NORTHWESTERN UNIVERSITY

Electrical Properties of Mesoscopic Spin Glasses

A DISSERTATION

SUBMITTED TO THE GRADUATE SCHOOL
IN PARTIAL FULFILLMENT OF THE REQUIREMENTS

for the degree

DOCTOR OF PHILOSOPHY

Field of Physics

By

Jonghwa Eom

EVANSTON, ILLINOIS

June 1998

ABSTRACT

Electrical Properties of Mesoscopic Spin Glasses

Jonghwa Eom

The electrical properties of mesoscopic AuFe wires have been measured in ^{4}He, ^{3}He, and dilution refrigerators. AuFe alloys in this study have Fe concentrations ranging from 0.1 to 0.4 at%, and their spin glass freezing has been observed in the resistivity $\rho(T)$ as a function of temperature, which shows a broad maximum at a temperature T_m. $\rho(T)$ of the AuFe spin glass wires has been investigated for wires of various widths in the range of 150 nm - 300 μm. The resistivity $\rho(T)$ of the AuFe wires indeed shows a size dependence. As the width of the wire is reduced, the amplitude of the resistivity maximum increases, and T_m shifts toward lower temperatures. However, the size dependence originates not from some intrinsic spin glass property, but from the electron-electron interaction contribution to $\rho(T)$. The four-terminal differential resistance, *dV/dI*, has also been measured as a function of dc current bias, *I*. We find that *dV/dI* becomes asymmetric in *I* when the width of at least one voltage terminal is less than 150 nm and different from the width of the other voltage terminal. We analyze *dV/dI(I)* of the AuFe wires by a model heat flow equation, and find that the asymmetry in *dV/dI(I)* reflects the size dependence of thermopower in mesoscopic AuFe spin glass wires.

Acknowledgments

I have the honor to acknowledge the support and encouragement of many people. My advisor, Prof. Venkat Chandrasekhar has inspired and stimulated me with incessant new ideas. He has taught me a wide range of topics from basic electronics to advanced physics. He has gladly provided me with his personal knowledge of experimental techniques, which make essential contributions to every single measurement in this study. Now I remember those days when Venkat and I started to build the Northwestern MesoLab in the winter of 1992. A helium-4 cryostat was the first achievement we had, and became the one which I wanted to show in pride.

Prof. Chris Van Haesendonck in Katholieke Universiteit Leuven, Belgium has been also my intellectual guide and advisor throughout the study of spin glasses.

My colleague, Chen-Jung Chien has helped me throughout the entire period of my Ph. D. course. He and I have shared the sorrows and joys of building the Northwestern MesoLab, and now we find that there are few things which have not been touched by our hands.

I am greatly indebted to Geert Neuttiens for my thesis, who showed the warmth of his heart during my visit of Leuven in 1996.

Dr. Christoph Strunk made an contribution to the early stage of developing the idea of thermoelectric effect in AuFe wires.

Jose Aumentado is the man who brings freshness to the Northwestern MesoLab,

and has continuously improved the lab facilities.

Dr. Brian Burk, the former research associate, helped me during the early stage of building the Northwestern MesoLab.

Dr. Michael Black, the current research associate, has helped me to comprehend the physical concepts with regard to superconductors.

I should not forget to thank Dr. Yoonseok Lee, who has gladly become my consultant with regard to cryogenic technology.

I also want to express my sincere gratitude for undergraduate helpers, Dennis Liang and Andrea Wells.

Prof. William Halperin and Prof. James Sauls have been always nice and kind to me, and I would like to appreciate their acceptance to be my dissertation committee.

Finally, I would like to dedicate this thesis to my wife Mihae, my son Woong, and my parents.

TABLE OF CONTENTS

LIST OF FIGURES

LIST OF TABLES

Chapter 1

INTRODUCTION

1.1 Size effect in electron scattering by magnetic impurities

Since its inception in the late seventies, mesoscopic physics has grown very rapidly because of modern nanofabrication technology. Utilizing a variety of etching and lithographical techniques, the size of electronic devices now approaches microscopic length scales. Complicated structures are frequently squeezed into a spot of 1 or 2 μm [47, 58, 138]. In such small devices conduction electrons behave coherently, giving rise to many kinds of quantum phenomena which are not observable in large scale devices.

The first example of such quantum phenomena is quantum interference, which includes weak localization [1, 20], conductance fluctuations [92], and the Aharanov-Bohm effect [8, 131]. These phenomena still provide some of the most challenging topics in mesoscopic physics [3, 93, 99]. In magnetic materials, quantum interference effects are more complex and interesting. Israeloff and Weissman [73] measured electrical noise in spin glass CuMn films and found the noise grows dramatically

as the films are cooled through the magnetic freezing temperature. The noise is attributed to spin fluctuations which are coupled to the resistivity through conductance fluctuations [52]. de Vegvar *et al.* [44] measured the magnetoresistance of CuMn mesoscopic spin glass wires and found fluctuations which were specific to microscopic spin configurations. These 'magnetofingerprints' are robust in magnetic field cycling, but dependent upon thermal cycling.

A second example of quantum phenomena is the *size effect.* When samples become smaller than a microscopic length relevant to some physical effect, fundamental modifications are expected in physical properties. The relevant length scale can be elastic mean free path, phase coherence length, or some other important length depending on the physics involved in the properties of interest.

Our question here is a microscopic length scale related to dilute magnetic alloys. Wilson in his renormalization group treatment of the Kondo effect [135] pointed out that the Kondo bound state has a critical transition to an infinitely strongly bound singlet state only when a sample becomes larger than a critical length $\xi_K = \hbar v_F / k_B T_K$. The idea of this length scale has been adopted by many researchers [61, 62, 72] and accepted as the radius of the Kondo screening cloud, which is basically an electron cloud accumulated around a magnetic impurity.

The first demonstration for this length in transport measurements was reported in a publication by Chen and Giordano [38]. However, as Bergmann argued [17], there is a question about the estimation of ξ_K and the actual size can be a few

orders of magnitude smaller than $\hbar v_F/k_B T_K$. Furthermore, a series of subsequent low temperature transport measurements by DiTusa *et al.* [46], Blachly *et al.* [27], Chandrasekhar *et al.* [34], and Yanson *et al.* [137] did not agree with each other, so that there is no definite conclusion regarding the size effect of the Kondo resistivity slope as well as the Kondo temperature.

In this study, we look for a fundamental length relevant to dilute magnetic alloys. We have used AuFe metallic spin glass thin films for dilute magnetic alloys. In spin glasses the distance between magnetic impurities is expected to be smaller than the radius of the Kondo screening cloud [19]. We want to answer the question "Is there a size effect in spin glasses?".

1.2 Before mesoscopic spin glasses

Spin glasses are fascinating systems which provide not only a variety of new concepts but also many unique phenomena. The history of spin glasses goes back to the 1970's when the term 'spin glass' was first coined. After evidence for a phase transition was discovered in low field susceptibility measurements [33], spin glasses became a very attractive topic in condensed matter physics and have been investigated by a wide spectrum of experimental probes including magnetization, specific heat, resistivity, and neutron scattering [100].

A spin glass is a system of magnetic impurities, for which the moments are frozen in random orientations. The randomness originates from competitive interac-

tions among the magnetic moments, which are freely rotatable at high temperature, but are frozen below a certain temperature T_f, which is called the spin glass freezing temperature. The key features of the interactions in metallic spin glasses are described by the Ruderman-Kittel-Kasuya-Yosida (RKKY) interaction [77, 110, 139], which is an oscillating function of the distance (r) between magnetic moments, its amplitude decaying as $1/r^3$.

There are still many unresolved problems with regard to spin glasses. Among those the most fundamental issue is whether the spin glass freezing is a phase transition or not. Zero field ac susceptibility supports the existence of a phase transition [33], but other properties such as resistance and specific heat do not provide definite evidence for the existence of a phase transition [57, 133]. In conventional neutron scattering experiments, despite a lot of work, no one has found any change in spin density wave associated with spin glass freezing [32, 60, 134]. From the theoretical point of view, the difficulties with spin glasses include the fact that there is no conventional order parameter as in ferromagnetic or in antiferromagnetic material.

Spin glasses have been found in a variety of materials including metals, semiconductors, and insulators [100]. Among these, we will concentrate on metallic spin glasses in this study. The metallic spin glass has been made by alloying a noble metal (Au) with a small amount of transition metal (Fe). The magnetic impurity (Fe) concentrations of our samples range from 0.1 to 0.4 at%. Although no

measurements have been made in this study, Kondo (in the dilute impurity limit), or ferromagnetic (in the highly concentrated impurity limit) samples can be made simply by adjusting the impurity concentrations.

1.3 Mesoscopic spin glasses

In this study we have confined our focus to *mesoscopic spin glasses*, which means spin glasses whose dimensions are on the order of $\sim \mu$m. The problem which we are going to investigate is what is the relevant microscopic length scale for spin glasses. The system we studied in this dissertation are AuFe nanowires, which are fabricated by electron beam lithography, combined with either flash evaporation of AuFe mother alloy or Fe ion implantation into Au thin films.

The measurements which we employed are divided into two different categories; the resistivity as a function of temperature $\rho(T)$, and the differential resistance as a function of dc bias current $dV/dI(I)$.

A conventional tool to probe the size dependence of the Kondo effect has been a measurement of $\rho(T)$ [24, 34, 38, 46]. In spin glasses, $\rho(T)$ is still an important tool to investigate the properties of interimpurity interactions. The shape of $\rho(T)$ becomes more complicated due to the interplay of the spin-flip scattering and the spin glass freezing [89, 90]. We will analyze the influence of size on $\rho(T)$ of mesoscopic AuFe spin wires.

A measurement of $dV/dI(I)$ of mesoscopic AuFe spin glass wires has also been

developed as a useful probe to investigate the transport properties of spin glasses. Most $dV/dI(I)$ experiments for spin glasses so far [124, 125, 136, 137] have focused mainly on the ballistic transport regime, where the actual sample size is comparable to the elastic mean free path. In this study, we extend $dV/dI(I)$ measurements to the diffusive regime and find an interesting phenomenon in this regime as well. The differential resistance $dV/dI(I)$ is directly related to the issue of heat flow in diffusive metals, and gives information about one of the off-diagonal elements of the transport matrix; the thermopower.

Chapter 2

PREVIOUS EXPERIMENTAL WORK

2.1 Size dependence in the Kondo resistivity

2.1.1 Finite size effect in the magnitude of the Kondo anomaly

In the past eight years a number of groups including ourselves have studied the influence of the size of samples on the Kondo anomaly. The critical length to see a size effect of the Kondo anomaly is believed to be the Kondo length, which is estimated to be $\xi_K \approx \hbar v_F / k_B T_K$ in clean samples (see Section 3.3.4). Physically ξ_K is expected to be the size of the conduction electron screening cloud (the Kondo screening cloud) around the magnetic impurity. Experiments have focused on the deviation of the resistivity from its value in bulk samples as the size of samples is reduced below ξ_K. The first experiment was by Chen and Giordano [38], who measured the resistivity of AuFe 30 ppm thin films and found that the logarithmic slope of the Kondo resistivity became smaller as the film thickness was reduced below $\sim$ 2500 Å.

Soon after Chen and Giordano's experiment, DiTusa *et al.* [46] explored the effect of finite size on the Kondo resistivity anomaly in CuCr systems. In their

experiments, samples with two different concentrations (1000 ppm and 2000 ppm) were prepared. In the 1000 ppm CuCr films, which were claimed to be in the Kondo regime, the slope of resistivity decreased as the width of samples was reduced below $\sim$ 10 μm. However, in the 2000 ppm CuCr films, which were in the spin glass regime, the temperature T_m where $\rho(T)$ has a maximum decreased as the width was reduced below $\sim$ 2.0 μm. They interpreted the decrease of T_m as being due to the modification of interimpurity interactions caused by the reduction of the sample size.

Another experiment on AuFe alloys showed the 2-dimensional to 1-dimensional crossover in the slope of the Kondo resistivity. Blachly and Giordano [27] found the Kondo resistivity slope drastically decreased as the width of the wires was reduced below 2000 Å. They associated this length scale with the Kondo length ξ_K appropriate for dirty metals. In the presence of impurities, the Kondo length ξ_K is given by the dirty limit formula $\xi_K = \sqrt{\hbar D/k_B T}$, which is $\sim$ 3000 Åfor samples of Blachly and Giordano [27]. However, when the width of the samples was reduced further below L_T ($\sim$ 1200 Å at 1.5 K), the low temperature resistivity slope was found to increase. This was interpreted by the fact that electron-electron interactions contribute to the low temperature resistivity, giving rise to an increase in ρ as T is reduced.

So far we have illustrated many experiments on a variety of magnetic alloys, and in each experiment the manipulation of sample size has been accomplished

either by varying the film thickness or by varying the width. The consensus from the experiments are as follows:

- The Kondo temperature shows no significant size effect.
- The low temperature Kondo resistivity slope, $d\rho/d\ln T$ decreases as either the film thickness or the width of the wire is reduced.

The Kondo temperature T_K is defined as a fitting parameter in a fit equation [45]:

$$\Delta\rho(T) = \rho_0 + B\left\{1 - \frac{\ln(T/T_K)}{[\ln^2(T/T_K) + \pi^2 S(S+1)]^{1/2}}\right\} \tag{2.1}$$

where the parameter B depends on the host metal, the impurity element, and concentration. S is spin of a impurity.

2.1.2 Kondo scattering in point contacts

Yanson *et al.* employed the mechanically controllable break junction technique to investigate the point contact spectra dV/dI for CuMn alloys [136, 137]. The size of the contact is comparable to atomic size scales, ranging from 2 to 50 nm. They found that a zero bias maximum in dV/dI due to Kondo scattering increased as the contact diameter d was reduced. Turning to the theory for Kondo scattering in point contacts [105], they estimated J/E_F by measuring d^2I/dV^2. Here J is the exchange interaction, and E_F is the Fermi energy. The estimated J/E_F scaled as d as $\sim d^{-1/3}$, and the calculated Kondo temperature $k_B T_K$ $(= E_F \exp(-2E_F/3J))$ shows a strong size dependence, reaching $T_K \sim 3\times10^3$ K at $d \approx 2$ nm. In the upper

limit of the point contact size ($d \approx 50$ nm), T_K reaches ~ 2 K. The bulk value of T_K for CuMn is usually taken to be order of 0.01 K, and hence the crossover length scale for the anomalous enhancement of T_K was estimated to be ~ 0.5 μm.

By using the same mechanically controllable junction technique, van der Post *et al.* [124] investigated the size effect of the Kondo scattering in CuFe alloys. As before, T_K increased as d was reduced, but only by a factor of ~ 2. For example, $T_K \approx 50$ K at $d \approx 1.5$ nm, which was comparable to $T_K \approx 30$ K at $d \approx 35$ nm.

In summary, the mechanically controllable junction technique was used to investigate the size effect at very small length scales ranging from 2 to 50 nm. It was found that the estimated T_K increased as the contact size was reduced. It is worthwhile to note that no change of T_K was found in the quasi 1-dimensional wires or 2-dimensional films, discussed in Section 2.1.1.

2.1.3 Absence of size dependence of the Kondo resistivity

Most experiments indicate the existence of a size effect in the Kondo resistivity. However, there is one experiment which provides evidence for the absence of size dependence of the Kondo resistivity. Chandrasekhar *et al.* [34] measured the resistivity of AuFe wires which were fabricated by ion implantation methods. The width of the samples ranged from 38 nm to 106 μm. $\Delta\rho$ $(= \rho(T) - \rho(T \approx 8K))$ indeed showed a size effect, increasing as the width of wires was reduced. However, after subtracting the electron-electron interaction contribution from $\Delta\rho$, the

material	*thickness*	*width*	T_K	ξ_K	*size effect*	Ref.
AuFe	265 - 4350 Å	2D film	1 K	10 μm	yes	[38]
CuCr	212 Å	0.14 - 35 μm	2 K	6 μm	yes	[46]
AuFe	150 Å	0.14 - 150 μm	1 K	10 μm	yes	[27]
CuMn	point contact	2 - 50 nm	0.01 K	1.2 mm	yes	[137]
CuFe	point contact	1.6 - 34 nm	30 K	0.4 μm	yes	[125]
AuFe	300 Å	.038 - 105 μm	1 K	10 μm	no	[34]

Table 2.1: Previous experiments on the size effect of the Kondo resistivity.

pure Kondo contribution to resistivity appeared to be independent of the width of the wires down to a width of 38 nm. This observation obviously runs counter to the previous observations which agree to the size effect of the Kondo scattering, bringing about a controversy regarding the size scale of the Kondo screening cloud.

Even before the work by Chandrasekhar *et al.* there were two experiments which supported the absence of a size effect in the Kondo resistivity. Van Haesendonck *et al.* [126] measured weak localization in CuCr thin films of various thicknesses and found that the electron-spin scattering time was not altered from the bulk value, down to a film thickness of $\sim$ 50 Å. Bergmann [19] measured weak localization in Mg/Fe/Mg thin film for different thicknesses of the second Mg film and found the screening of the magnetic impurity was not hindered by the finite size of the second Mg film thickness, if the thickness of this film was above $\sim$ 5

atomic layers.

We summarize the experimental studies on the size dependence of the Kondo resistivity in Table 2.1, where T_K is the Kondo temperature of a bulk sample and the corresponding Kondo length ξ_K is estimated by $\hbar v_F / k_B T_K$.

2.1.4 The role of disorder

Although it was not directly related to the size effect of Kondo systems, an interesting issue was experimentally investigated by Blachly *et al.* [25]: namely, what role does disorder play on the Kondo effect in 2-dimensional films? Practically, they studied the Kondo effect which is affected by disorder in an overlayer film. They fabricated bilayer samples which consisted of CuFe and Cu 2-dimensional films. The first layer was a CuFe film. For the second layer, the Cu film was actually sputtered in an Ar environment. The pressure of the Ar determines the degree of disorder. We summarize their observations:

- An enhanced Kondo effect was observed in the presence of a nonmagnetic overlayer.

- The presence of disorder in a nonmagnetic overlayer suppressed the Kondo effect.

A similar effect has been also found in a slightly different system, namely AuFe/Au thin film [26]. A theoretical model to explain this effect [96, 121, 122, 123] has been

proposed, and will be described in Section 3.4.1.

2.2 Size dependence in the spin glass resistivity

How is the size effect modified if distances between magnetic impurities are smaller than the size of the Kondo screening cloud? To answer this question, a series of experiments on systems with concentrated magnetic impurities, *i.e.*, spin glasses have been done in the last four years.

2.2.1 Finite size effect in spin glasses

Lane *et al.* [87] measured resistivity of CuCr films with concentrated magnetic impurities and found a size dependence of the interimpurity interaction Δ_c in spin glasses. Δ_c was qualitatively estimated by the average local internal field, H_0, which was obtained from the fit of the resistance maximum temperature, T_m, as a function of magnetic field, H

$$T_m(H) - TWm(0) = A\frac{H^2}{\sqrt{H^2 + H_0^2}} \tag{2.2}$$

where A is independent of size and thus a constant for samples from the same evaporation. By measuring H_0 in samples of various sizes, Lane *et al.* [87] concluded that Δ_c decreased as either the width (ranging from 0.9 - 5.0 μm) or the thickness (ranging from 150 - 1670 Å) of the samples was reduced.

van der Post *et al.* [125] studied the point contact spectroscopy of CuMn (1 at%) sample using a mechanically controllable break junction. The diameter of

the contact ranged from 0.5 nm to 50 nm. The observed dV/dI showed that the ratio Δ_c/T_K decreased with decreasing contact diameter. However, the decrease of Δ_c/T_K did not indicate directly the size effect in Δ_c, because T_K itself had been found to be dependent on size [136, 137]. Furthermore, the internal field, H_0, showed no evidence of size dependence. Therefore, it was concluded that there was no definite evidence for size dependence of Δ_c in point contact spectroscopy, in the size regime ranging from 0.5 to 50 nm.

2.2.2 Absence of size dependence in the spin glass resistivity

Neuttiens *et al.* [104] extended the study of size dependence of AuFe wires from the Kondo regime to the spin glass regime. Keeping the film thickness the same, the width of the samples was varied from 300 μm down to 150 nm. The detailed analysis of this result will be discussed in Section 5.3. The conclusion of this work can be summarized:

- Although the resistance maximum temperature T_m decreases as the width of the sample is reduced, this is due to the electron-electron interaction (EEI) contribution to the low temperature resistivity, $\rho(T)$. After subtracting the EEI contribution, $\rho(T)$'s of samples of different widths fall into a single functional form, indicating no size dependence in the spin glass resistivity.

- The presence of disorder in the samples affects the interimpurity interaction Δ_c. Δ_c decreases as disorder is increased. The disorder effect is more promi-

nent in thin films in comparison to bulk samples. Δ_c is less by a factor of $\sim$ 3 in thin films compared to bulk samples.

2.2.3 Size dependent thermopower in mesoscopic spin glass wires

Very recently Strunk *et al.* [115] combined an electron heating experiment (which is basically identical to the experiment in Chapter 6) and noise thermometry to measure the thermopower of AuFe spin glass nanowires. The method they employed is basically the same as that in this dissertation. They measured the differential resistance as a function of dc bias current, and estimated the difference in the thermopower of two AuFe wires of different widths. In contrast to the experiments discussed in this dissertation, the electron temperature of the heater wire is directly measured by noise thermometry, rather than being estimated by a model heat flow equation. Ion implanted AuFe wires were used, and the impurity concentrations were 50 ppm and 0.3 at%. For both the concentrations they found non-zero $dV/dI_A(I)$'s at the bath temperature $T = 0.3$ K. They also found that the amplitude of $dV/dI_A(I)$ for 0.3 at% AuFe wires is bigger than that for 50 ppm. They showed the thermopower difference $\Delta S(T)$ of two different 0.3 at% AuFe wires, of which widths were 305 nm and 105 nm respectively. The estimated $\Delta S(T)$ is ~ 0.6 μV/K at $T = 4$ K. This magnitude is comparable to the value ($\Delta S \approx 0.4$ μV/K) found in the experiments in this disseration.

Chapter 3

MODELS AND THEORIES

In this chapter we are going to review relevant concepts and models with regard to dilute magnetic alloys. First, we discuss magnetic moments in metals. Second, a brief review of the classic models of spin glasses will be given. Although these classic models may not be directly related to the experiments in this study, they are incorporated in this chapter to give a more general understanding of spin glasses. After the review of the classic models, we review the more recent theoretical models which attempt to explain the results of experiments in mesoscopic Kondo alloys.

3.1 Magnetic moments in metals

3.1.1 Isolated magnetic impurity; the Kondo effect

Even very small amounts of magnetic impurities cause a manifest difference in the resistivity of metals (Cu, Ag, Au, etc) at low temperatures, giving rise to a resistivity $\rho(T)$, which increases logarithmically as the temperature T is lowered. The interplay of this contribution to the resistivity with the contribution due to phonon scattering at higher temperatures leads to a minimum in $\rho(T)$ at some intermediate

temperature T. This phenomenon is known as the Kondo effect after Jun Kondo [85] who explained the effect by taking into account the higher order corrections in the electron-spin scattering matrix. He showed that the magnetic scattering cross section could be divergent when the scattering was treated to more than the leading order term in perturbation theory. Kondo's result for the logarithmic increase in $\rho(T)$ is given in the form of [63, 83]

$$\rho_{Kondo} \sim \rho_0 \left[1 - JN(0) \ln\left(\frac{k_B T}{\Delta}\right)\right], \quad T > T_K \tag{3.1}$$

where J is the exchange interaction, $N(0)$ the electron density of states at the d orbital of the magnetic impurity, and Δ the d level broadening. The Kondo temperature T_K is the temperature at which resistivity $\rho(T)$ deviates from the above approximation $\rho_{Kondo}(T)$, and is given by

$$k_B T_K \approx \Delta \exp\left[-\frac{1}{JN(0)}\right] \tag{3.2}$$

In addition to the Kondo contribution, the low temperature resistivity includes the phonon contribution, which is proportional to T^5 [13]. Therefore, the resistivity is expected to have following properties:

- $\rho(T)$ has a minimum at a temperature T_{min}, which is given by $d\rho(T)/dT = 0$. T_{min} is proportional to $N(0)^{1/5}$, and hence $\propto c^{1/5}$, where c is the concentration of magnetic impurities.

- The slope of the logarithmic increase in $\rho(T)$ is proportional to c. For example,

experimentally the slope for AuFe alloys is found to be ~ 0.11 nΩcm/ppm per decade of temperature[64, 100].

Dilute magnetic alloys exhibit a large thermoelectric effect. This is simply due to the strong energy dependence of the distribution function of the conduction electrons at the Fermi level. The thermopower for dilute magnetic alloys is given in the form of [140]

$$S = -\frac{\pi^2}{3}\frac{k_B}{e}k_B T\left[\frac{\partial \ln \rho(\varepsilon)}{\partial \varepsilon}\right]_{\varepsilon=\varepsilon_F} \tag{3.3}$$

where ε is energy of conduction electrons. Again, the strong energy dependence of ρ_{Kondo} at the Fermi level ε_F explains the giant thermopower observed in dilute magnetic alloys. Note that Eq. 3.3 holds also for conventional normal metals.

Some features of thermopower in dilute magnetic alloys are listed here [84]:

- When the thermal energy is smaller than the Zeeman splitting of the localized spins ($T \ll 2\mu_B H_0/k_B$, where H_0 is internal field), the thermopower shows a linear dependence in T.

- When $T \gg 2\mu_B H_0/k_B$, thermopower becomes independent of the impurity concentration as well as temperature.

- When phonon scattering dominates the magnetic scattering, the thermopower deceases. The decrease occurs faster for lower impurity concentration than for higher impurity concentration.

- In a magnetic field, the thermopower is expected to vary as $1/H$. However, the actual behavior is considerably more complicated [69].

3.1.2 Interactions between magnetic moments; the RKKY interaction

The magnetic moments in a dilute magnetic alloy communicate with each other if the concentration of magnetic impurities exceeds a certain value. The distance between impurities is not necessarily close enough for their charge distributions to overlap directly, but is close enough to make an *indirect exchange interaction* via conduction electrons. This interaction is the so-called Ruderman-Kittel-Kasuya-Yosida (RKKY) interaction, which is an oscillating function of distance r, [77, 110, 139]

$$J_{RKKY}(r) \propto \frac{1}{r^2}\left[\frac{\cos k_F r}{2k_F r} - \frac{\sin k_F r}{(2k_F r)^2}\right] \tag{3.4}$$

The above equation (Eq. 3.4) is derived with the assumption that metals are in the clean limit; that is, the mean free path ℓ is much longer than the average interimpurity distance R. Modification of the RKKY interaction would be expected in the disordered metal when the mean free path $\ell < R$. Jagannathan showed [74] that although the first cumulant $J^{(1)}(R)$ ($\equiv [J]_{av}$, where $[\ ]_{av}$ is an average over impurity configurations) falls off as $exp(-R/\ell)$, the second cumulant $J^{(2)}(R)$ ($\equiv [(J - [J]_{av})^2]_{av}$ is long ranged, falling off as a power law in R just as in the pure metal. The thermodynamic average of $J^{(1)}(R)$ and $J^{(2)}(R)$ are given by [74]:

$$\overline{J^{(1)}(R)} = J_0 exp(-R/\ell)$$

$$\overline{J^{(2)}(R)} = 3\left(\frac{mk_F}{(2\pi)^3}\right)^2 \frac{1}{R^6} \tag{3.5}$$

Note that while $\overline{J^{(1)}(R)}$ depends on ℓ, $\overline{J^{(2)}(R)}$ is independent of ℓ.

Depending on the experimental quantity of interest, the effective interaction between spins is determined by either $\overline{J^{(1)}(R)}$ or $\overline{J^{(2)}(R)}$. For example, while the line shift in the nuclear magnetic resonance (NMR) spectrum should yield information on $\overline{J^{(1)}(R)}$, the spin glass freezing temperature T_f is determined by $\overline{J^{(2)}(R)}$ [54, 113]. Therefore the line shift of the NMR spectrum is expected to fall off as $\sim exp(-R/\ell)$ [65], but T_f *is expected to be independent of* ℓ [127].

Bergmann [18] also investigated the RKKY interaction in the disordered regime. He interpreted the RKKY oscillations as an interference of the conduction electrons scattered off the impurities with a magnetic moment, which is similar to his treatment of weak localization except that the impurities now are magnetic impurities [20]. He found that the zero temperature exchange interaction $J(r)$ depends on the distance as $1/r^d$, where d is the sample dimension and at finite temperature its range is limited by the thermal diffusion length $(\hbar D/k_B T)^{1/2}$.

3.1.3 Spin glasses

When the RKKY interactions among magnetic impurities become dominant over the thermal energy $k_B T$, the spins in concentrated magnetic alloys freeze with random orientations. The randomness originates from the fact that the distances

between impurities are randomly distributed, and the RKKY interaction alternates in sign as a function of the distance between impurities.

Some measurements show that a spin glass freezing occurs gradually as the temperature T is lowered, and do not support the existence of a phase transition. However, the zero field ac susceptibility has a sharp cusp at a temperature T_f, which supports the existence of a phase transition [33]. Since there is no explicit order parameter which can be confirmed by experiments, it is still being debated whether the spin glass freezing is a phase transition or not.

The resistivity of a spin glass shows a broad maximum at a temperature T_m, which is a factor of 2 - 3 higher than T_f [57]. The broad maximum comes from the interplay of the Kondo effect and the spin freezing at lower temperature. The mechanism of the Kondo effect which is based on spin flip scattering, still exists even in the presence of the RKKY interactions [90], causing an increase of the resistivity as T is lowered. However, when the thermal energy k_BT becomes smaller than the RKKY interaction, spin flip scattering is suppressed, and resistivity thus decreases as T is lowered. Consequently a broad maximum is found in $\rho(T)$.

Although the spin glasses discussed here are restricted to metallic spin glasses, there are other types as well; insulating spin glasses and semiconducting spin glasses. These spin glasses include, for examples, (EuSr)S, CdMnTe, $(MgFe)Cl_2$, and $ZnFeF_2$ [100]. In such spin glasses there are no conduction electrons to mediate the interactions between magnetic moments. However, the nonmagnetic ions over-

lapping the charge clouds of the neighboring magnetic ions convey the interactions between the magnetic moments; this is the so-called *superexchange interaction.* In these spin glasses the detailed microscopic interactions are not the same as that in metallic spin glasses, but share their nature with metallic spin glasses and are describable by the same models.

3.2 Classic theoretical concepts and models for spin glasses

In this section we denote the spin glass freezing temperature by T_c, in the spirit that spin glass freezing is a true phase transition in the framework of infinite ranged exchange interactions.

3.2.1 Order parameter; the Edwards and Anderson model

Although the RKKY interaction explains how the spins in a dilute magnetic alloy have randomness in the configuration of their orientations, it does not provide a further description for 'spin glass freezing'. For the dynamics regarding a phase transition, one needs a more dependable theoretical tool, for example, a mean field theory. Even with a mean field theoretical approach it is a difficult task to describe the spin glass freezing, because there is no conventional long range order which is experimentally observable, as in ferromagnetic or antiferromagnetic materials.

The first attempt to solve this problem was by Edwards and Anderson [48]. In their pioneering paper they proposed a spin glass order parameter q, which is

defined by

$$q = \lim_{\Delta t \to \infty} < \mathrm{s_i}(t) \cdot \mathrm{s_i}(t + \Delta t) > \tag{3.6}$$

where $< >$ represents a thermodynamic average and $\mathrm{s_i}(t)$ is the spin which is found at a lattice site i at the time t. At $T = 0$ one expects $q = 1$, while at $T \geq T_c$, $q = 0$.

Starting with a simple interaction energy $J_{ij}\mathrm{s_i} \cdot \mathrm{s_j}$, Edwards and Anderson calculated the order parameter as a function of T [48], which is given as follows:

$$\begin{aligned} q^2 &= 5\left[1 - \left(\frac{T}{T_c}\right)^2\right]\left(\frac{T}{T_c}\right)^4 \\ \text{where} \quad T_c &= \frac{\sqrt{2}\,J_0}{3k_B} \end{aligned} \tag{3.7}$$

where J_0 is the mean value of exchange interaction. A non-zero q exists in the regime $0 < T < T_c$, indicating the existence of a second order phase transition. A further calculation for the susceptibility χ yields

$$\begin{aligned} \chi &= \frac{a}{T} \qquad \text{when} \quad T > T_c \\ &= \frac{a}{T_c} - \mathcal{O}(T_c - T)^2 \qquad \text{when} \quad T < T_c \end{aligned} \tag{3.8}$$

This result explains well the generic shape of the measured $\chi(T)$. However, in a further calculation the theoretical specific heat for $s = 1/2$ was found to be in complete disagreement with experiment [54]. Nevertheless, the Edwards and Anderson model provides a convenient simple picture of the spin glass transition as well as the definition of an appropriate order parameter.

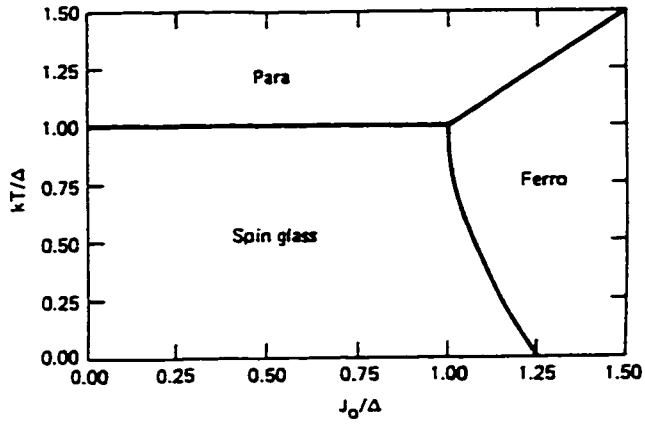

Figure 3.1: Phase diagram for infinite ranged Ising spins from the Sherrington and Kirkpatrick model. From Ref. [112]

3.2.2 The first mean field theory of spin glasses; the Sherrington and Kirkpatrick model

Let $\mathcal{H}_J(s)$ be the Hamiltonian for a spin glass system, which depends on the configuration of spins s and on the interaction J between the spins. The magnitude of J is distributed according to a probability $P(J)$, the functional form of which depends on the model one chooses.

The simplest choice for $P(J)$ may be a Gaussian distribution, which is found to be good enough for most studies of thermodynamic properties [82]. Using the Gaussian distribution $P(J)$, Sherrington and Kirkpatrick [112] applied mean field theory to infinite ranged spin glasses. In an infinite ranged spin glass the functional form of $P(J)$ is the same for any pair of spins in the system. In the end they provided a phase diagram of a spin glass ferromagnet, which is shown in Fig. 3.1.

As Sherrington and Kirkpatrick showed, there are two significant order pcrameters in the phase diagram, which are given as follows:

$$\begin{aligned} m &= [< s_i >]_{av} \\ q &= \lim_{\Delta t \to \infty} [< s_i(t) \cdot s_i(t + \Delta t) >]_{av} \end{aligned} \tag{3.9}$$

A non-zero m indicates ferromagnetic order, while non-zero q indicates magnetic order, *i.e.* a spin glass. There are three different regimes depending on the order m and q; first, a paramagnetic state ($m = 0$ and $q = 0$), second, a ferromagnetib state $m \neq 0$ and $q \neq 0$, and third, a spin glass state $m = 0$ and $q \neq 0$. In Fig. 3.1, J_0 is the average of the exchange interaction J and Δ is the second cumulant of J.

An interesting situation happens for J_0/Δ between 1 and $\sqrt{\pi/2}$, which can be satisfied in a certain range of magnetic impurity concentrations. There are two phase transitions in sequence as T is lowered. A phase transition from paramagnetic to ferromignetic is followed by a transition from ferromagnetic to spin glass; the so-called *reentrant effect.* In the exact solution of the Sherrington-Kirkpatrick model by Parisi's replica symmetry breaking scheme, this reentrant spin glass phase is replaced by a *mixed xhase* which is a ferromagnetic phase with replica symmetry breaking [22]. Regardless of what the reentered phase is called, reentrance effects have been observed in various systems [39, 49, 95]

The Sherrington-Kirkpatrick (SK) model is a mean field theory version for the Edwards and Anderson model, which is exactly solvable with a replica trick and reproduces the most desirable features of the Edwards and Anderson model.

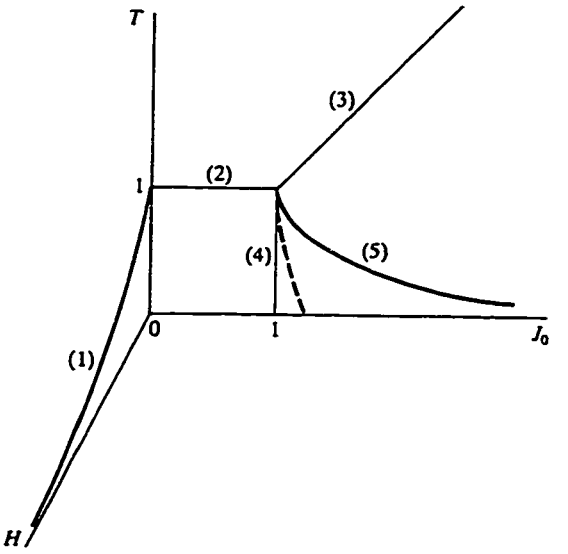

Figure 3.2: Exact phase diagram of the SK model by Parisi's replica symmetry breaking. Lines 1 and 5 are determined by the Almeida-Thouless instability, line 2 by $q = 0$, line 3 by $m = 0$, $q = 0$, and line 4 by $q \neq 0$, $m = 0$. The broken line represents the (incorrect) original SK solution. From Ref. [53].

However, it gives a negative entropy at low temperature, which cannot be correct in discrete Ising models. Such problems in the SK model have been investigated extensively by de Almeida and Thouless [43]. They found an instability (which means the free energy is no longer an extreme) not only in the spin glass phase of the SK model for all temperatures below T_c at zero field, but even in the ferromagnetic phase at non-zero field where the SK solution had been analytic. This instability problem led to a series of works with regard to replica symmetry breaking [106, 107, 108].

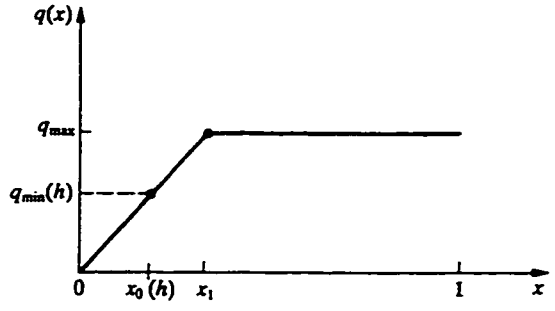

Figure 3.3: Parisi solution for the order parameter $q(x)$ near $T = T_c$. The solid line is for local field $h = 0$ and the broken line is for a finite h. For $h = 0$, $q_{min} = 0$, but q increases monotonically as h is increased. From Ref. [53].

3.2.3 Replica symmetry breaking; the Parisi solution

The SK solution, although it is the first true mean field treatment of spin glass, turns out to be clearly unphysical. The free energy of the SK solution leads to a negative entropy for $T \to 0$. This problem and the Almeida and Thouless (AT) instability require a reconsideration of the replica symmetry scheme in the mean field theory. A breakthrough of the problem has been made by Parisi [106, 107, 108]; the so-called replica symmetry breaking (RSB). The key result of RSB is that the order parameter is replaced by the integral of the order parameter density $q(x)$, where the parameter x runs from 0 to 1 continuously. The idea in introducing the parameter x is to make the order parameter q continuous in the local field h. $q(x)$ for a spin glass has been calculated near $T = T_c$ and is shown in Fig. 3.3.

The susceptibility of a spin glass, which is obtained from the second derivative

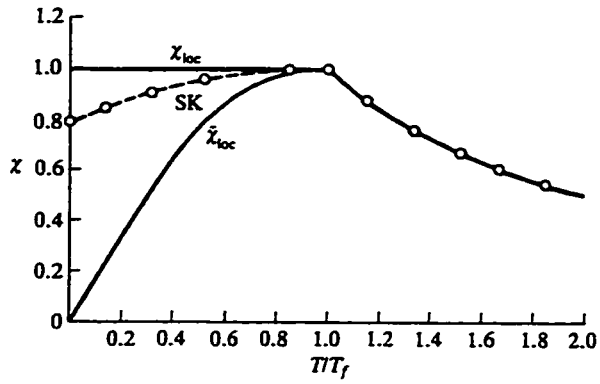

Figure 3.4: Parisi solution for a susceptibility. Susceptibility $\chi = (k_BT)^{-1}(1 - \int_0^1 q(x)dx)$, $\bar{\chi} = (k_BT)^{-1}(1 - q(1))$, and the broken line represents the SK solution. From Ref. [53].

of free energy with respect to local field h, is given in the form of

$$\chi = \frac{1}{k_BT}\left[1 - \int_0^1 q(x)dx\right] \tag{3.10}$$

The final result for $\chi(T)$ is shown in Fig. 3.4. χ resembles the field cooled susceptibility found in experiments, while $\bar{\chi} = (k_BT)^{-1}\ (1 - q(1)\ )$ the zero field cooled ac susceptibility.

The importance of Parisi's RSB solution includes the fact that it resolves not only the AT instability in the spin glass state but also the problem with regard to the negative entropy. It also proves that the spin glass system is still manageable within the framework of the mean field theoretical approach. However, from an experimentalist's point of view the exactitude of the RSB solution is not easy to check since the model still bases its argument on infinite ranged interactions between spins, which is unrealistic.

3.2.4 Droplet model; the Fisher and Huse approach

Parisi's replica symmetry breaking solution of the SK model makes the conventional theoretical approach for the questions of spin glasses stay within the mean field theory. Consequently, most measurements have concentrated on the properties which are incorporated into the mean field theory, for example, susceptibility, specific heat, and resistivity. However, there have been theoretical efforts based on techniques other than the mean field theory, providing new concepts and predictions of spin glass properties. Such theoretical approaches include the gauge theory of spin glasses, the hydrodynamic theory of spin waves, the scaling theory, and numerical simulations by Monte Carlo, etc. The details of each approach can be found in the review paper by Binder and Young [22] as well as the book by Fischer and Hertz [53]. Here we summarize the most attractive model to us since it provides the concept of a fundamental length scale for spin glasses. So far this dynamical length scale has not been observed in experiments, but a possible relationship with the observation in this study cannot be absolutely excluded.

In 1986 Daniel Fisher and David Huse [55, 56] published a paper in which they described spin glasses from a completely different point of view; a scaling of low lying large scale droplet excitations. The interaction in this model is *short ranged*, being a nearest-neighbor interaction. The order parameter is still defined

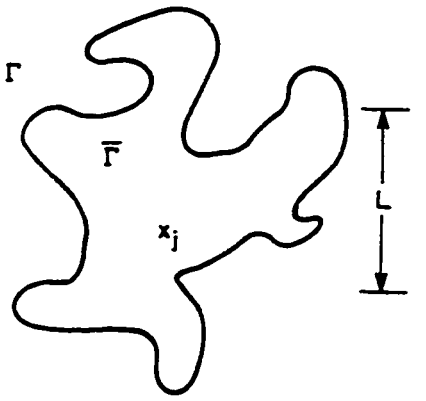

Figure 3.5: Schematic picture of the droplet model. L is the size scale for a droplet, in which the spins are aligned as in the ground state $\bar{\Gamma}$. From Ref. [55].

in a similar way as the original Edwards-Anderson type,

$$q_M = \frac{1}{V}\sum_{i,j}[< S_i >< S_j >]_{av} \tag{3.11}$$

where $< >$ denote a thermodynamic average within a given state, and $[\ ]_{av}$ the configurational average. Ground states have the property that their energy cannot be lowered by flipping any finite collection of spins. In an Ising spin glass there will be certainly at least one pair of ground states, which are symmetric from the point of view of global spin reversal. Fisher and Huse argued that there is only one pair of ground states in the spin glass system. Within their argument we denote one ground state by Γ, and the other $\bar{\Gamma}$, obtained from Γ by a global spin flip. The droplet of length scale L is defined as a domain, in which the spins are aligned as in the ground state $\bar{\Gamma}$. Outside of droplet the spins are aligned as in the ground state Γ, which is just the global spin reversed state of $\bar{\Gamma}$ (See Fig. 3.5).

The shape of the droplet is complicated, making its surface fractal. For a droplet of size L, the typical surface area A_L is given in the form of

$$A_L \sim L^{d_s} \tag{3.12}$$

The fractal dimension d_s in the d-dimensional system satisfies

$$d - 1 < d_s < d \tag{3.13}$$

Bray and Moore calculated the area of a domain wall in small 2-dimensional Ising spin glass samples, where they find $d_s \approx 1.3$ [29].

The typical droplet free energy F_L in the natural scaling ansatz scales as

$$F_L \sim L^{\theta} \tag{3.14}$$

with some exponent θ. θ increases with increasing dimensionality d. For $d = 1$, $\theta = -1$, while $\theta \approx -0.25$ for $d = 2$, and $\theta \approx 0.2$ for $d = 3$ [30, 70, 98]. The upper limit of θ is set by $(d-1)/2$. If $\theta < 0$, L in the low lying excitation state becomes longer and longer, thereby destroying the spin glass freezing. Therefore, the spin glass transition within the droplet model exists only in $d = 3$. The droplet model predicts a number of properties of the low frequency dynamics of the spin glass. To form a droplet of a length scale L, it is necessary to go over a free energy barrier B, which scales typically as $\sim L^{\psi}$. Here another exponent ψ is introduced, the magnitude of which is in the range $\theta \leq \psi \leq d - 1$. Therefore, the characteristic time τ_L that a droplet of size L will last is written as

$$\tau_L \sim \tau_0 \exp(\frac{B}{k_B T}) \tag{3.15}$$

At high temperature τ_0 determines the characteristic microscopic time scale at which a small droplet appears and disappears from the system.

3.3 Length scales in mesoscopic samples

3.3.1 Elastic mean free path, ℓ

The concept of this length originates from the Drude model of conduction electron scattering. In the Drude model, the motion of conduction electrons in metals is analogous to that of neutral molecules in dilute gases. The interactions between the conduction electrons are ignored, but the interactions between electrons and ions are taken into account to explain the resistances of metals.

In the Drude model, the relaxation time τ is given by

$$\tau = \frac{m}{\rho n e^2} \tag{3.16}$$

where ρ is resistivity. For Au, $\tau \approx 6.0/\rho_\mu \times 10^{-14}$ sec, where ρ_μ is the resistivity in the unit of $\mu\Omega$cm [13]. The $\rho\ell$ is a constant depending on metal parameters, so that the elastic mean free path for Au is expected to be

$$\ell_{Au} = \frac{840}{\rho_\mu} \text{ [Å]} \tag{3.17}$$

For Au wires containing a very small amount of magnetic impurities, Eq. 3.17 can still be used without any modification. For the AuFe spin glass samples in this dissertation ℓ determined by this manner was $\sim$ 200 Å.

3.3.2 Phase coherence length, L_φ

An electron which is understood as a particle in the Drude model actually has a duality in ius nature, *i.e., it is also interpretable as a wave packet*, being represented by $\psi = |\psi|e^{i\varphi}$. Here, φ is referred to as the phase of the electron. The phase coherence length, L_φ is the distance that an electron travels before φ becomes uncorrelated with the initial phase, φ_i. Equivalently, it is defined as the distance that an electron travels during the time τ_φ after which the uncertainty in the phase $\Delta\varphi$ is of order unit,

$$\Delta\varphi \sim \frac{\Delta\varepsilon}{\hbar}\tau_\varphi \sim 1 \tag{3.18}$$

τ_φ is sometimes called as the phase relaxation time. Now let us discuss how an electron loses its phase memory. The scatterers in metals may be divided into the following categories; *static scatterer* and *dynamic scatterer*. The static scatterer includes impurities without an internal degree of freedom, and defects in crystal. When an electron scatters off a static scatterer, the phase change $\Delta\varphi$ is constant in time t; $\Delta\varphi(t) = \Delta\varphi(t + \delta t)$. The electrons even after the scattering process are still coherent with each other.

Dynamic scatterers include lattice vibrations (electron-phonon scattering) and electron-electron interactions. The role of the scatterer in the scattering process varies randomly in time so that there is no stationary relationship between the phases before and after the scattering event; $\Delta\varphi(t) \neq \Delta\varphi(t+\delta t)$. Efficiency in randomizing φ depends on the characteristics of scatterers. For example, in electron-

phonon scattering the short wavelength phonons are more effective in destroying φ [6].

Once τ_φ is known, it is rather straightforward to get the phase coherence length, L_φ. One obvious way to do is by setting

$$L_\varphi = v_F \tau_\varphi \tag{3.19}$$

which is analogous to the relationship between the mean free path (ℓ) and the mean free time (τ). However Eq. 3.19 is valid only in the ballistic scattering regime, where $\tau_\varphi \approx \tau$, which is often the case with high mobility GaAs/AlGaAs heterostructures. For disordered metal films or low mobility semiconductors, the motion of electrons within a distance of order L_φ is already diffusive; that is $\tau_\varphi \gg \tau$. In this case, Eq. 3.19 is replaced by

$$\begin{aligned} L_\varphi &= \sqrt{D\tau_\varphi} \\ \text{where} \quad D &= \frac{1}{d} v_F \ell \end{aligned} \tag{3.20}$$

Here, d is the dimensionality of the sample, and D the diffusion constant for electrons.

Finally we would like to point out that impurity scattering can randomize the phase of electrons if the impurity has an internal degree of freedom. A typical example is a magnetic impurity in a metal, where the spin moment fluctuates with time, working as if it were a dynamic scatterer. Therefore, a small amount of magnetic impurities greatly suppresses L_φ. For this reason, we normally do not

consider L_φ as a relevant length scale in AuFe spin glass wires. For reference, the estimated L_φ for pure Au wires fabricated in our group is typically 3 - 7 μm at 0.3 K. This estimate is obtained by fitting a low field magnetoresistance to the weak localization formula [35].

3.3.3 Thermal length, L_T

If two energy states are correlated with each other, the relative phase φ of electrons in the two states is closely tied to each other. The energy correlation range is given by the Thouless relation $E_c = \hbar D/L^2$ [119], where L is the length over which the correlation extends at a finite temperature T. E_c is the order of $k_B T$, giving rise to a a correlation which extends over a length defined by

$$L_T = \sqrt{\frac{\hbar D}{k_B T}} \tag{3.21}$$

where D is the electron diffusion constant. L_T is called the *thermal length* or *Thouless length*, being typically($\sim 0.27\ \mu\text{m}/\sqrt{T}$ for the AuFe samples in this study.

L_T is the characteristic length scale which determines the dimensionality of the electron-electron (EE) interaction contributions to the resistivity of disordered metals [5]. The importance of the dimensionality of the EE interactions will be discussed in Section 3.4.2.

3.3.4 Size of the Kondo screening cloud; the Kondo length

The Kondo effect arises from the screening of the moment of a magnetic impurity by the conduction electrons in the host metal. As the temperature is decreased, the screening becomes more effective, leading to a logarithmic increase of the resistance. Finally, at temperatures far below the Kondo temperature T_K, the magnetic impurity is completely screened. Physically, the screening can be thought of as arising from a cloud of conduction electrons of dimension ξ_K. Given this physical picture, one expects that distorting this screening cloud might influence the Kondo effect. One way to distort the screening cloud is by reducing the sample dimensions. This idea initiated the series of experiments that were described in Chapter 2.

Dimensional analysis as well as a more rigorous calculation leads to an estimate of the size of the screening cloud!of the form

$$\xi_K \approx \frac{\hbar v_F}{k_B T_K} \tag{3.22}$$

where v_F i the Fermi velocity of the host metal. Physically, one can consider the spin of the conduction electrons in the vicinity of the impurity to be correlated with the impurity spin for a time $\hbar/k_B T_K$. ξ_K is then the distance that an electron at the Fermi energy with a velocity v_F travels in this time. For AuFe, with $T_K \sim 1$ K, $\xi_K \approx 10$ μm. In a dirty metal with electrostatic impurities where the motion of the electron is no longer ballistic but diffusive, this length must be replaced with the diffusion length $\sqrt{\hbar D/k_B T_K}$. For our samples, this diffusive length is much shorter, of the order of 3000 Å.

3.4 Size effect in alloys with dilute magnetic impurities

3.4.1 Finite size dependence in the Kondo effect

Spin-orbit induced magnetic anisotropy in reduced dimensional samples

If a sample becomes smaller than the Kondo screening cloud, the Kondo effect is expected to be different from that in bulk samples. However, as discussed in Chapter PreviousWorkChapter, we cannot draw any definite conclusions from the experiments performed so far for the actual size of the screening cloud, or even for the very existence of such a Kondo screening cloud [34, 38].

Ujsaghy *et al.* [121, 122, 123] proposed a theoretical model in attempt to reconcile the contrasting experimental results. The background of the model is that the conduction electrons which interact with magnetic impurities in alloys also interact with nonmagnetic host atoms through the spin-orbit scattering mechanism. The spin-orbit scattering can have an anisotropy when the motion of a magnetic impurity moment becomes anisotropic for some reason, for example, due to the effect of a nearby sample surface. In this case, the amount of the anisotropy should depend on the volume to surface ratio of samples.

In order to get anisotropic spin-orbit scattering, different angular momentum channels need to taken into account. If $\mathbf{n}$ is an unit vector whose direction is perpendicular to the surface, the Hamiltonian for the anisotropy is given by

$$\mathcal{H} = K(\mathbf{n} \cdot \mathbf{S})^2 \tag{3.23}$$

where **S** is the spin of the magnetic impurity and K the strength of the anisotropy.

The main body of the paper by Ujsaghy *et al.* [123] is a calculation of K, which is a function of the distance of the magnetic impurity d measured from the surface. K turns out to be proportional to d^{-1}. Several implications of the model have been made by Ujsaghy *et al.* [123], and are summarized here:

1. The Kondo temperature T_K is unchanged for $S = 5/2$ and 2. For $S = 2$, the increase in $\rho(T)$ of thin films is not significantly different from bulk value. However, for $S = 5/2$ the situation becomes more complex and the slope in $\rho(T)$ is affected.

2. The Kondo resistivity is reduced by a factor of $1 - 2\lambda_0/t$, where λ_0 is the effective thickness of a surface layer where the spin-orbit induced anisotropy suppresses the Kondo effect, and t the film thickness. For AuFe alloys λ_0 is estimated to be approximately 180 Å. This explains the experimental result from the Purdue group [38] that the Kondo resistivity slope decreases as the thickness of the AuFe film is reduced. When the width (W) of the film is changed in the regime $W \gg t$, very little change of the spin-orbit induced anisotropy is expected. This appears to explain more or less the observation reported by Chandrasekhar *et al.* [34] that the Kondo effect was not modified when the linewidth of AuFe wires was reduced [34]. However, for the narrowest wires measured in that experiment, the width $W \sim 38$ nm was comparable to the film thickness $t \sim 30$ nm, but no suppression of the Kondo

slope was observed in comparison to the widest wires. Furthermore, the slope of the Kondo resistivity for the widest samples was the same as for bulk samples, indicating that the reduced thickness had no effect on the Kondo slope. Hence, the theory does not fully explain the results of Chandrasekhar *et al.*.

3. If magnetic impurities are covered by a non-magnetic film with a long mean free path, they do not experience spin-orbit induced anisotropy. Consequently, the slope of the Kondo resistivity increases, regaining the value in bulk samples as observed in experiment [24].

4. In a Kondo film covered by an extra layer with short mean free path, the anisotropy survives near the interface so that the slope of the Kondo resistivity does not increase significantly as observed in experiment [24].

5. If the Kondo film is covered by materials with negligible spin-orbit interaction, no significant change is expected with regard to the Kondo effect. No experiments have been performed to confirm this effect yet.

Size effect in the disordered Kondo resistivity

While the spin-orbit induced anisotropy explains many observed properties with regard to the size effect in the Kondo resistivity, the calculations in the model assumes that samples are in the clean limit. A few experiments have already focused on effect of disorder on the Kondo anomaly [23, 25, 86]. With regard to the Kondo

problem in the presence of disorder, Ivar Martin *et al.* [96] developed a model to explain the size effect observed in the experiment of Blachly *et al.* [23].

The main idea of the model is that weak localization can lead to a finite size dependence in the Kondo effect. In the paper by Ivar Martin *et al.* the correction to the Kondo resistivity in 2-dimensional films is given by [96]

$$\begin{aligned} \frac{\Delta\sigma}{\sigma} &= \frac{4\tau_0\rho_0 J}{\tau_s^0}\left(1+\frac{2.3\hbar\tau_s^0}{\pi m k_F L\ell^2}\right)\ln\frac{\epsilon_F}{T} \quad \text{for } T_K \ll T < \hbar/\tau_s^0 \\ &= \frac{4\tau_0\rho_0 J}{\tau_s^0}\left(1-\frac{1.2\hbar\tau_s^0}{\pi m k_F L\ell^2}\right)\ln\frac{\epsilon_F}{T} \quad \text{for } \hbar/\tau_s^0 \ll T \end{aligned} \tag{3.24}$$

where τ_0 and τ_s^0 are the nonmagnetic and magnetic scattering times, ρ_0 the density of states at the Fermi level, J the exchange interaction, ℓ the elastic mean free path, and L the film thickness.

In the concentrated magnetic impurity limit $T < \hbar/\tau_s^0$, weak localization enhances the logarithmic increase in resistivity, as was observed in CuFe alloys in the impurity concentration range of 0.3 - 2.1 at% [86]. On the other hand, in the dilute limit $T \gg \hbar/\tau_s^0$, the Kondo effect is suppressed as disorder is increased and the thickness of films is reduced [23].

So far, we have shown that there exist two different models to explain the size dependence in the Kondo anomaly. Depending on the degree of disorder in samples, either of the models can be applied. To be more specific, the criterion for the mechanism given by Ivar Martin *et al.* to dominate is $v_F\tau_s^0/k_F^2 > \ell^2\, min(\lambda_0, \ell)$, where λ_0 is the hindered spin-orbit length [96].

However, one may note that both models does not take into account electron-electron interaction contributions properly. Furthermore, the model proposed by Ivar Martin *et al.* [96] does not take into account the spin-orbit scattering so that it is questionable whether their model can be applied to AuFe systems where the effect of spin-orbit scattering is important.

3.4.2 Electron-electron interaction contribution to $\rho(T)$

In pure Au films, there are three dominant contributions to the resistivity $\rho(T)$ at low temperatures. First, there is the phonon contribution at temperatures T above $\sim$10 K, which gives rise to a rapid increase in $\rho(T)$ as T is increased. Second, there is electron-electron (EE) interaction contribution, and third, a weak localization (WL) contribution. The magnitude of the last two contributions essentially increase as T is reduced, and are dependent on the size of the sample. For quasi 1-dimensional samples, the magnitude of the EE and the WL contributions increase as the widths of wires are reduced, leading to a qualitative deviation from the $\rho(T)$ of bulk samples.

In alloys containing magnetic impurities, the WL contribution is greatly suppressed due to reduction of the electron coherence length arising from electron scattering off magnetic impurities [20]. However, the EE interaction contribution still exists even with magnetic impurities in metals. Thus the EE interaction contribution in quasi 1-dimensional wires should be properly taken into account to see

whether a size dependence in $\rho(T)$ actually originates from the fundamental effect of mesoscopic spin glasses or not.

Normally electron-electron scattering is not expected to affect the resistivity since it conserves the total momentum of the electron system. Even with the Fermi liquid corrections, EE scattering does not bring about any essential temperature dependence of ρ[5]. However, elastic impurity scattering with EE interactions (the Coulomb interactions) produces a non-trivial temperature dependence of the electron density of states and the energy measured at the Fermi level [5]. A correction in $\rho(T)$ is thus expected.

There have been many predictions of the scattering time τ_{ee} for electrons in disordered metals. Schmid [111] and Altshuler *et al.* [9, 10] found a $T^{d/2}$ dependence using a transport equation approach. Abrahams *et al.* [1] obtained the $\ln T$ dependence using impurity averaged perturbation theory.

Altshuler *et al.* obtained a specific functional form for the EE interaction corrections to $\rho(T)$ [5]. Since the characteristic times in problems associated with electron-electron interactions are of the order of T^{-1}, the dimensional crossover for EE interactions occurs when the sample dimension becomes comparable to $L_T = \sqrt{\hbar D/k_B T}$. The corrections to the resistivity are given by [5]

$$\begin{aligned} \delta\rho_{ee} &= A_1 \frac{R_\Box^2 t}{(\pi\hbar/e^2)W} L_T \qquad \text{for } d=1 \\ &= -\frac{e^2 R_\Box^2 t}{2\pi^2\hbar} \ln \frac{k_B T}{(\hbar/\tau)} \qquad \text{for } d=2 \\ &= A_3 \frac{e^2\rho^2}{2\pi^2\hbar} \frac{1}{L_T} \qquad \text{for } d=3 \end{aligned} \tag{3.25}$$

where W is the width and t the thickness of the film, and $1/\tau$ the total scattering rate. $R_\Box$ ($\equiv \rho/t$) is the sheet resistance. The numerical values for the coefficients are given by [5]

$$\begin{aligned} A_1 &= -3\sqrt{2}\,\Gamma(\frac{1}{2})\,\zeta(-\frac{1}{2}) \approx 1.56 \\ A_3 &= \frac{\sqrt{2}}{6}\,\Gamma(\frac{3}{2})\,\zeta(\frac{1}{2}) \approx -0.61 \end{aligned} \tag{3.26}$$

Looking at the sign of A_d carefully, one might notice that the correction to $\rho(T)$ grows with decreasing temperature regardless of sample dimension. When electron screening is taken into account, A_d is expected to be modified [5].

As mentioned above, the dimensionality is determined by the length scale L_T. At low temperature, the magnitude of L_T can easily be on the order of $\sim$ 1000 Å, which is frequently comparable to the widths of samples. Therefore, the samples would be in the intermediate regime between 1-dimension and 2-dimension, and the functional form of Eq. 3.25 is not immediately applicable. To treat this intermediate regime, we proposed [104] a functional form ρ_{ee}^{q1} for the EE interaction correction for quasi 1-dimensional samples, which is given by

$$\delta\rho_{ee}^{q1} = \alpha \frac{R_\Box^2 t}{(\pi\hbar/e^2)W} \sum_{n=0}^{\infty} \frac{1}{\sqrt{(1/L_T)^2 + (n\pi/W)^2}} \tag{3.27}$$

where $R_\Box$ is the sheet resistance of a film, W the linewidth, and t the film thickness. α is a numerical constant which takes into account the effect of electron screening. Eq. 3.27 has been obtained under the assumption that the EE interaction correction to the conductivity (or, resistivity) in disordered conductors can be calculated

in a manner analogous to the weak localization correction. We will give a brief explanation for this scheme in what follows.

The weak localization correction to the conductivity of disordered metals is given by [59]

$$\delta\sigma(\omega) = -\frac{2De^2}{\pi\hbar}\int \frac{d\mathbf{Q}}{D\mathbf{Q}^2 - i\omega} \tag{3.28}$$

where D is the diffusion constant. Phenomenologically, $-i\omega$ can be replaced by $1/\tau_\varphi$ to take into account the effect of finite electron phase coherence [12], and hence Eq. 3.28 leads to

$$\begin{aligned} \delta\sigma &= -\frac{e^2}{\pi\hbar}L_\varphi \qquad d=1 \\ &= -\frac{e^2}{2\pi^2\hbar}\ln\frac{\tau_\varphi}{\tau} \qquad d=2 \\ &= \frac{e^2}{2\pi^2\hbar}\frac{1}{L_\varphi} \qquad d=3 \end{aligned} \tag{3.29}$$

For the EE interaction correction an assumption we assume instead that $-i\omega$ should be replaced by $1/\tau_T$ ($\equiv (\hbar/k_BT)^{-1}$) . Then Eq. 3.28 leads to the exactly the same formula as Eq. 3.29, except that L_φ is replaced by L_T, eventually leading to the same formulae for the resistivity correction as in Eq. 3.25.

In a sample of finite size the integral in Eq. 3.28 is replaced by a sum. Therefore we write the EE interaction correction formula as follows,

$$\delta\sigma = -\frac{2e^2}{\pi\hbar}\frac{1}{LWt}\sum_{Q_x,Q_y,Q_z}\frac{1}{Q_x^2+Q_y^2+Q_z^2+L_T^{-2}} \tag{3.30}$$

where

$$Q_x = \frac{n\pi}{W}, \qquad Q_y = \frac{m\pi}{L}, \qquad Q_z = \frac{l\pi}{t} \tag{3.31}$$

l, m, n are integers, and L, W, t are the sample dimensions. L_T is given by $\sqrt{\hbar D/k_B T}$. In metal films t is usually much smaller than L_T so that only the $l = 0$ contribution is dominant in the sum. If $L \gg L_T$, we restore the sum to an integral and obtain

$$\begin{aligned} \delta\sigma &= -\frac{e^2}{\pi\hbar}\frac{1}{Wt}\sum_{Q_x}\int_{-\infty}^{+\infty}\frac{dQ_y}{Q_y^2 + (n\pi/W)^2 + L_T^{-2}} \\ &= -\frac{e^2}{\pi\hbar}\frac{1}{Wt}\sum_{n=0}^{\infty}\frac{1}{\sqrt{(1/L_T)^2 + (n\pi/W)^2}} \end{aligned} \tag{3.32}$$

Using the relation $\delta\rho = -\delta\sigma/\sigma^2$, Eq. 3.32 gives the functional form of the EE interaction correction for the quasi 1-dimensional sample, expressed in Eq. 3.27.

Since we have justified the functional form in Eq. 3.27, we are ready to use the EE interaction correction for the quasi 1-dimensional case. In practical applications of Eq. 3.27 we are only interested in the relative magnitude difference of the EE interaction correction below the temperature T_0 ($\approx$ 10 K) where $\rho(T)$ of spin glass AuFe wires has a minimum. Therefore the magnitude difference of the EE interaction correction can be expressed as

$$\begin{aligned} \delta\rho_{ee}^{q1}(T) - \delta\rho_{ee}^{q1}(T_0) &= \alpha\frac{R_\square^2 t}{(\pi\hbar/e^2)W} \\ &\times \sum_{n=0}^{\infty}\left[\frac{1}{\sqrt{(1/L_T)^2 + (n\pi/W)^2}} - \frac{1}{\sqrt{(1/L_{T_0})^2 + (n\pi/W)^2}}\right] \end{aligned} \tag{3.33}$$

The prefactor α, the screening factor, is used as a fitting parameter when the functional form of ρ_{ee}^{q1} is used to correct the observed raw $\rho(T)$ of 1 and 2-dimensional samples. For a set of samples from a single evaporation the prefactor α should be the same. We found that $\alpha \approx 1.5$ for AuFe spin glass samples in this study. To

our surprise this value is comparable to the calculated value without any screening (see Eq. 3.26).

To make the proposed functional form $\delta\rho_{ee}^{q1}$ valid, one should reproduce the same result as $\delta\rho_{ee}$ of Eq. 3.25 in the limits of $d = 1$ and 2. We now show that ρ_{ee}^{q1} properly restores ρ_{ee} for the 1 and 2-dimensional cases. Since the sum in Eq. 3.27 is actually divergent, we introduce an upper cutoff in the summation. Let us first consider the 1-dimensional limit, where $W \ll L_T$. The term which makes the dominant contribution to ρ_{ee}^{q1} is the $n = 0$ term. In this case ρ_{ee}^{q1} can be approximated as follows:

$$\delta\rho_{ee}^{q1} \approx \alpha \frac{R_{\Box}^2 t}{(\pi\hbar/e^2)W} L_T \tag{3.34}$$

Consequently $\delta\rho_{ee}^{q1}$ is the same as the formula for $d = 1$ as in Eq. 3.25.

For the 2-dimensional limit ($W \gg L_T$), we cannot ignore the higher order terms in ρ_{ee}^{q1}. Using the fact that $W \gg L_T$ in 2-dimensional samples, one can replace the summation by an integral. We show that $\delta\rho_{ee}^{q1}$ restores $\delta\rho_{ee}$ for 2-dimensions in Eq. 3.25, as follows:

$$\begin{aligned}
\delta\rho_{ee}^{q1} &= \alpha \frac{R_{\Box}^2 t}{(\pi\hbar/e^2)W} \sum_{n=0}^{\infty} \frac{1}{\sqrt{(1/L_T)^2 + (n\pi/W)^2}} \\
&= \alpha \frac{R_{\Box}^2 t}{(\pi\hbar/e^2)W} \sum_{n=0}^{\infty} \frac{W}{\pi\sqrt{(\frac{W}{\pi L_T})^2 + n^2}} \\
&\approx \alpha \frac{R_{\Box}^2 t}{(\pi\hbar/e^2)W} \frac{W}{\pi} \int_0^{\Gamma} dx \frac{1}{\sqrt{(\frac{W}{\pi L_T})^2 + x^2}} \\
&= \alpha \frac{R_{\Box}^2 t}{(\pi\hbar/e^2)W} \frac{W}{\pi} \ln \frac{\Gamma + \sqrt{\Gamma^2 + (W/\pi L_T)^2}}{W/\pi L_T}
\end{aligned}$$

$$\begin{aligned} &\approx \alpha \frac{e^2 R_\square^2 t}{2\pi^2 \hbar} \ln \frac{2\Gamma}{W/\pi L_T} \\ &= -\alpha \frac{e^2 R_\square^2 t}{2\pi^2 \hbar} \ln \frac{k_B T}{\hbar/\tau} \end{aligned} \tag{3.35}$$

where we have used the assumption that the upper cutoff Γ is much bigger than $W/\pi L_T$'. In the last step we replaced Γ by $W/2\pi\sqrt{D\tau}$.

3.5 Differential resistance and thermoelectric effect

3.5.1 Heat flow model in metallic wires; Nagaev's equation

In normal transport measurements people frequently use a small ac signal as a probe current. By measuring the response from the sample at the frequency corresponding to the input ac signal, the linear transport properties of samples are obtained. Although a small dc signal can be used as a probing excitation, it is generally not a good idea to use it for the following reasons. First of all, it is very hard to remove the small dc voltage drift ($\sim 0.1 - 1\mu$V) which may arise from varying thermoelectric potential in the measurement circuit. Secondly, the normal circuit components for the transport measurement contain $1/f$ noise (also known as pink noise), which becomes larger at lower frequency [68]. Consequently we used an ac differential technique in our measurement.

In addition to the advantages described in the previous paragraph, dV/dI can also be used as a tool to investigate electron heating effects in samples if a dc bias current I is superposed on top of the small ac probing current I_{ac}. When $I = 0$,

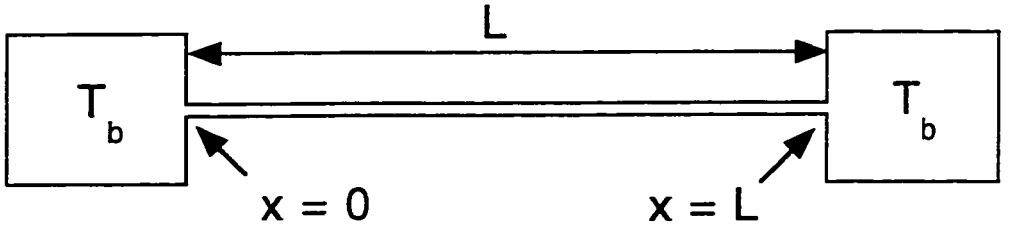

Figure 3.6: 1-dimensional metal wire with a dc current flow. The two electrical contacts are large so that the electron temperature at the contacts is assumed to be the same as the bath temperature T_b. x represents the position in a wire.

dV/dI just gives the normal resistance $R(T)$. When a dc current I flows through a metal wire, the external power input I^2R supplies an energy input to the electron system. The conduction electrons heat up and transfer their excess energy to the environment. Now, an interesting question is how much the electrons are heated up and what is the temperature of the conduction electrons T_e after the stabilization of the heat flow. In what follows, we analyze the resulting heat flows in metal wires and provide a model heat flow equation to predict T_e in metal wires.

T_e in a metal normally depends on three factors; the power input by Joule heating, the power loss through electronic thermal conduction to the electrical contacts, and the power loss through the electron-phonon interaction. We assume that phonons in metals are well thermalized to the bath temperature T_b of the silicon substrate. We now discuss these three factors one by one.

Let us assume that a dc bias current I flows through a metal wire of a length L, as drawn in Fig. 3.6. The power input, $\mathcal{P}_1$, of the section with length δx due to

Joule heating is given by

$$\mathcal{P}_1 = I^2 \rho \frac{\delta x}{A} \tag{3.36}$$

where ρ is the resistivity, and A the cross section of the metal wire, and x the position along the wire.

Now let us consider cooling mechanisms. Thermal current flows in a direction opposite to the temperature gradient, given in the form of $-\kappa \nabla T$. Here κ represents the thermal conductivity, which is $\sim$ 3.1 watt-cm/K for Au at 273 K [13]. In the metal wire of Fig. 3.6, the electronic thermal current, $\mathcal{P}_2$, of the section with length δx becomes

$$\begin{aligned} \mathcal{P}_2 &= -\kappa \frac{\partial}{\partial x} T_e(x + \delta x) + \kappa \frac{\partial}{\partial x} T_e(x) \\ &= -\delta x \frac{\partial}{\partial x} \left(\kappa \frac{\partial}{\partial x} T_e \right) \end{aligned} \tag{3.37}$$

From the law of Wiedemann and Franz within the Sommerfeld approximation, we find the relationship [13]

$$\frac{\kappa}{\sigma T} = \frac{\pi^2}{3} \left(\frac{k_B}{e} \right)^2 \tag{3.38}$$

By putting Eq. 3.38 into Eq. 3.37, the power transfer $\mathcal{P}_2$ by electronic thermal conduction is given by

$$-\frac{\pi^2}{3} \left(\frac{k_B}{e} \right)^2 \frac{1}{\rho} \delta x \frac{\partial}{\partial x} \left(T_e \frac{\partial}{\partial x} T_e \right) \tag{3.39}$$

Another way for hot elecurons to dissipate their energy is through the emectron-phonon interaction. Electrons lose their excess energy ($c_e dT$) at the electron-phonon

scattering rate τ_{e-ph}^{-1}. Here c_e $(= \gamma T)$ is the electronic specific heat for the normal metal at low temperature. The proportionality constant $\gamma \approx \pi^2 n k_B^2 T/2\varepsilon_F$, being 67.2 J/m^3K for Au. Assuming that the phonons in the metal film are at the same temperature as the substrate temperature, T_b, the power transfer $\mathcal{P}_3$ due to the electron-phonon interaction is

$$\mathcal{P}_3 = \int_{T_b}^{T_e} \frac{c_e dT}{\tau_{e-ph}} A\delta x \tag{3.40}$$

Here n is number density of conduction electrons in the metal and ε_F the Fermi energy, which is $\sim$ 5.5 eV for Au.

To get an explicit form for $\mathcal{P}_3$, one needs to know the temperature dependence of τ_{e-ph}^{-1}. The electron-phonon scattering rate τ_{e-ph}^{-1} also depends on T. The general functional form of the electron phonon scattering rate τ_{e-ph}^{-1} can be expressed by [78]

$$\frac{1}{\tau_{e-ph}} \sim \int d\omega \frac{\alpha^2 F(\omega)}{sinh(\hbar\omega/k_B T)} \tag{3.41}$$

where $\alpha^2 F(\omega)$ is the Eliashberg function which is closely related to the details of the electron phonon scattering process. For a clean metal in the Debye approximation, $\alpha^2 F(\omega)$ is proportional to ω^2. Hence, electron-phonon scattering rate $\tau_{e-ph}^{-1} \propto T^3$ for $k_B T \ll \hbar\omega_D$, where ω_D is the Debye frequency. In the presence of a large number of impurities, the electron-phonon interaction is modified, giving a deviation from the T^3 dependence discussed above. However, there is no general agreement on the form of τ_{e-ph}^{-1} in dirty limit. For examples, Keck and Schmid [78] obtained $\tau_{e-ph} \propto T^4$, while Bergmann [21] and Takayama [117] calculated $\tau_{e-ph}^{-1} \propto T^2$. Furthermore, a

temperature dependence of τ_{e-ph} which is not describable by a power law has been also found in the dirty limit [14].

We use the relation $\tau_{e-ph}^{-1} \propto T^3$ under the assumption that the samples in this study are in the clean limit. The justification for the assumption of clean limit is given as follows. The determination whether our samples are in the clean or the dirty limit involves some length scale. In the case of the electron-phonon interaction, the inverse of the phonon wave vector $q_{ph} = 4k_BT/\hbar v_s$ is a good candidate for a length scale. Here v_s is the sound velocity in the metal, which is $\sim$ 3200 m/sec for Au. For samples in this study, $q_{ph}^{-1} \approx$ 50 - 100 Å, which is smaller than the elastic mean free path $\ell \sim$ 200 Å, so that the samples are nominally in the clean limit.

Using $\tau_{e-ph} = \Lambda T^{-3}$, $\mathcal{P}_3$ in Eq. 3.40 is rewritten as

$$\frac{1}{5}\gamma\Lambda A\delta x(T_e^5 - T_b^5) \tag{3.42}$$

Using the fact that the total heat flow in and out of the sample is zero; $\mathcal{P}_1 - \mathcal{P}_2 - \mathcal{P}_3 = 0$, we finally reach a model heat flow equation:

$$\frac{\pi^2}{3}k_B^2L^2\frac{\partial}{\partial x}\left(T_e\frac{\partial T_e}{\partial x}\right) = -(eIR)^2 + \frac{\gamma\Lambda e^2L^2\rho}{5}(T_e^5 - T_b^5) \tag{3.43}$$

Nagaev derived the same result by a sightly different method using a diffusion equation for the distribution function [101], where the coefficient $\gamma\Lambda e^2L^2\rho/5$ was replaced by $24\zeta(5)\alpha_{ph}L^2k_B^5/(k_B\Theta_D)^2(\hbar D)$. Here $\zeta(5)$ is Riemann's zeta function, Θ_D the Debye temperature, and α_{ph} electron-phonon coupling constant. The value of α_{ph} ($\sim$ 0.415) is obtained from noise thermometry studies for Au films on sil-

icon substrates [66]. By solving Eq. 3.43 numerically with appropriate boundary conditions, the profile of $T_e(x)$ along the wire for a given dc current flow can be estimated. The boundary condition can be as simple as $T_e(x=0) = T_e(x=L) = T_b$ for a single wire as in Fig. 3.6, while more complicated boundary conditions are expected for a configuration of multiple wires.

Before moving on to the discussion of boundary conditions, we examine the coupling between the phonons of metals and the phonons in the silicon substrate. The temperature under our control is not the temperature of the metal film but the temperature T_b of the silicon substrate on which the metal film sits. Let the relaxation time τ_b represents the characteristic time involved in the coupling between two systems. If τ_b is compared to τ_{e-ph}, the energy transfer mechanism between the phonons of the two systems should be seriously taken into account.

Bergmann *et al.* argued that phonon propagation through the interface between a metal and a quartz is similar to black-body radiation [16]. Let U_f be the energy density in the metal film. The energy that escapes through the interface is given by

$$\frac{dU_f}{dt} = \frac{c}{4\lambda_{ph}} U_f, \qquad \tau_b = \frac{4\lambda_{ph}}{c} \tag{3.44}$$

where c is the longitudinal sound velocity, and λ_{ph} the phonon wave length which is given by $\hbar c/4k_BT$. Therefore τ_b is given by $\hbar/k_BT$ ($\sim 7.6/T \times 10^{-12}$ seconds), which is much smaller than τ_{e-ph} ($\sim 1/T^3 \times 10^{-7}$ seconds) at low temperatures. Therefore, the temperature of the phonons in metals is controlled effectively just

by controlling the temperature T_b of the silicon substrate.

3.5.2 Boundary conditions for Nagaev's equation

To solve Nagaev's equation (Eq. 3.43) numerically, we need to know the appropriate boundary conditions. The boundary conditions usually depend on the geometry of the samples. Here we just take two geometries which have been frequently used during the experiments in this study.

Single wire

Figure 3.6 shows the simplest geometry of a sample one may measure, a single wire without any voltage probes. Both ends of the wire are attached to large electrical contacts, at which the electron temperature T_e is assumed equal to T_b. The boundary condition for this geometry is simply

$$T_e(x=0) = T_e(x=L) = T_b$$

or, equivalently

$$T_e(x=0) = T_b \quad \text{and} \quad \left.\frac{dT_e}{dx}\right|_{x=L/2} = 0 \tag{3.45}$$

where L is the length of the wire.

With the boundary condition Eq. 3.45, the electron temperature profile $T_e(x)$ of the single metal wire was calculated by Nagaev's equation at three different dc currents $I = 3$, 10, and 40 μA. The parameters used for the coefficients in Nagaev's equation are $T_b = 0.45$ K, $D = 105$ cm^2/sec, $W = 110$ nm, $L = 35.4$ μm, $R_\square = 1.22$

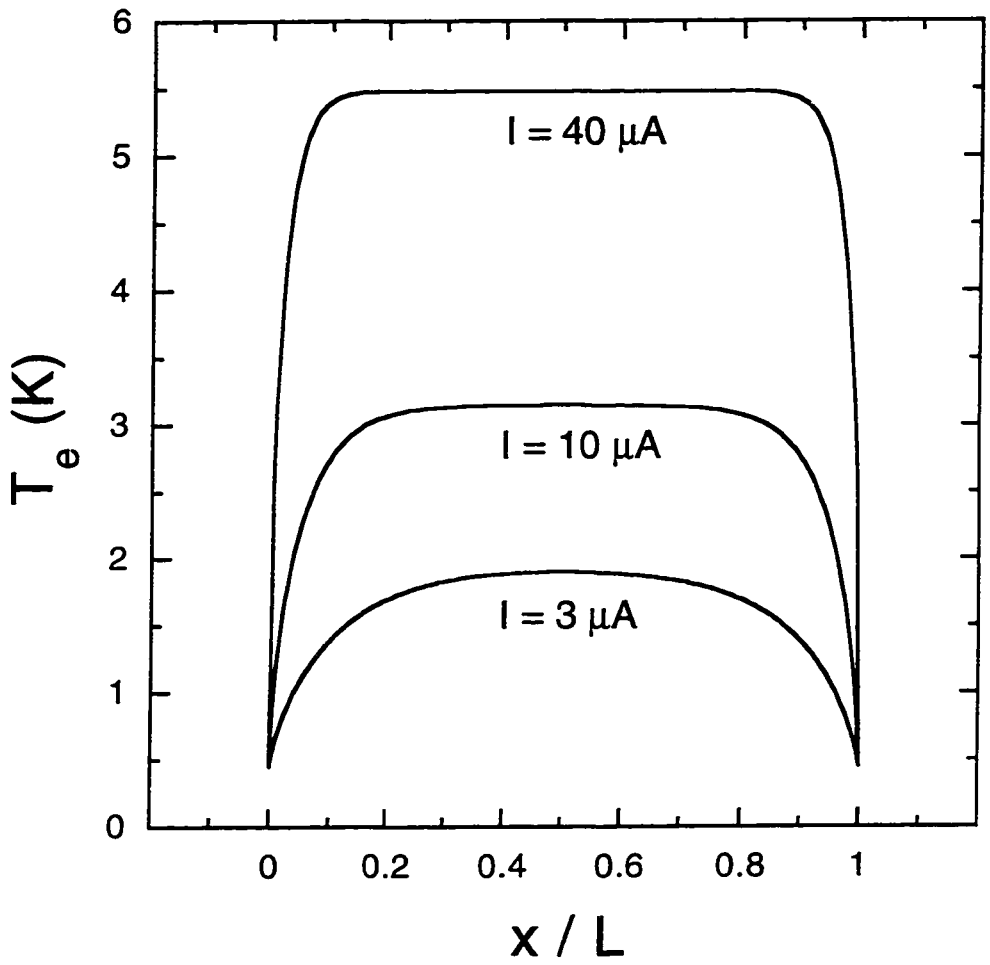

Figure 3.7: Electron temperature profile, $T_e(x)$ of a single metal wire for three different dc currents $I = 3$, 10, and 40 μA. The two electrical contacts are large so that T_e at the electrical contact is assumed to be the same as the bath temperature $T_b(= 0.45K)$. x/L represents the normalized position in the wire.

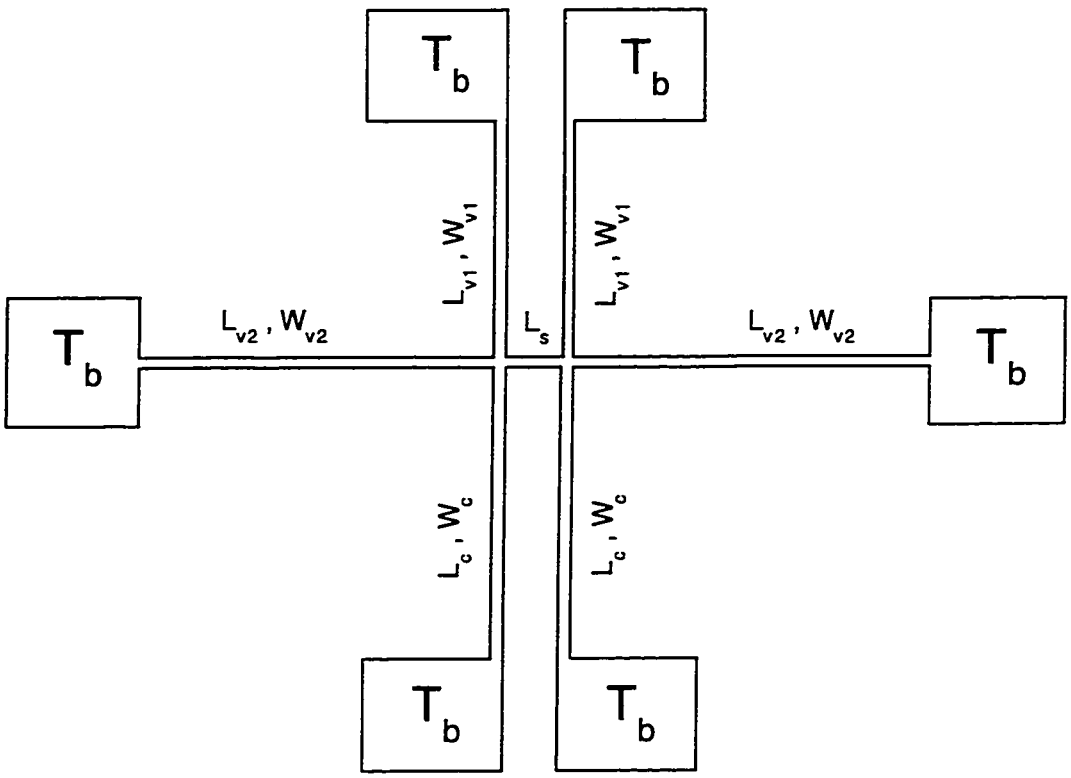

Figure 3.8: Schematic of a multi-probe sample. The subscripts $v1$, $v2$, c, and s represent the vertical voltage line, the horizontal voltage line, the current line, and the sample segment, respectively. L represents the length of the lines, and W the linewidth. The structure consists of one short sample section in the middle and 6 lines which are attached to the sample.

Ω, $\Theta_D = 170$ K, and $\alpha = 0.415$. The resulting $T_e(x)$ is shown in Fig. 3.7. The profile shows a rapid drop of T_e in the vicinity of the electrical contacts, indicating that cooling by electronic thermal conduction occurs most efficiently near the electrical contacts.

Multi-probe structure

Figure 3.8 shows a multi-probe structure similar to the multi-probe AuFe wires

in this study. The subscripts $v1$, $v2$, c, and s represent the vertical voltage line, the horizontal voltage line, the current line, and the sample segment, respectively. L represents the length of the line, and W the width of the line. The structure consists of one short sample section and 6 lines which are attached to the sample. Two out of the 6 lines are current carrying lines, the rest four being voltage probes. For simplicity, we assume that T_e within the sample section does not change with position, *i.e*, T_e is assumed fixed at a constant temperature T_s.

We have three different equations; one for the current lines, and two more for the voltage lines. The equations are

$$\begin{aligned}
\frac{\pi^2}{3}k_B^2 L_c^2 \frac{\partial}{\partial x}\left(T_c \frac{\partial T_c}{\partial x}\right) &= -(eIR_c)^2 + \eta_c \frac{k_B^2}{\Theta_D^3}(T_c^5 - T_b^5) \\
\frac{\pi^2}{3}k_B^2 L_{v1}^2 \frac{\partial}{\partial x}\left(T_{v1} \frac{\partial T_{v1}}{\partial x}\right) &= \eta_{v1} \frac{k_B^2}{\Theta_D^3}(T_{v1}^5 - T_b^5) \\
\frac{\pi^2}{3}k_B^2 L_{v2}^2 \frac{\partial}{\partial x}\left(T_{v2} \frac{\partial T_{v2}}{\partial x}\right) &= \eta_{v2} \frac{k_B^2}{\Theta_D^3}(T_{v2}^5 - T_b^5)
\end{aligned} \tag{3.46}$$

where the dimensionless parameter $\eta_c = 24\zeta(5)\alpha_{ph}L_c^2 k_B \Theta_D/\hbar D$, and η_{v1}, η_{v2} are defined similarly.

The first boundary condition comes from the fact that T_e is equal to T_b at the electrical contacts:

$$T_c(x=0) = T_{v1}(x=0) = T_{v1}(x=0) = T_b \tag{3.47}$$

and the second boundary condition comes from the assumption that T_e of the short sample section is constant:

$$T_c(x=L_c) = T_{v1}(x=L_{v1}) = T_{v2}(x=L_{v2}) = T_s \tag{3.48}$$

Finally the last boundary condition is from the continuity equations for heat flow at the nodes around the sample. If we use '+' for heat flow out and '−' for heat flow in, the total heat flow at the node in steady state is given by

$$-\kappa_c W_c t \frac{dT_c}{dx}\bigg|_{x=L_c} - \kappa_{v1} W_{v1} t \frac{dT_{v1}}{dx}\bigg|_{x=L_{v1}} - \kappa_{v2} W_{v2} t \frac{dT_{v2}}{dx}\bigg|_{x=L_{v2}} = 0 \qquad (3.49)$$

where $\kappa_c = \pi^2 (k_B/e)^2 \sigma T_c/3$, and κ_{v1}, κ_{v2} are defined similarly. t is the thickness of the metal film. Therefore Eq. 3.49 is rewritten as

$$-W_c T_c \frac{dT_c}{dx}\bigg|_{x=L_c} - W_{v1} T_{v1} \frac{dT_{v1}}{dx}\bigg|_{x=L_{v1}} - W_{v2} T_{v2} \frac{dT_{v2}}{dx}\bigg|_{x=L_{v2}} = 0 \qquad (3.50)$$

Now we have found a complete set of boundary conditions for the structure in Fig. 3.8.

With the boundary conditions Eqs. 3.47, 3.48, and 3.50, the electron temperature profile $T_e(x)$ of the current line is calculated using Nagaev's equation (Eq. 3.46) for three dc currents I = 3, 10, and 40 μA. The parameters used for the coefficients in Nagaev's equation are T_b = 0.45 K, D = 105 cm^2/sec, W_c = 110 nm, L_c = 15.5 μm, W_{v1} = 110 nm, L_{v1} = 24.5 μm, W_{v2} = 60 nm, L_{v2} = 24.5 μm, $R_\square$ = 1.22 Ω, Θ_D = 170 K, and α = 0.415. The resulting $T_e(x)$ of the current line is shown in Fig. 3.9. The profile shows not only the rapid drop of T_e in the vicinity of the electrical contacts but also a drop at the node where the sample section is connected, due to the cooling effect of the voltage probes.

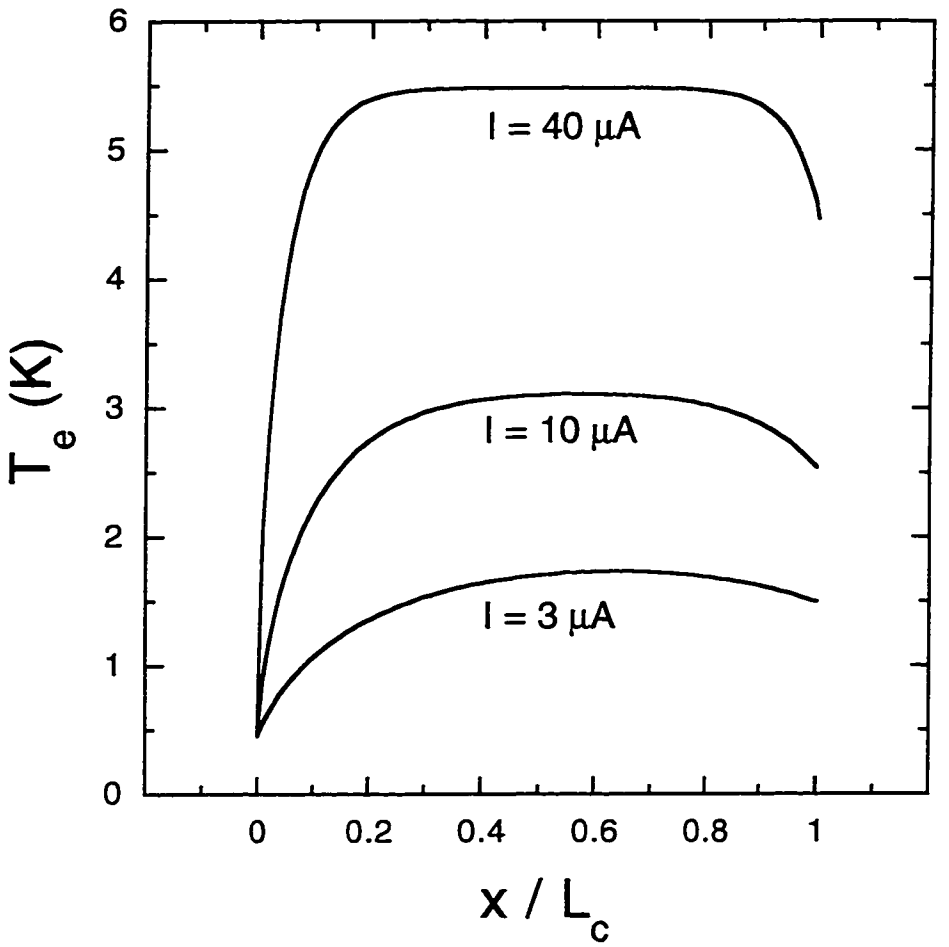

Figure 3.9: Electron temperature profile $T_e(x)$ of the current line in the multi-probe structure. (See Fig. 3.8.) $T_e(x)$'s are obtained for three different dc bias currents I = 3, 10, and 40 μA. The electrical contacts are large so that T_e at the electrical contact is assumed to be same as the bath temperature T_b (= 0.45 K). x/L_c represents the normalized position in the current wire.

3.5.3 *Thermoelectric effect in $dV/dI(I)$ measurements*

In differential resistance $dV/dI(I)$ measurements at low temperature the major role of I is heating of the electron system as discussed in Section 3.5.1. Therefore, $dV/dI(I)$ reflects the behavior of $R(T)$. Furthermore, one would expect a completely symmetric $dV/dI(I)$ since the heating of a resistive wire by I is independent of the direction of I. However, we found [50, 103] that $dV/dI(I)$ of AuFe wires becomes asymmetric in I when the widths of the voltage probes are different from each other, one of the voltage probes being narrower than $W \sim 150$ nm. Although a simple electron heating picture cannot explain the asymmetry, the thermoelectric effect associated with heating explains the asymmetry in $dV/dI(I)$. As I heats up the electrons in a sample, two voltage probes work as a thermocouple and give rise to a finite voltage if the thermopower of the two voltage probes is different from each other.

Let us consider how an asymmetric $dV/dI(I)$ can be detected when two voltage probes have different thermopowers, $S_{v+} \neq S_{v-}$ (see Fig. 3.10). A dc current I flows through two current terminals $I+$ and $I-$, heating up the short sample section in the middle of the wire. Then, the total voltage measured between the $V+$ and $V-$ electrical contacts is given by

$$\begin{aligned} V &= IR + V_{th} \\ &= IR + \int_{T_b}^{T_M(I)} (S_{v+}(T_e) - S_{v-}(T_e)) dT_e \end{aligned} \tag{3.51}$$

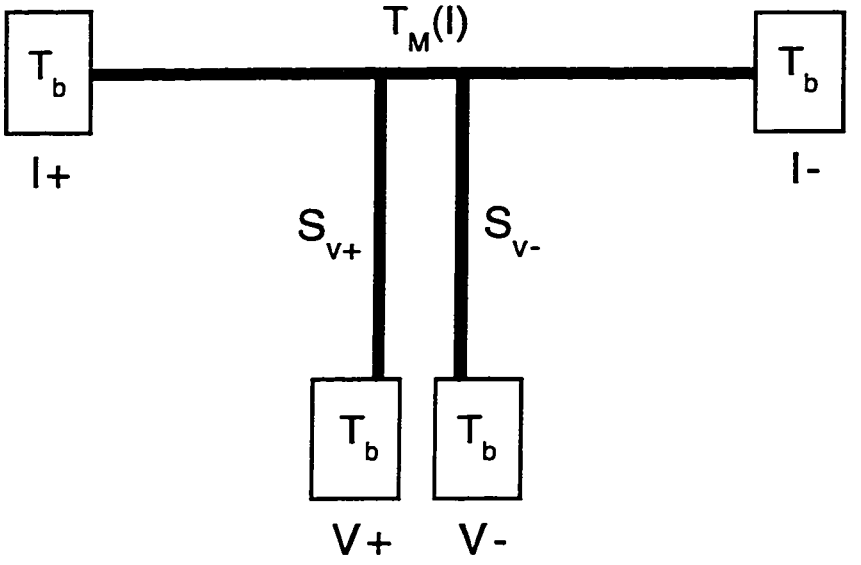

Figure 3.10: Schematic of a sample which has an asymmetry in $dV/dI(I)$. If two voltage probes have different thermopowers ($S_{v+} \neq S_{v-}$), $dV/dI(I)$ becomes asymmetric in I.

where $T_M(I)$ is the electron temperature of the sample section with a dc current I. By differentiating Eq. 3.51, the antisymmetric part of the differential resistance is obtained:

$$\left(\frac{dV}{dI}\right)_A = (S_{v+} - S_{v-})\frac{dT_M}{dI} \tag{3.52}$$

Since $T_M(I)$ is symmetric in I, dT_M/dI is antisymmetric in I.

Once $T_M(I)$ is known, either by a calculation or using a local thermometer, we can estimate $\Delta S(= S_{v+} - S_{v-})$ between the two voltage probes as a function of T_M using Eq. 3.52. If one of the voltage probes has negligible thermopower ($S_{v-} \approx 0$), the thermopower of the other voltage probe is directly obtained from a $dV/dI(I)$ measurement. This fact has been found to be extremely useful for thermopower

measurements at very low temperature [51].

Chapter 4

EXPERIMENTAL TECHNIQUES

Technical particulars regarding sample fabrications and measurements are discussed in this chapter. The primary techniques used for fabricating samples in this study is photolithography and electron beam lithography. We also discuss the low temperature transport measurement techniques employed in this study.

In Appendix A we list references for chemicals, electronic components, and measurement apparatus which appear in this chapter.

4.1 Sample fabrication

The samples in this study are basically thin metal films evaporated on top of a silicon substrate. The silicon substrate actually has an insulating top layer, which allows us to check the electrical continuity of samples at room temperature.

Structurally, the samples consist of two parts; a big pattern and a small pattern. The big pattern is on the order of 500 μm, and is meant for easy electrical bonding. The big pattern is also made of the same material as the small patterns. Since it has a large area, big patterns are fabricated by a photolithographical technique. Using photolithography we can make many big patterns simultaneously in a single

fabrication step. The most essential and delicate part of the sample is made by using an electron beam lithographical technique. By this technique, we can fabricate a very narrow metal wires with linewidth $\sim$ 600 Å, comparable to the mean free path. With its flexibility in designing patterns, electron beam lithography is a reliable technique for the fabrication of mesoscopic samples.

4.1.1 Wafer preparation

The first step in the fabrication process is finding a suitable substrate. All the substrates used in this study are 0.020″ inch thick Si (100) wafers with an oxidized top layer. The SiO_2 top layer makes it possible to check the electrical continuity of samples at room temperature.

The clean surface of the top layer is extremely important since the thickness of metal film is just a few hundred Å. Any small particles on the surface can destroy the entire sample, and hence a substrate cleaning process is necessary. The following steps explain the substrate cleaning process which we employed in this study:

1. Clean substrates ultrasonically for 3 minutes in deionized water.

2. Clean substrates ultrasonically for 3 minutes in 2-propanol ('isopropanol').

3. Clean substrates ultrasonically for 3 minutes in acetone.

4. Clean substrates ultrasonically for 1 minute in methanol.

5. Rinse substrates with methanol and blow with dry N_2 gas immediately.

4.1.2 Photolithography

The following steps outline the photolithographical process which we employed in this study. The entire process was done in a clean room.

1. Right after the substrate cleaning process, the substrate is spun to coat photoresist. Microposit S1813 Photo Resist was used. Spin speed is 5000 rpm and spin time is 60 seconds. Thickness of coating layer is approximately 1.1 μm.

2. The substrate is baked in a oven at 90 °C for 30 minutes. This process removes the solvent in the resist layer, and hardens it. After baking, the substrate is cooled on a bench top for 10 minutes.

3. The photoresist layer is a single layer, and hence it does not make an undercut profile after development. An undercut profile makes for better liftoff. To have an undercut profile, the top surface of the photoresist layer is hardened by soaking in chlorobenzene for 1 minute.

4. The substrate and a photomask are aligned in a Quintel Q-2001CT mask aligner. Using 190 watt arc lamp, the photoresist is exposed for 15 seconds.

5. the substrate is immersed in photoresist developer. Microposit MF-319 De-

veloper is used. Development normally takes 45 seconds at 20 °C. Right after developing, the residue of the developer is removed by flushing the substrate with deionized water.

6. Thin metal films are deposited on the substrate. The detailed metal deposition process will be discussed in Section 4.1.4.

7. The sample is soaked in acetone for 30 minutes to lift off unwanted metal parts.

4.1.3 Electron beam lithography

Once the large pattern is made, the most sensitive part, which is on the order of μm, is made by using electron beam (e-beam) lithography. First, substrates are re-cleaned in a rather soft way so as not to damage the big pattern.

1. Clean ultrasonically for 30 seconds in acetone.

2. Rinse with deionized water.

3. Flush by acetone.

4. Finally rinse with methanol and blow dry immediately.

Now the substrate is ready to be spin-coated with polymethylmethacrylate (PMMA). We used a commercial PMMA (NANO PMMA RESIST by Microlithography Chemical Corp.), for which the solvent is Anisole. For better liftoff we need

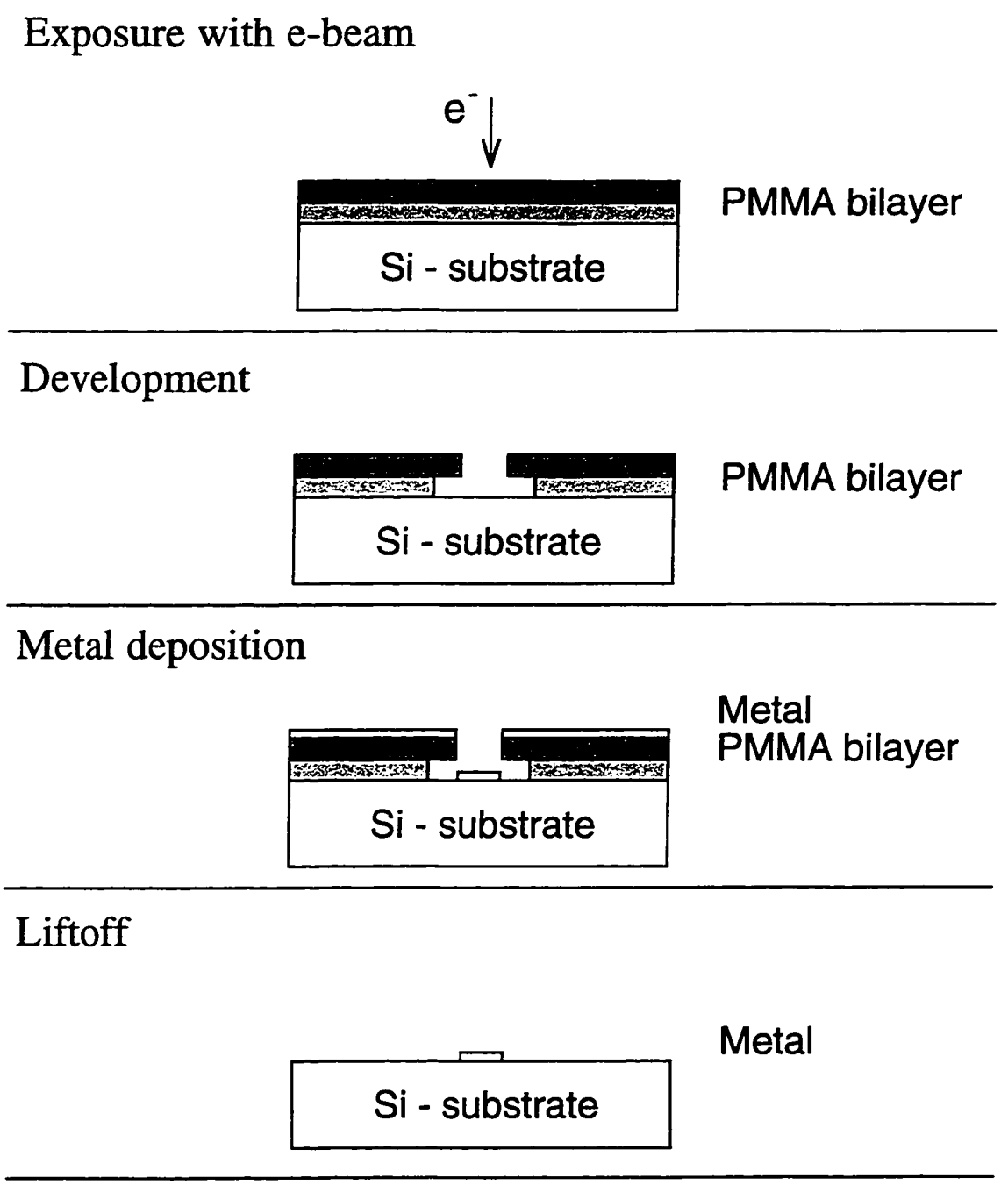

Figure 4.1: Fabrication steps of e-beam lithography. Fabrication steps of photolithgraphy are similar except for the exposure step.

an undercut profile. To make an undercut, we used bilayer resists of two different molecular weight PMMA's. The heavier weight PMMA is less sensitive to e-beam. Therefore the lighter weight PMMA (100K) is spun as the first layer, and the heavier weight PMMA (495K) as the second layer. The following steps explain the processes which are used to make each PMMA layer:

1. PMMA solution is dropped to cover the entire substrate surface.

2. The substrate is spun at 3000 rpm for the first PMMA layer (7000 rpm for the second layer). The spin time is 1 minute.

3. The substrate is baked in an oven for 1 hour at 170 °C. Using a Tencor P-10 surface profiler, we calibrated the resultant thickness of the baked PMMA layers. The first layer was found to be $\approx$ 1000 Å, and the second layer $\approx$ 500 Å.

4. Now the small pattern is ready to be exposed by e-beam. The source of e-beam is a scanning electron microscope (JXA - 840), which is controlled by the e-beam lithography program written by Professor Venkat Chandrasekhar. The exposure by e-beam depends on three parameters; magnification of microscope (Mag), dosage of e-beam exposure (Dos), and beam current (I_{beam}). The typical values of these parameters for submicron scale wires are Mag $\sim$ ×2000, Dos $\sim$ 300 μC/cm^2, and $I_{beam} \sim$ 5 pA.

5. After writing small patterns, the exposed PMMA is removed by a developer. The developer is a mixture of methyl isobutyl ketone (MIBK) and 2-propanol with a volume ratio of 1 : 3. The developing time is 45 seconds at 20 °C.

We illustrate these e-beam lithography steps in Fig. 4.1. The steps for metal deposition and liftoff will be discussed in following sections.

4.1.4 Metal deposition

The third step in Fig. 4.1 is metal deposition. Au (99.999 %) is the primary material in this study, but other materials such as Ag, Al, Ge have been evaporated for other studies using the same evaporator (Edwards 306). The chamber of the evaporator has been kept free of magnetic materials to prevent inadvertent introduction of magnetic impurities during metal deposition. The base pressure of the evaporator is normally $\sim 3 \times 10^{-7}$ Torr after 5 - 6 hours of pumping.

The actual metal deposition process includes a dry etch step. This cleaning step is to remove the residual PMMA in developed areas, and was found necessary for submicron wire fabrication. The detailed process is as follows.

1. The chamber is evacuated until pressure reaches less than 5×10^{-7} Torr.

2. Purified Ar gas is introduced to a pressure of 40×10^{-3} Torr in the chamber, and a dc voltage of 1 kV is applied between two plates. Samples are attached on one of the plates. The distance between the two plates is $\sim$ 2 inches. Ar

ions bombard and remove the residue of the PMMA resist in exposed areas. An appropriate time for the dc plasma glow discharge is $\sim$ 30 seconds.

3. The chamber is re-evacuated to get the pressure down to $\sim$ 5 $\times 10^{-7}$ Torr again.

After cleaning by the dc plasma glow discharge, metal depositions are done by using a thermal boat inside the chamber. Evaporation parameters, *i.e.* the thickness of film and the deposition rate are monitored by a Leybold XTM/2 Deposition Monitor. The typical film deposition rate ranges from 1 to 10 Å/sec. The higher the deposition rate, the larger the grain size in films, and the longer the mean free path and phase coherence length obtained.

4.1.5 Liftoff

A metal film covers the entire substrate after the metal deposition process. Unwanted parts of the film are removed by a procedure which is called liftoff. By removing the PMMA, we also remove the unwanted metal film which is on top of the PMMA. This can be done easily by soaking the substrate in acetone since PMMA dissolves in acetone easily at room temperature. We normally immerse the substrate in acetone for 2 hours. When taking out the substrate after 2 hours, we flush the substrate with acetone to remove fragments of unwanted metal film. Then we immediately flush the substrate with methanol, and blow it dry.

	1st implantation		*2nd implantation*		*3rd implantation*	
concentration	*energy*	*dosage*	*energy*	*dosage*	*energy*	*dosage*
at%	keV	$10^{13}/cm^2$	keV	$10^{14}/cm^2$	keV	$10^{14}/cm^2$
0.2	20	4.5	60	1.2	90	3.8
0.3	20	6.2	75	6.5		
0.4	20	9.0	60	1.8	90	8.1

Table 4.1: Ion implantation energies and dosages for 0.2, 0.3, and 0.4 at% AuFe spin glasses.

4.1.6 AuFe alloy fabrication

Ion implantation

After Au samples are fabricated, ^{56}Fe ions are implanted in the Au film at energies and dosages calculated to give the desired impurity concentrations. Thanks to Professor H. Pattyn at *Instituut voor Kern- en Stralingsfysica, Katholieke Universiteit Leuven, Belgium*, the ion implantation facilities in Leuven have been used to make AuFe alloys with Fe concentrations ranging from 0.1 to 0.4 at%. The advantages of the ion implantation method are that the Fe concentration is not only easily varied, but is also uniform in its spatial distribution. The implantation energies and dosages for 0.2, 0.3, and 0.4 at% AuFe spin glasses are given in Table 4.1. The multiple implantations at 2 or 3 different energies were employed for a more uniform impurity distribution over the film thickness.

Flash evaporation

Some of the AuFe samples in this study were made by the flash evaporation method [126, 128]. The author did not participate in the flash evaporations, but is indebted to Geert Neuttiens, a colleague in *Katholieke Universiteit Leuven, Belgium* for the samples.

For samples presented by flash evaporation, the magnetic impurity concentrations are determined by the concentrations of mother alloys. A series of small droplets of the mother alloy is dropped on top of a hot thermal boat, and is evaporated at a very fast rate. By this way a more uniform concentration can be obtained, otherwise constituents of the mother alloys with different melting points may segregate during evaporation, resulting in a non uniform impurity distribution in the films.

AuFe 0.1, 0.28 and 0.85 at% samples were made by this method, and investigated with regard to size dependence in the spin glass resistivity, $\rho(T)$.

4.2 Transport measurements at low temperature

4.2.1 Cool-down in helium cryostats

Since spin glass freezing in our AuFe alloys typically occurs below $\sim$10 K, we need to cool down our samples to liquid helium temperatures $\sim$ 4.2 K. The most convenient cooling is done in helium cryostats. We used three different types of cryostats depending on the temperature range; a helium-4 cryostat, a helium-3

cryostat, and a ^{3}He-^{4}He dilution refrigerator. The helium-4 cryostat, which was made by the author, can reach $T \sim 1.2$ K under continuous operation. The helium-3 cryostat made by Janis Corporation can reach as low as $T \sim 0.26$ K, but is not a continuous system. The ^{3}He-^{4}He dilution refrigerator, an Oxford 300 Kelvinox is the major work horse in our group, reaching a base temperature of $\sim$ 25 mK without a booster pump.

The wiring from room temperature to the base temperature block in the cryostat was done by using superconducting wires made of NbTi in a CuNi matrix. A π section filter was installed on each data line to prevent rf noise from being transmitted to the samples. Samples are mounted on a cold finger which is directly attached to the base temperature block in each cryostat.

Samples are mounted in such a way that the magnetic field is applied perpendicular to the metal film or substrate surface. The magnetic field is produced by a superconducting magnet made of NbTi alloy wires. There are two magnets, which can go up to 6 and 12 Tesla respectively.

4.2.2 Temperature readout, temperature stabilization, magnet control, data acquisition program, and wire bonding

Temperature readout

In cryogenics one of the most essential and basic things is thermometry. Among many thermometry methods [109], we employed resistance thermometry because of

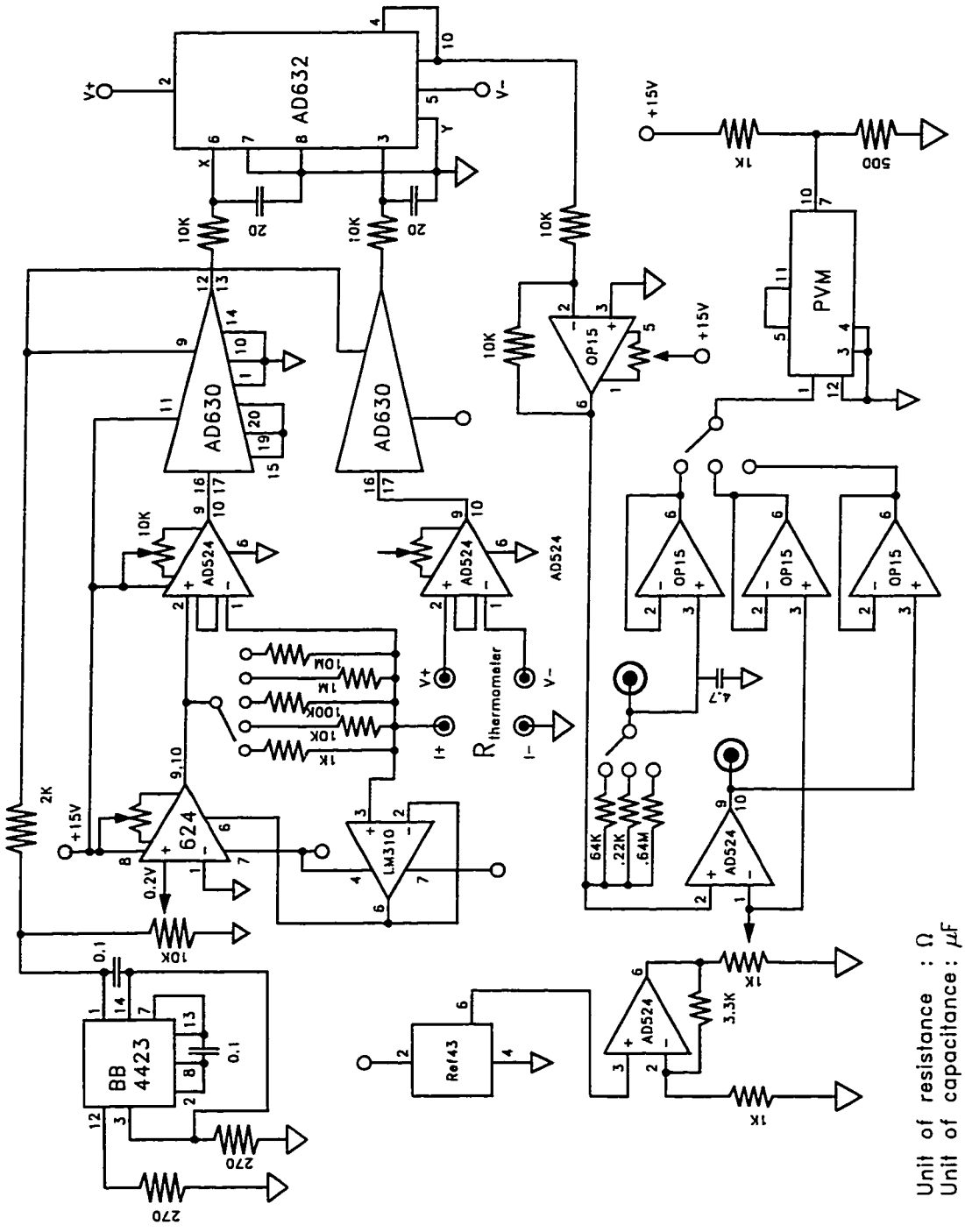

Figure 4.2: Circuit diagram of the thermometer bridge.

its convenience in installation as well as readout. Two types of resistors were used; a germanium resistor and a RuO_2 resistor. Both show insulating behavior at low temperature with the resistance increasing as the temperature is lowered. Although the resistors are easy to mount and measure, problems are always prevalent with regard to thermal contact and self heating by the measuring current. Care is needed to avoid such problems.

To make certain of a good thermal contact, we install the resistors as follows. We make a copper block (oxygen free copper) and drill a hole in it. The resistor is placed inside the hole. After placing the resistor, the space around thermometer is filled with silicon heat sink compound (Dow Corning 340). Once the installation of the resistor is completed, the copper block is screwed into the mixing chamber of the dilution refrigerator.

In the helium-4 cryostat and the helium-3 cryostat, a cold finger made of oxygen free copper is used to hold the sample socket. A hole is directly made in the cold finger and the resistor is placed inside the hole. The extra room in the hole is filled with silicon heat sink compound (Dow Corning 340), as described above.

Once the thermometers are installed properly in the cryostat, the next task is reading the thermometer. For accurate measurements without any self-heating problems, a low excitation thermometer bridge has been designed and made by the author. The detailed circuit design of the thermometer bridge is shown in Fig. 4.2. The bridge is composed of a high output impedance current source, two lock-in

amplifier chips (AD630), a voltage divider (AD632), and an error signal generator (AD524). The excitation current through the thermometer is changed depending on the range of the thermometer resistance. The excitation current for a reading of 1 kΩ resistor is typically 20 nA.

Temperature stabilization

Temperature stabilization is especially essential in $dV/dI(I)$ measurements. Simple temperature controllers were built in our laboratory, and were found to control the desired temperature to within 0.1%. Figure 4.3 shows a schematic of the PID temperature controller we have used in experiments [35].

The temperature controller consists of three parts; proportional (P), integral (I), differential (D) control unit. When the error signal from the thermometer bridge is fed into the input of the temperature controller, the output signal is generated by a summation of the PID components. The appropriate parameters for P, I, and D are found normally by trial and error, and are sensitive to the temperature range. Sometimes we want to scan the temperature rather than measure at a constant temperature. In such case we use Keithley 230 programmable voltage source, which is directly connected to the heater in the cryostat. A computer controls the Keithley 230 to ramp output voltage, and consequently the input power to the heater ramps up or down.

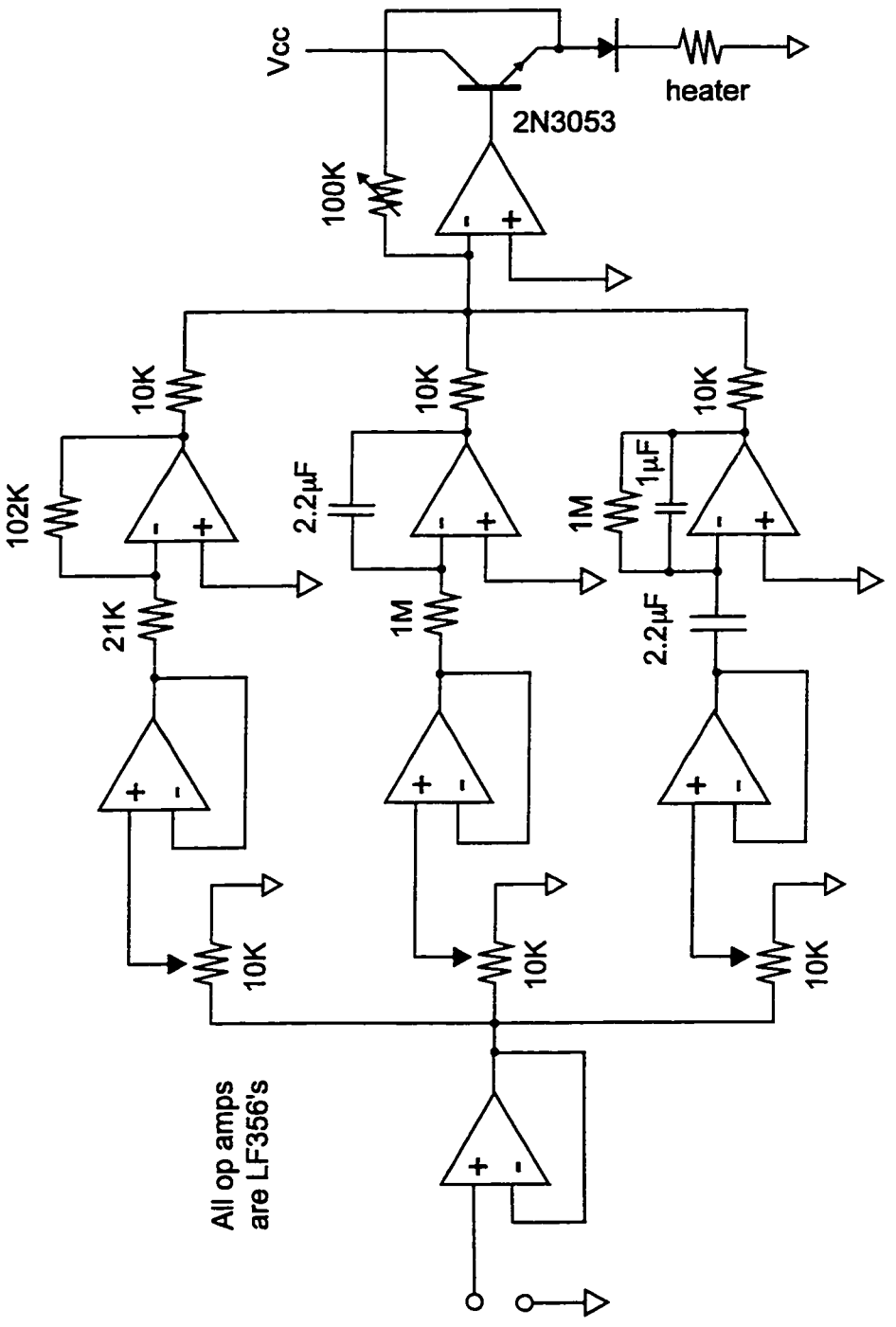

Figure 4.3: Schematic of the PID temperature controller. From Ref. [35].

Magnet control

We use two superconducting magnets. One is used with the helium-4 and helium-3 cryostats and reaches a field of 6 Tesla. The other is used with the dilution refrigerator and reaches a field of 12 Tesla. The current for the magnets is provided by a power supply (HP6260B, KEPCO BOP 20-20M, KEPCO BOP 100-1M, or LakeShore Model 622). The magnitude of the magnetic field is estimated by reading the magnet current which is proportional to magnetic field.

Data acquisition program

The original data acquisition program was written in Basic by Prof. Chandrasekhar. The author participated in the translation of the original program into Pascal, and refined the program to operate more conveniently. The program runs under the DOS operating system on an IBM PC.

Wire bonding

Samples are glued to sample headers by using silver paint. After the samples are mounted on the headers, electrical connections between the copper pins in the heater and electrodes in the samples are made by a wire bonder. A wire bonder is very dependable machine when electrical connections are made in mesoscopic samples. The wire bonder used in our laboratory is a Kulicke and Soffa Model 4123 wedge bonder. We used 0.001″ diameter Al-Si wires (Si 1%) in the wedge bonder.

4.2.3 Measurement of low temperature samples

Four-probe ac resistance bridge

The circuit diagram of a four probe ac resistance bridge is shown in Fig. 4.4. This bridge is a simplified version of the Adler-Jackson bridge [2], and has been constructed by the author. The original version of the design is found in the Ph.D. Thesis of Prof. Chandrasekhar [35]. The bridge contains a 1 MΩ resistor in each arm to make a passive current source. The ac drive generated from the internal oscillator of a lock-in amplifier (PAR 124) is fed into the input of the bridge. The ac probe excitation is applied through an isolation transformer (Triad G-31), which prevents any dc offset current from transferring to the sample. All the components of the bridge are in a single aluminum box which is electrically grounded.

The balance resistor, a GenRad 1432-W Decade Resistor, is located at the mirror site against sample resistor so that it nulls out the common mode signal. Since high frequencies tend to give rise to large phase shifts which are picked up from the inductance of the signal lines, we chose a rather low frequency ranging from 11 to 300 Hz depending on the sample resistance. With this low frequency, this simple bridge works with great reliability and sensitivity.

The ac excitation method has the advantage of preventing dc drift during the measurement, which may cause problems especially when the sample signal is smaller than the drift. However, the ac response of a sample should be exactly phased to measure the exact magnitude of the response. The bridge in Fig. 4.4 has

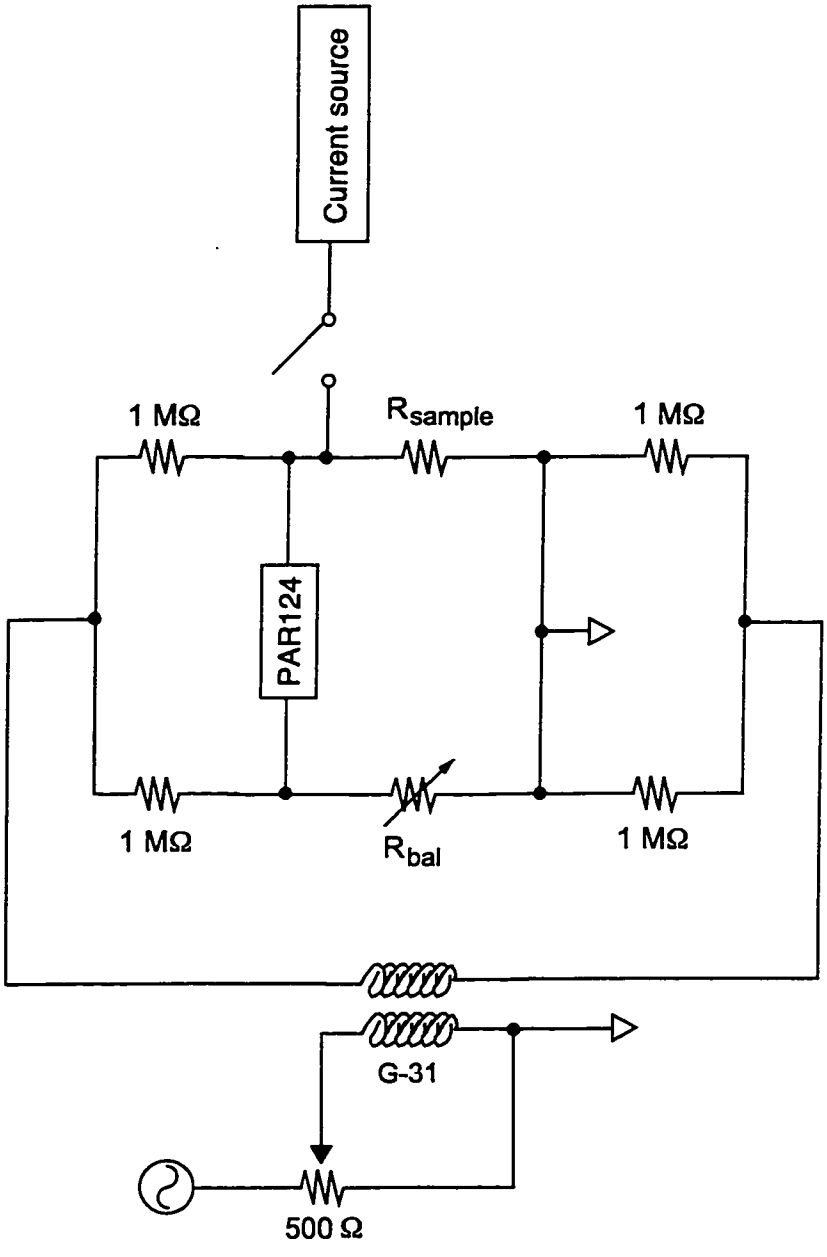

Figure 4.4: Schematic of the four probe resistance bridge. Just by adding a dc bias current source to $I+$ terminal, the measurement configuration for $dV/dI(I)$ is completed.

a great advantage in its ease of exact phasing. With this bridge, phasing is simply accomplished by ensuring that the out-of-phase component does not change when the balance resistance R_{bal} is changed.

Finally let us consider how the differential resistance ($dV/dI(I)$) measurements are set up. With the bridge in Fig. 4.4, the measurement configuration of $dV/dI(I)$ is really straightforward. It is done by just adding a dc bias current source to the $I+$ terminal. Sweeping the dc bias current is achieved using a function generator (HP3325A, or DS345). We normally sweep the dc bias current as high as $\pm 100\mu$A at a sweep rate of 0.1 mHz. The current source for the dc bias current will be discussed in following section.

Current source, instrumentation amplifier, voltage summer

We made three general purpose circuit components as parts of a utility circuit box. The components are a current source, an instrumentation amplifier, and a voltage summer. The utility box has been found to be extremely convenient for low temperature transport measurements. Figure 4.5 shows the schematic of the home-made utility circuit box.

The current source has a very high output impedance ($Z_{output} \approx 1 \times 10^{+13}\Omega$), and is a nearly perfect current source even with sample source impedances on the order of $\sim$ 10 kΩ. We used this bipolar current source to sweep the dc bias current I for the $dV/dI(I)$ measurements.

The instrumentation amplifier, AD624, is used to monitor I in $dV/dI(I)$ mea-

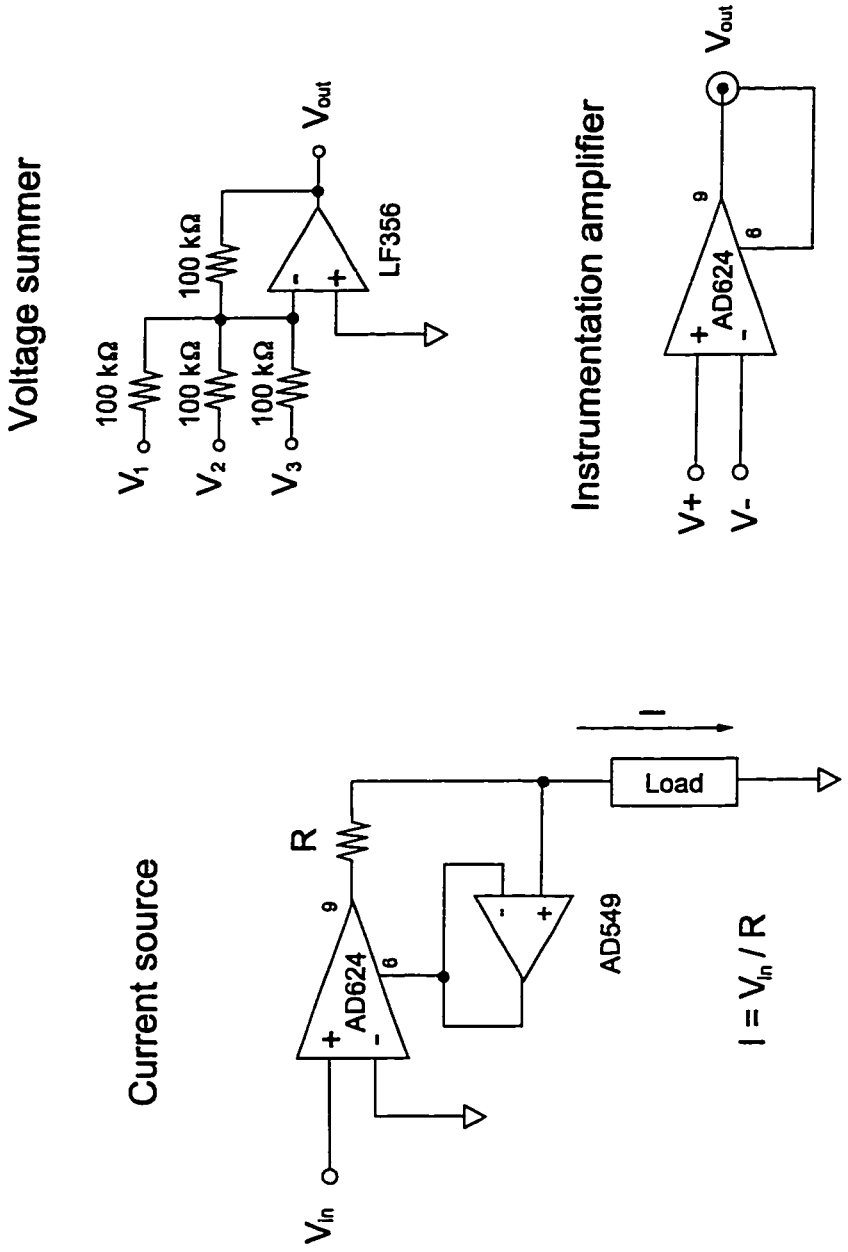

Figure 4.5: Schematic of the home-made utility circuit box. The utility circuit box consists of three components; Current source, Instrumentation amplifier, and Voltage summer.

surements. The advantage of the AD624 amplifier includes low offset voltage, low noise, and precision gain. Therefore it is very useful when the dc bias current through the sample is read out. The voltage summer has not been used in this study.

4.3 Sample characterization

4.3.1 Sample dimension

The thickness of the films in this study range from 200 $\sim$ 400 Å, nad are comparable to the mean free path ℓ, but are much smaller than the thermal length L_T. To read the film thickness, we use a film deposition monitor (Leybold XTM/2). The deposition monitor has been calibrated by a control film, the thickness of which was determined by a Tencor P-10 surface profiler. Other dimensions such as the length and width are determined by using a scanning electron micrograpе.

4.3.2 Other physical parameters

For metallic wires in the Drude model, the elastic mean free path ℓ is obtained from the resistivity (see Eq. 3.17). The AuFe samples in this study typically have $\rho_\mu \approx$ 3.1 - 4.6 $\mu\Omega$cm, and hence $\ell \approx$ 180 - 270 Å.

Since the dimensions of the samples are normally larger than ℓ, the samples are assumed to be in the diffusive limit. The diffusion constant D is obtained from

ℓ using the equation:

$$D = \frac{1}{3} v_F \ell \tag{4.1}$$

where v_F is the Fermi velocity of the conduction electrons in the host metal. Typically for our AuFe samples, we found $D \approx 85$ - 125 cm^2/sec. We also found that D increases as film thickness is increased. The thermal length L_T is obtained from the value of D, and $L_T \approx 0.25$ - 0.31 μm/$\sqrt{T}$ for our AuFe spin glass samples. The sheet resistance $R_\square$ is another useful parameter which describes the quality of films. $R_\square$ is defined by $R_\square \equiv R \times (W/L)$, where R represents the resistance of a sample, W the width, and L the length. $R_\square$ at $T = 4.2$ K is $\sim 1\ \Omega$, *i.e.*, the metal films are nominally clean. Uhe quality of the metal film is also checked by the fact that $k_F \ell \gg 1$. We estimate $k_F \ell$ ($\approx 220 - 320$), which is much larger than 1.

The electron phase coherence length L_φ is rather unimportant in our AuFe alloy since L_φ is greatly suppressed by electron-spin scattering. Furthermore, we were unable to measure L_φ by weak localization measurements.

Chapter 5

EXPERIMENTAL RESULTS: SIZE DEPENDENCE IN THE AUFE SPIN GLASS RESISTIVITY

5.1 A broad resistivity maximum

The electrical resistivity in dilute magnetic impurity alloys shows a logarithmic increase as the temperature T is lowered, the so-called Kondo effect [85]. The Kondo effect is caused by the interactions of conduction electrons with isolated magnetic impurities. The correlations between magnetic impurities are small so that they do not give rise to spin-spin interactions even at low temperature. If the concentration of magnetic impurities is gradually increased, the impurities start to interact with each other, and they are no longer isolated. The system is then called a 'spin glass'. Even in concentrated magnetic impurity alloys, when the thermal energy is larger than the interimpurity interaction, the moments can rotate freely and give rise to an increasing resistivity as temperature is lowered from the Kondo effect [90]. However, if T is lowered further, the thermal energy cannot overcome the interimpurity interactions and the moments start to freeze out. The freezing of moments modifies electron-spin scattering, and the resistivity ρ decreases

as T is lowered. In consequence, the resistivity shows a broad maximum at a finite temperature T_m. T_m scales with the impurity concentration; the higher the concentration, the higher T_m [57].

Although we have measured $\rho(T)$ of many AuFe wires with various concentrations ranging from 0.1 - 1.0 at%, we will focus only a few of them, which provide us with the most essential information. Fig. 5.1 shows $\rho(T)$ for a 0.2 at% AuFe wire, a 0.4 at% AuFe wire and a pure Au wire. $\rho(T)$ of the AuFe wires shows a broad resistivity maximum at a finite temperature T_m. While T_m for the 0.2 at% AuFe wire is $\sim$ 1.7 K, T_m for the 0.4 at% AuFe wire is $\sim$ 3.5 K. As expected, T_m increases with increasing Fe concentration. Both AuFe wires show a minimum in $\rho(T)$ at a temperature $T_{min} \approx$ 10.5 K. In contrast, $\rho(T)$ of the pure Au wire decreases monotonically as T is lowered, finally saturating below $\sim$ 4.0 K.

There is an important thing to note in Fig. 5.1. For the Kondo samples the resistivity slope scales as the magnetic impurity concentration; the more concentrated the alloys, the more negative the slope (see Section 3.1.1). However, the resistivity slope in Fig. 5.1 does not reflect this behavior. In the temperature range between T_m and T_{min} the resistivity slope of a 0.2 atAuFe wire. This is attributed to the fact that spin-spin interactions still exist above T_m, and hence the resistivity slope is not simply governed by the Kondo effect [89]. Spin-spin interactions, which are stronger in more concentrated magnetic alloys, mask the manifestation of the Kondo resistivity. Therefore the resistivity slope of the 0.2 atnegative than that of

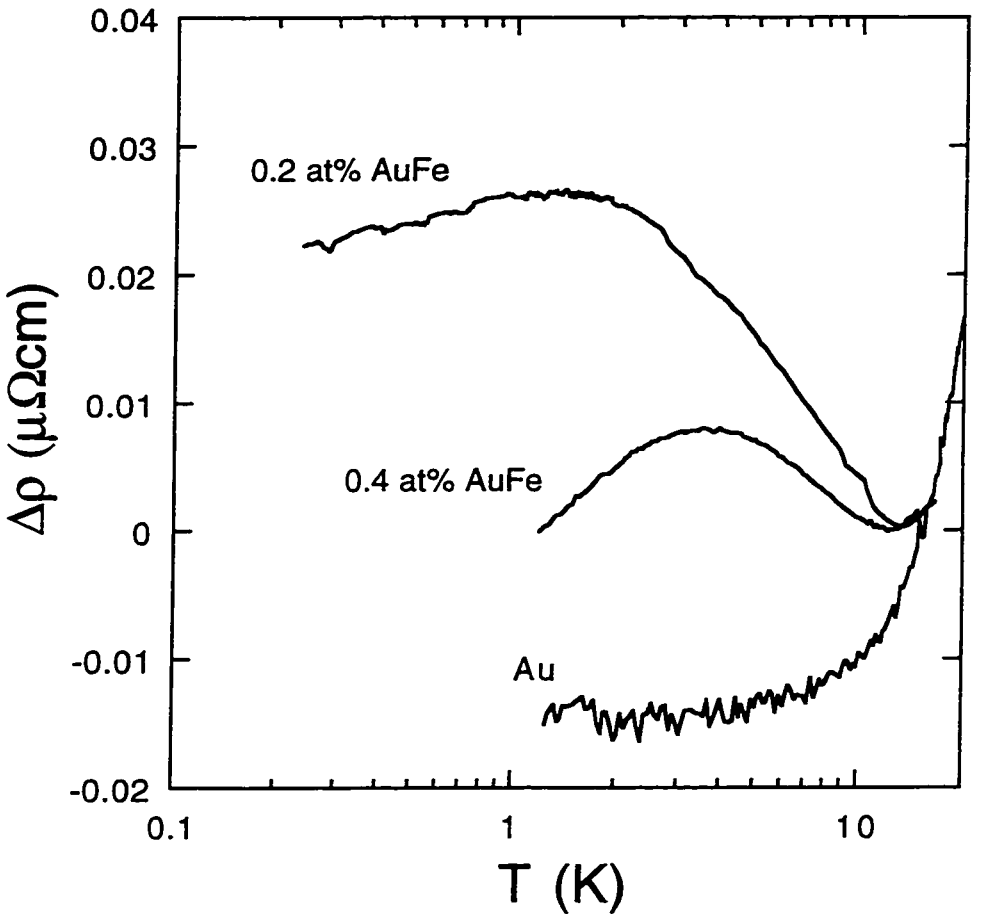

Figure 5.1: $\Delta\rho(T)$ ($\equiv \rho(T) - \rho(10.5K)$) of spin glass AuFe wires. The dimensions of the AuFe wires are $W = 135$ nm, $L = 1.8$ μm for 0.2 at%, and $W = 85$ nm, $L = 3.5$ μm for 0.4 at% alloy. $\Delta\rho(T)$ of a pure Au aire is also plotted for comparison, and its dimensions are $W = 115$ nm, $L = 1.84$ μm. The film thickness is identical for all three wires, $t = 330$ Å. At $T = 10.5$ K, $\rho = 4.5$ $\mu\Omega$cm for the 0.2 at% AuFe wire, 4.6 $\mu\Omega$cm for the 0.4 at% AuFe wire, and 6.0 $\mu\Omega$cm for the Au wire.

the 0.4 at% AuFe spin wire.

5.2 $\rho(T)$ of spin glasses in a finite magnetic field

The properties of spin glasses are highly sensitive to a magnetic field H. For example, a small magnetic field smears out the sharp ac-susceptibility, destroying the phenomenon of the spin glass phase transition [33]. $\rho(T)$ is also affected by H. As the magnetic field H is increased, the amplitude of the broad maximum in $\rho(T)$ decreases, and T_m shifts toward higher temperatures (see Fig. 5.2). $\rho(T)$ in Fig. 5.2 is zero field cooled (ZFC), which means that the sample had been cooled first in zero magnetic field, and then the data were taken at a finite field as T is increased. There is another way of cooling, which is the so-called field cooling (FC) technique. The sample is cooled with a finite field and then the data are taken as T is increased. However, we found no differences between ZFC and FC measurements of $\rho(T)$. This observation contrasts with the fact that the magnetization of CuMn spin glass as a function of temperature shows a clear difference between FC and ZFC [102]. Magnetic moments in FC samples align their directions during spin glass freezing, causing an enhancement of the magnetization. However, $\rho(T)$ is not sensitive to the relative orientations of spins and is consequently not sensitive to differences between ZFC and FC.

Previously we argued that T_m originates from the interplay of the Kondo effect and the spin-spin correlation strength Δ_c. In a magnetic field the spin flip scattering

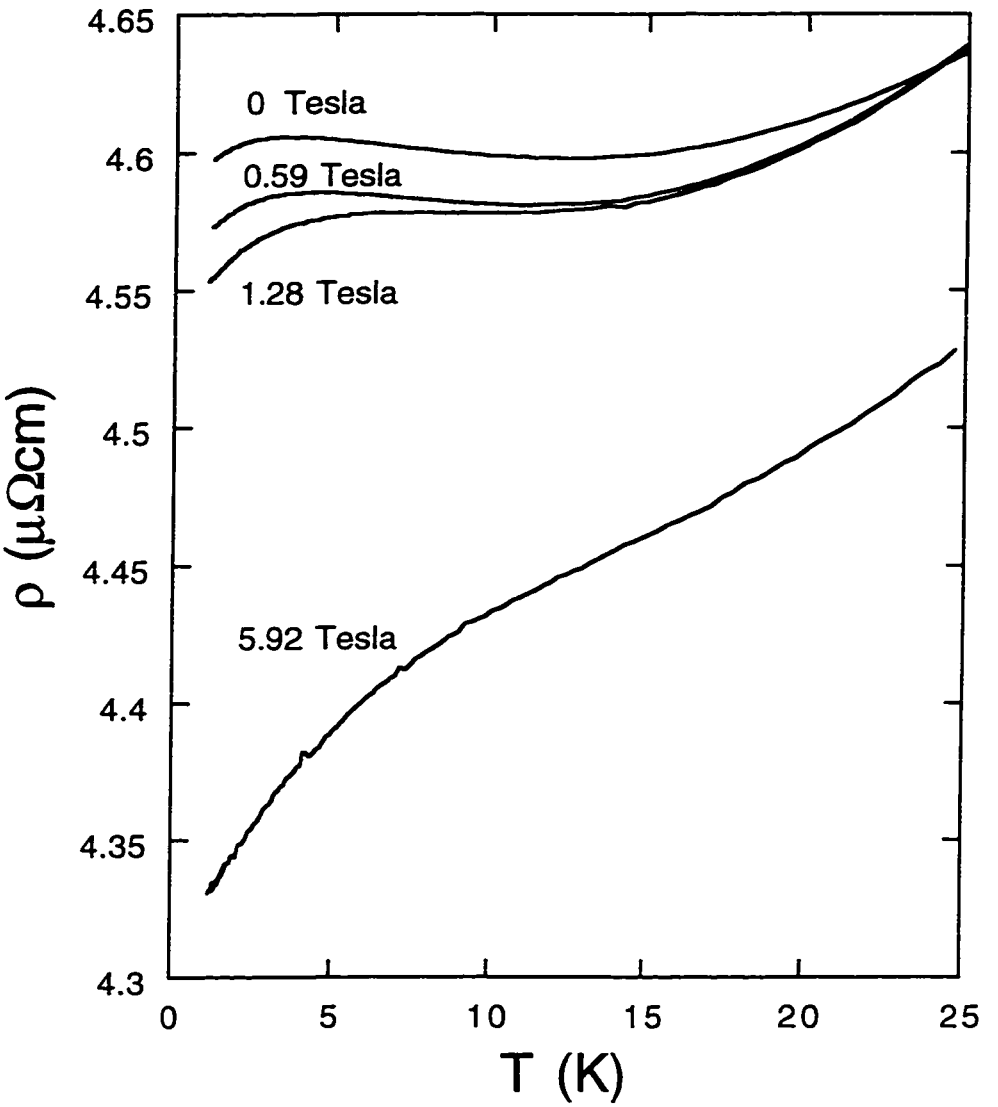

Figure 5.2: $\rho(T)$ of a 0.4 at% AuFe wire at various magnetic fields. The dimensions of the AuFe wire are $W = 85$ nm, $L = 3.5$ μm, $t = 330$ Å.

which gives rise to the Kondo effect is greatly suppressed, and hence the temperature T_m shifts toward higher temperatures and the amplitude of the resistivity maximum decreases as shown in Fig. 5.2. For $H = 0$ to 1.28 Tesla, we still see a maximum in $\rho(T)$. At a magnetic field H = 5.92 Tesla, T_m exceeds the temperature where electron-phonon scattering is dominant. Therefore, a broad maximum is not apparent in $\rho(T)$.

5.3 Absence of a size effect in the spin glass resistivity

Many experiments have focused on the size scale of the Kondo screening cloud, and have investigated $\rho(T)$ of dilute magnetic alloys as the dimensions of the alloys are changed (see Chapter 2). However, the disagreement among the experimental observations in Kondo alloys has not been resolved as yet. Recently, researchers have focused on more concentrated magnetic alloys, *i.e.*, spin glasses [87]. Finite size effects in the spin glass freezing temperature T_f in CuMn spin glass films have already been investigated [67, 79, 80], and the general consensus is that T_f decreases as the film thickness is reduced. It was also found that T_f remains finite even at a 1 monolayer [67]. However, a size effect in T_f does not necessarily guarantee a size effect of the Kondo screening cloud. The screening cloud is a spin correlation of the conduction electrons around a local magnetic impurity. NMR might be a better method to probe the electron spin correlation. However, the NMR spectrum for dilute alloys of CuFe shows no drastic change in the spatial polarization associated

with the Kondo condensation, rasing the question of whether the Kondo screening cloud really exists [28].

In this section we report detailed measurements of the resistivity $\rho(T)$ of thin AuFe spin glass wires for various widths ranging from 140 nm to 300 μm. The thin film samples were prepared by flash evaporation. The comparisons are made only among the samples which were fabricated in the same evaporation. Therefore, the samples are nominally identical except for their linewidths. AuFe mother alloys with two different Fe concentrations, 0.28 and 0.85 at%, have been used to make two sets of samples.

Fig. 5.3(a) shows $\Delta\rho$ (T) = ρ(T) - ρ(10 K) for a series of 0.28 at% AuFe wire of different width. The resistivity of these samples at 4.2 K is 9.24 $\mu\Omega$cm, and the corresponding mean free path $\ell \approx$ 89.3 Å. The 300 μm wide wire shows a broad maximum around 2 K. Taking ρ(T) of the 300 μm wide wire as a reference, $\rho(T)$ of the other quasi 1-dimensional wires show systematic deviations in their temperature dependence. As the width is reduced, the amplitude of $\Delta\rho(T)$ increases and T_m shifts toward lower temperatures.

Fig. 5.4(a) shows $\Delta\rho$ (T) = ρ(T) - ρ(10 K) for 0.85 at% AuFe wires. The resistivity at 4.2 K is 11.94 $\mu\Omega$cm, and the corresponding $\ell \approx$ 70.4 Å. The broad maximum is located at higher temperatures in this high concentration alloy, and buried under the contribution from electron-phonon scattering. However, we still see the size dependence in $\rho(T)$ at temperatures below $\sim$ 4 K. As similar as 0.28

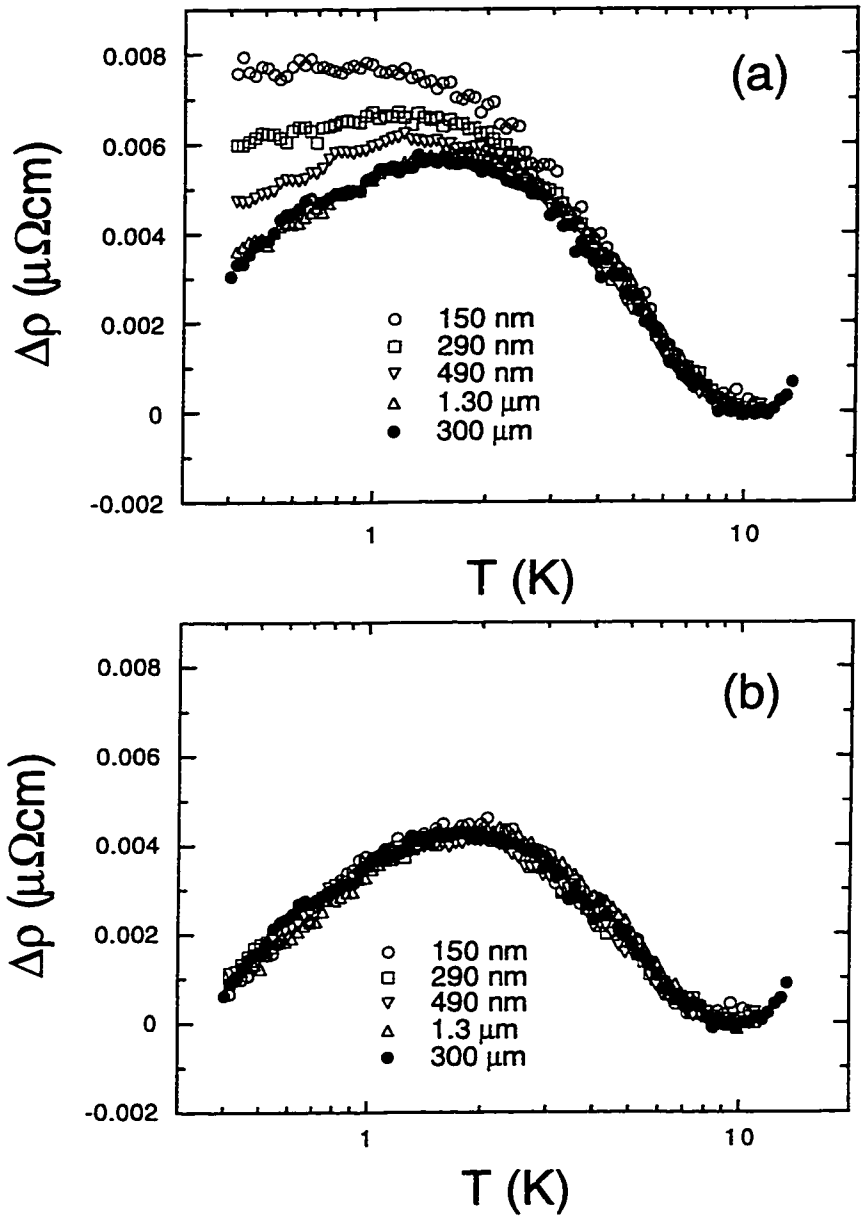

Figure 5.3: $\Delta\rho(T)$ of 0.28 at% AuFe wires. (a) $\rho(T)-\rho(10K)$ of the 0.28 at% AuFe wires with film thickness $t = 220$ Å and different linewidths. (b)$\rho(T) - \rho(10K)$ after subtracting the electron-electron interaction contribution. From Ref. [104].

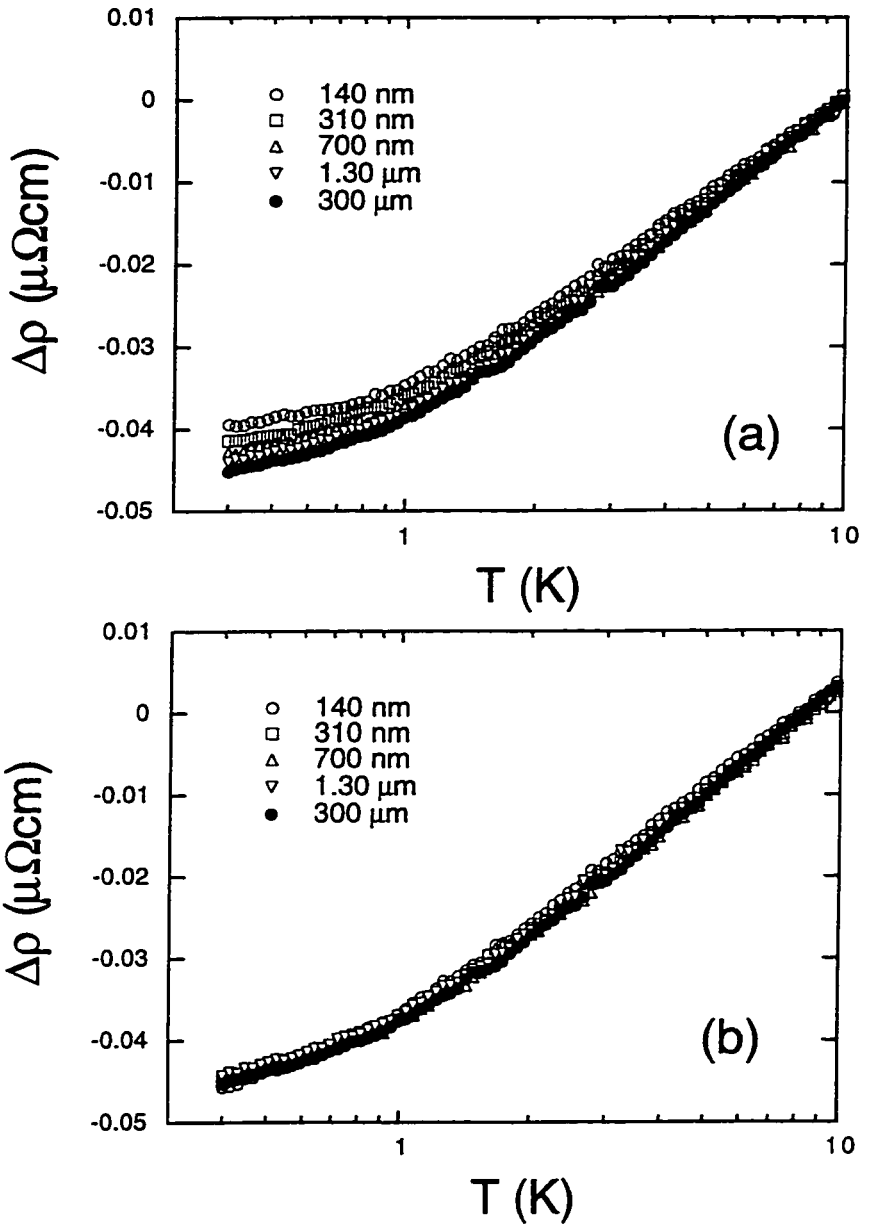

Figure 5.4: $\Delta\rho(T)$ of 0.85 at% AuFe wires. (a) $\rho(T)-\rho(10K)$ of the 0.85 at% AuFe wires with film thickness $t = 250$ Å and different linewidths. (b)$\rho(T) - \rho(10K)$ after subtracting the electron-electron interaction contribution. From Ref. [104].

at% AuFe wires, $\rho(T)$ of the 0.85 at% AuFe wires show a systematic reduction of spin glass freezing as the width becomes narrower. The amplitude of $\Delta\rho(T)$ increases as the width is reduced.

Both Figs. 5.3(a) and 5.4(b) clearly show a size dependence below the spin glass freezing temperature. However, before concluding the existence of a size effect in the spin glass freezing, one has to note that the low temperature resistivity is also influenced by other factors, for example, the electron-electron interaction or weak localization contribution. However, weak localization would be greatly suppressed by the scattering with magnetic impurities. In contrast, the electron-electron interaction contribution still exists even with magnetic impurities. The contribution of electron-electron interactions to the resistivity ($\delta\rho_{ee}$) depends on the size of the samples as shown in Section 3.4.2. For electron-electron interactions, the thermal length L_T ($= (\hbar D/k_B T)^{1/2}$) is the appropriate length scale which determines the dimensionality of $\delta\rho_{ee}$. L_T for the samples in Fig. 5.3 is typically $\sim$ 180 nm/$\sqrt{T}$, and L_T for the samples in Fig. 5.4 $\sim$ 160 nm/$\sqrt{T}$. L_T for both sets of the samples is comparable to the width of the samples so that the dimensionality of samples are between 1 and 2. The functional form of $\delta\rho_{ee}$(T) for these quasi 1-dimensional samples has been given in Eq. 3.33. We first determine the prefactor α in Eq. 3.33 by making $\Delta\rho - \delta\rho_{ee}$ of the narrowest wire falls on top of $\Delta\rho - \delta\rho_{ee}$ of the widest wire. The value for both sets of samples is $\alpha \approx 1.5$, which is consistent with the value of α for Kondo samples [34]. Keeping the value of α same, $\delta\rho_{ee}$(T)

is subtracted from $\Delta\rho$(T) for the other samples with different widths. After the subtraction, the resulting $\Delta\rho(T)$ coincide regardless of their width differences as shown in Fig. 5.3(b) and Fig. 5.4(b). Therefore, *no size dependence of the spin glass resistivity is found down to a length scale of* $\sim$ *150 nm.*

The absence of size dependence of the spin glass resistivity is consistent with the previous work by Chandrasekhar *et al.* [34], which has been discussed in Section 2.1.3. They measured $\rho(T)$ of AuFe wires but for the very dilute Fe impurity regime, *i.e,* the Kondo regime. When the EE interaction contribution ($\delta\rho_{ee}$) was subtracted, the resulting $\rho(T) - \delta\rho_{ee}$ was identical regardless of the linewidths, which ranged from 38 nm to 105 μm.

However, our result is against the conclusion which was drawn in the paper by Lane *et al.* [87]. They measured $\rho(T)$ of CuCr spin glass films and found the reduction of the interimpurity interaction Δ_c as the film thickness was reduced down to 150 Å.

Why does such a disagreement occur? One may notice that the difference between the experiments is the method of varying the dimensions of the samples. While one varies the linewidth of samples, the other varies the thickness of samples. The surface-to-volume ratio is not changed appreciably by varying the linewidth, but the surface-to-volume ratio is changed considerably when the film thickness is varied. This factor, along with the spin-orbit induced magnetic anisotropy model by Ujsaghy *et al.* [123] gives a suggestive explanation for the disagreement in the

experiments. To check this idea, one needs to measure the resistivity of very narrow wires of which the linewidth is comparable to the film thickness. If the model is valid, one will see a cross-over of the size effect when the linewidth becomes smaller than the film thickness.

Chapter 6

EXPERIMENTAL RESULTS: DIFFERENTIAL RESISTANCE AS A FUNCTION OF DC BIAS CURRENT

Resistance may be measured by two different methods depending on the nature of the probe current. One method utilizes a small dc current, and the other a small ac current. Both measurements eventually give the same number in the limit of zero current. In actual experiments, however, the two methods are not same. While the dc technique is sensitive to drifts which frequently come from the measurement environment, the ac differential technique is almost free of drift and has a high resolution. The dc drift typically originates from thermoelectric voltages, and is thus sensitive to the temperature gradient along signal lines which exist quite often in low temperature measurements. For this reason we employed the ac differential technique to measure the transport properties of samples.

While we discussed dV/dI as a function of T in the previous chapter, we will concentrate on dV/dI as a function of dc bias current I in this chapter. Keeping all other parameters the same including T, we measure dV/dI as I is swept slowly.

The major role of I in a diffusive metal is heating of the electron system, as we discussed in Section 3.5.1. Consequently $dV/dI(I)$ would appearto be ralated to the differential resistance as a function of temperature, $dV/dI(T)$ [88, 137]. However, it turns out that this is not true for $dV/dI(I)$ in AuFe wires. Even in the simplest case where $dV/dI(I)$ of a AuFe wire is symmetric in I, a discrepancy is found in the amplitudes of $dV/dI(I)$ and $R(T)$ which cannot be explained by a simple heating model. When $dV/dI(I)$ contains a non-zero antisymmetric component [50, 103], the interpretation becomes more complicated. Here, we extend the study of $dV/dI(I)$ to heat transport properties, and find something more than $dV/dI(T)$. In the end, we connect the heat transport of $dV/dI(I)$ with thermoelectric effects.

We found $dV/dI(I)$ of AuFe wires shows qualitatively different behavior depending on the widths of the wires. The critical width found in our measurements is $W \approx 150$ nm. Therefore we divide samples into two categories; *the narrow wires* ($W < 150$ nm) and *the wide wires* ($W > 150$ nm). We also found that $dV/dI(I)$ is sensitive to the 4-terminal measurement configuration. To denote different measurement configurations we shall use the notational convention $dV/dI_{ij,kl}$, where i, j represents the current terminals and k, l the voltage terminals.

So far we have denoted the bath temperature simply by T since there is no need to distinguish the electron temperature and the bath temperature. However, electrons are heated up above the bath temperature when a dc current flows through

a sample, giving rise to a temperature difference between the electron system and the bath. To clarify this issue, from now on we shall use T just for the bath temperature and T_e for the temperature of the electron system.

6.1 *Differential resistance $dV/dI(I)$ of pure Au wires*

Figure 6.1(a) shows $dV/dI(I)$ of a Au wire at a bath temperature $T = 1.355$ K. $dV/dI(I)$ shows a quadratic increase with increasing I with some fluctuations at the low bias regime. These fluctuations actually turn out to be very interesting and will be discussed in a moment.

Figure 6.1(b) shows the antisymmetric part (dV/dI_A) of the differential resistance in Fig. 6.1(a), which is extracted numerically. $dV/dI_A(I)$ is basically just flat without any curvature, indicating no appreciable dependence of I. This flat line in $dV/dI_A(I)$ looks uninteresting and dull, but turns out to be very important for checking whether our measurement system gives rise to an artificial asymmetry in $dV/dI(I)$.

Several other measurements on pure Au wires with widths ranging from 80 nm to 1 μm confirm that $dV/dI(I)$ of Au wires is symmetric (see Fig. 6.2(b)) and the measurement system we employed did not generate any artificial effects in $dV/dI(I)$.

Now let us discuss further the fluctuations in $dV/dI(I)$. We found that the fluctuations in the data were not measurement noise but reproducible and the am-

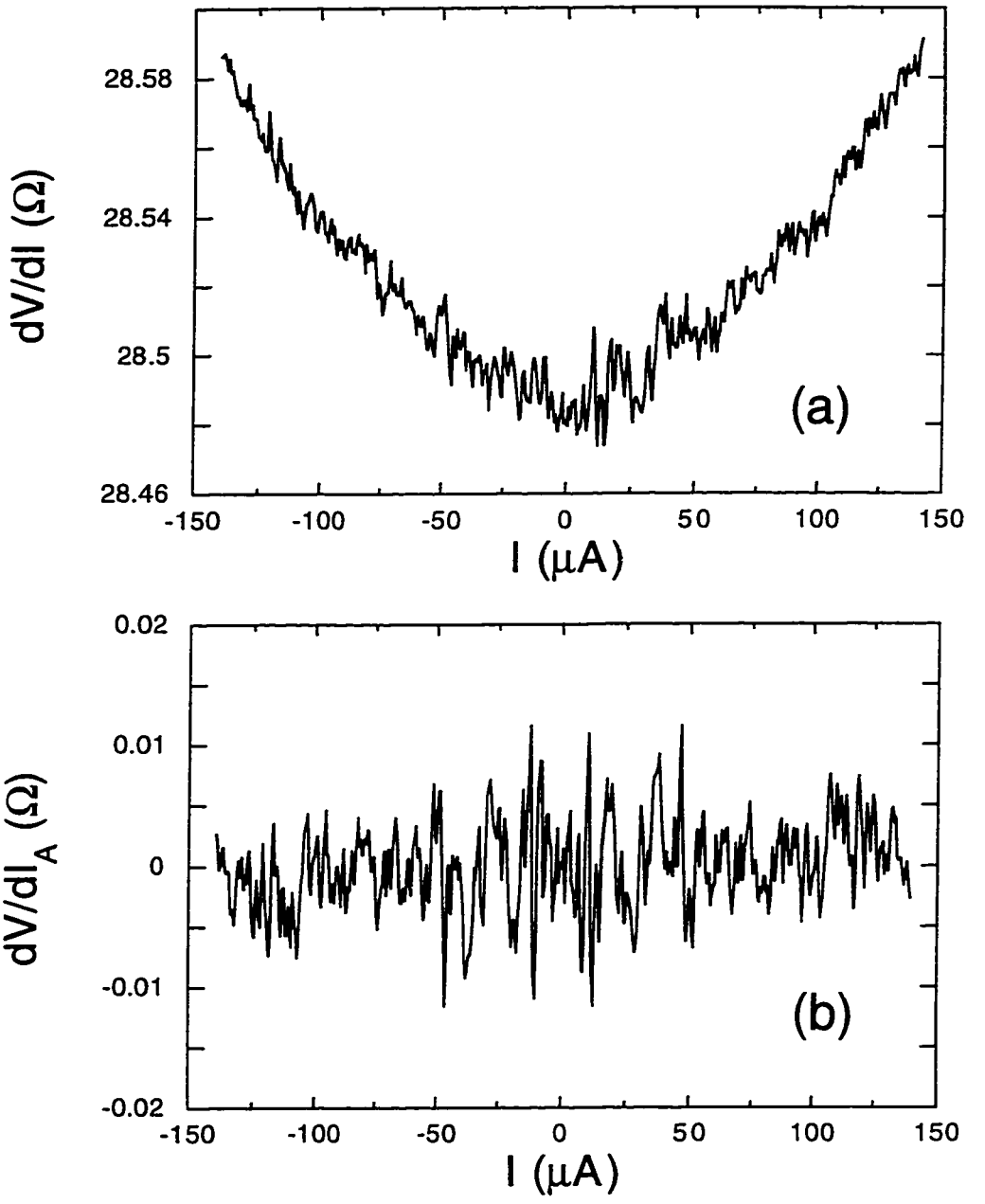

Figure 6.1: dV/dI(I) of a pure Au wire. The Au wire has $W = 117$ nm, $L = 1.83$ μm, and $t = 330$ Å. The measurement was performed at $T = 1.355$ K

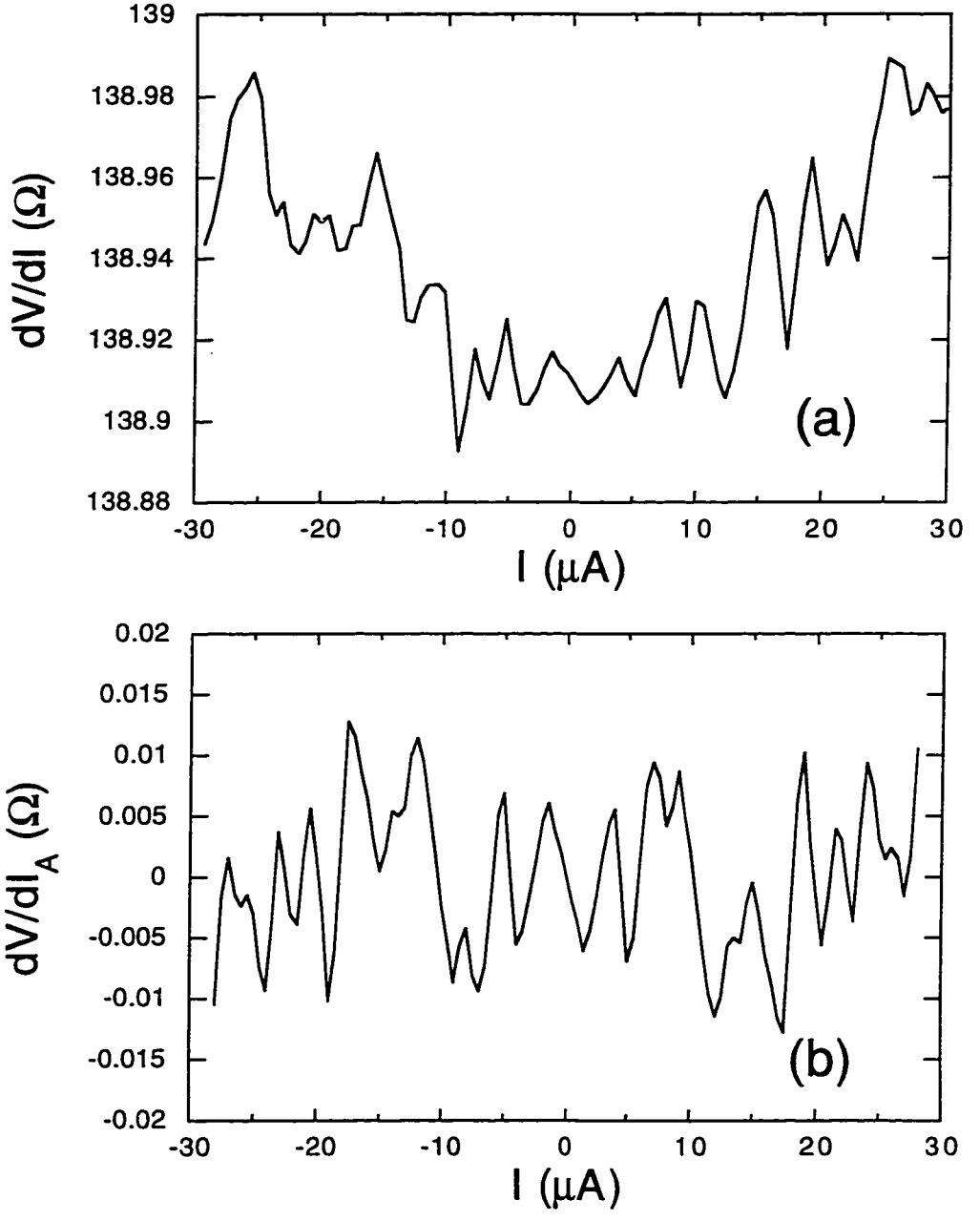

Figure 6.2: Conductance fluctuations in $dV/dI(I)$ of a Au wire. The Au wire has $W = 96$ nm, $L = 7.3$ μm, and $t = 330$ Å. The measurement was performed at $T = 4.43$ K

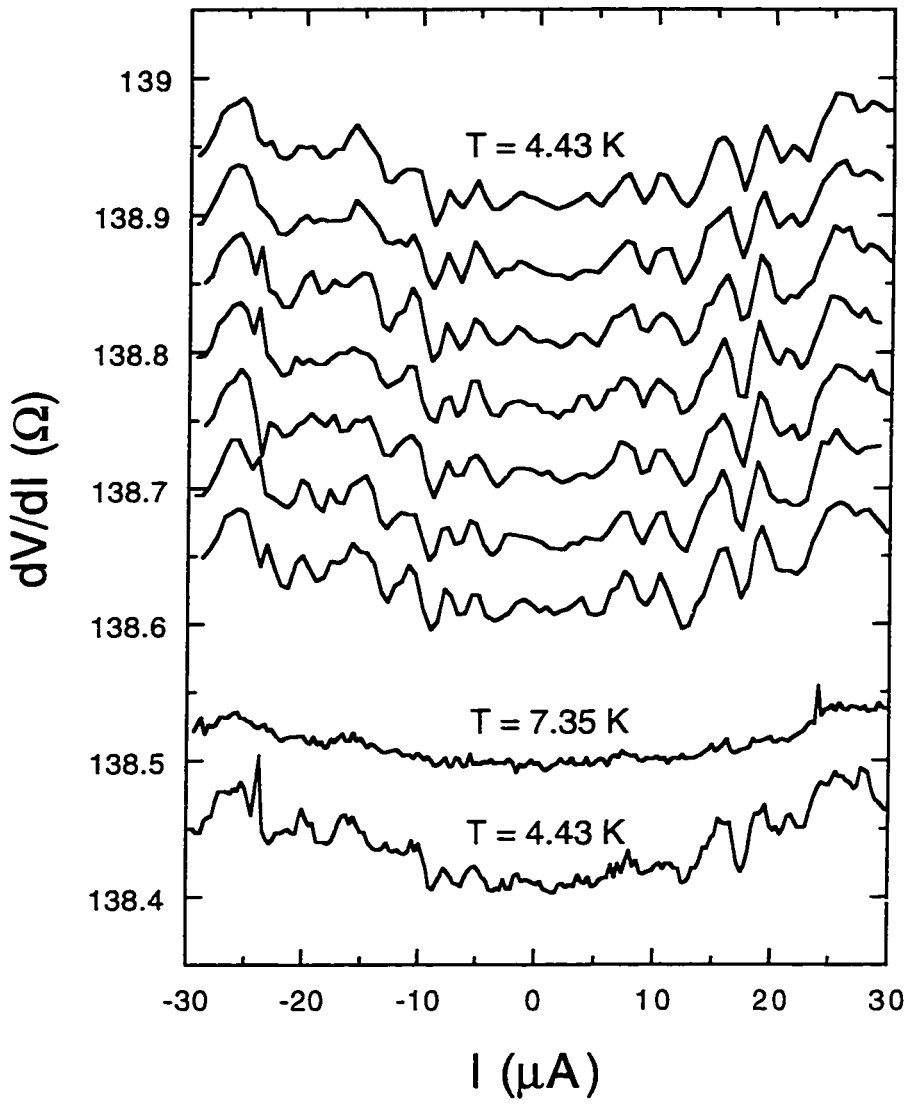

Figure 6.3: Conductance fluctuations in $dV/dI(I)$ before and after warming up. The Au wire has $W = 96$ nm, $L = 7.3$ μm, and $t = 330$ Å. Top seven traces were taken at $T = 4.43$ K one after another, then the sample was heated up to 7.35 K for the next trace. Finally the sample was re-cooled back to $T = 4.43$ K. The curves are shifted for clarity.

plitudes of the fluctuations decrease as T is increased. To check whether the fluctuations are just restricted to one particular Au wire or not, we measured $dV/dI(I)$ of another Au wire. Figure 6.2(a) shows $dV/dI(I)$ of a Au wire with a narrower width (= 96 nm). We found the fluctuations still exist except that the pattern of the fluctuations is different. As pointed out before, the fluctuations in $dV/dI(I)$ of Fig. 6.1 and 6.2 are reproducible as long as samples are kept at the same temperature. A more detailed relationship between the fluctuations and temperature is shown Fig. 6.3. The figure shows nine different traces of the same Au wire as in Fig. 6.2. The top seven traces were taken keeping the substrate temperature fixed at 4.43 K. The seven traces are remarkably similar. As long as the sample is kept at 4.43 K, we found that the shape of the low bias $dV/dI(I)$ did not change even after a week. But one needs to be careful to get reproducible fluctuations with regard to applied bias current I. I should not exceed a certain high bias current, over which the temperature of substrate rises up. We kept I below ~ 300 μA in our samples.

To investigate the effect of temperature, we increased T up to 7.35 K and took a $dV/dI(I)$ trace. The resulting $dV/dI(I)$ shows a great suppression of the fluctuations as shown in Fig. 6.3. Finally we re-cooled the sample back to 4.43 K, and measured $dV/dI(I)$ again. To our surprise, $dV/dI(I)$ then showed a different pattern compared to the one before heating. Warming to a temperature of 7.35 K re-arranged the impurity configurations inside the sample.

Similar fluctuations have already been intensively studied in the 1980's; namely

the Altshuler-Lee-Stone theory of *Conductance Fluctuations* [4, 11, 91, 92]. Conductance fluctuations are found especially in small samples ($L < L_\varphi$), where the conduction electrons retain their phase memories within the sample. The estimate of the amplitude of the conductance fluctuation δG is given by [4, 11, 91, 92]

$$\begin{aligned} \delta G &\equiv \sqrt{[(G - [G]_{av})^2]_{av}} \\ &\approx e^2/h \qquad\qquad \text{at} \quad T = 0\,\mathrm{K} \end{aligned} \tag{6.1}$$

where $[\ ]_{av}$ represents an average over impurity configurations of a sample. Therefore, δG does not scale with sample length [71]. The above estimate for the conductance fluctuation is in good agreement with the experimental data on Au films (*e.g.*, $\sim 0.067e^2/h$ for the Au wire in Fig. 6.3) [131]. However, it fails to describe the data from samples in the ballistic regime [42].

δG becomes smaller at higher temperature, first because L_φ decreases as T is increased, and second, because the effect of thermal averaging increases as T is increased. This explains the observation in Fig. 6.3, but we still need to figure out the implication of $[\ ]_{av}$ in $dV/dI(I)$ measurements.

Since an impurity configuration is fixed at same low temperature, the measurement of $[\ ]_{av}$ could be a difficult task. One may think of heating up a sample to high enough temperature to re-arrange the impurity configuration and then cooling it down again. However, the number of times one has to heat up to get an $[\ ]_{av}$ makes things impossible. There is no way to measure δG like this. Fortunately there is

a way to measure $[\ ]_{av}$ experimentally. According to the ergodic hypothesis [92], averaging over a finite magnetic field range is equivalent to averaging over impurity configurations.

The background of this idea is that the effect of a new impurity configuration can be obtained by randomizing the electron phase with applied magnetic field. In the presence of magnetic field an electron traveling along the path connecting from $\mathbf{r}_0$ to $\mathbf{r}_1$ will get a phase shift of $\Delta\phi = \int_{\mathbf{r}_o}^{\mathbf{r}_1} \mathbf{A} \cdot d\mathbf{r}$, where $\mathbf{A}$ is the vector potential. Therefore the phase shift depends on magnetic field as well as the traveling path of the electron. The magnitude of the critical field to have a new impurity configuration is given by $H_c \sim \Phi_0/L_\varphi^2$ for a 2-dimensional film and $H_c \sim \Phi_0/WL_\varphi$ for 1-dimensional wire of width W. Here, Φ_0 is the normal flux quantum hc/e.

Conductance fluctuations have also been found as a function of other measurement parameters; for example as a function of dc bias current in Sb wires [132] and as a function of the gate voltage in metal oxide semiconductor field effect transistors [75, 76, 94, 114]. This can be simply understood when one extends the 3-dimensional vector potential $\mathbf{A} \cdot d\mathbf{r}$ into the four-vector product $A_\mu(dx)^\mu$, and hence the phase shift $\Delta\varphi$ includes the term of $\int eVdt/\hbar$. Here V is a scalar potential associated with the electric fields in a sample [130]. This agrees with the observation of conductance fluctuations in our $dV/dI(I)$ measurements.

6.2 $dV/dI(I)$ of five probe AuFe wires

6.2.1 $dV/dI(I)$ of wide AuFe wires

$dV/dI(I)$ of spin glass wires at temperatures below the resistance maximum temperature T_m shows a maximum. This maximum resembles the maximum in $\rho(T)$ which originates from the interplay of the Kondo effect and spin glass freezing. Fig. 6.4 shows an example of $dV/dI(I)$ of wide AuFe wires. Fig. 6.4(a) is for a 0.1 at% AuFe wire with $W = 250$ nm, made by using flash the evaporation technique. Fig. 6.4(b) is for a 0.4 at% AuFe wire with $W = 407$ nm made by using ion implantation. $dV/dI(I)$'s of samples from the two different fabrication methods do not show any fundamental differences.

T_m for these samples are 2.5 and 3.5 K respectively, and scale with the impurity concentration. In both cases we find that $dV/dI(I)$ *is completely symmetric in the bias current* I. The symmetric $dV/dI(I)$'s are consistent with a simple electron heating picture [88]. I heats an electron system equivalently regardless of its direction so that the resulting $dV/dI(I)$ is symmetric in I. Such $dV/dI(I)$ curves now should be comparable to $R(T)$ since I basically functions as a heater of the electron system. Fig. 6.5 shows the comparison between $dV/dI(I)$ and $R(T)$ of a 0.1 at% AuFe wire. A simple linear scaling gives a nice match between two curves except for the mismatch in the amplitudes. The amplitude of $dV/dI(I)$ is larger than that of $R(T)$. The enhanced amplitude of $dV/dI(I)$ will be discussed in detail

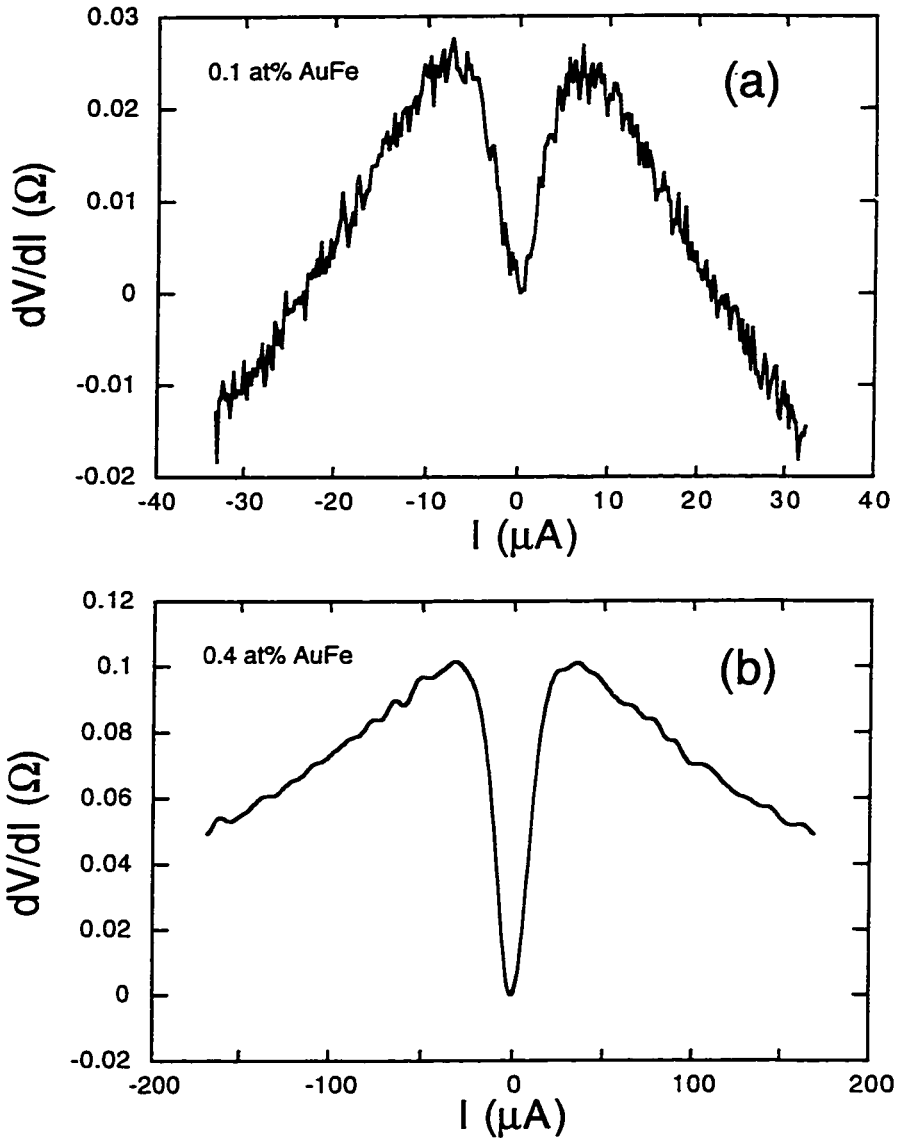

Figure 6.4: $dV/dI(I)$ of wide AuFe wires. (a) $dV/dI(I)$ of a 0.1 at% AuFe wire with $W = 250$ nm, $L = 10.59$ μm, and $t = 225$ Å. The measurement was performed at $T = 1.314$ K, and $dV/dI(0) = 135.1$ Ω. (b) $dV/dI(I)$ of a 0.4 at% AuFe wire with $W = 407$ nm, $L = 11.38$ μm, and $t = 330$ Å. The measurement was performed at $T = 1.235$ K, and $dV/dI(0) = 26.75$ Ω.

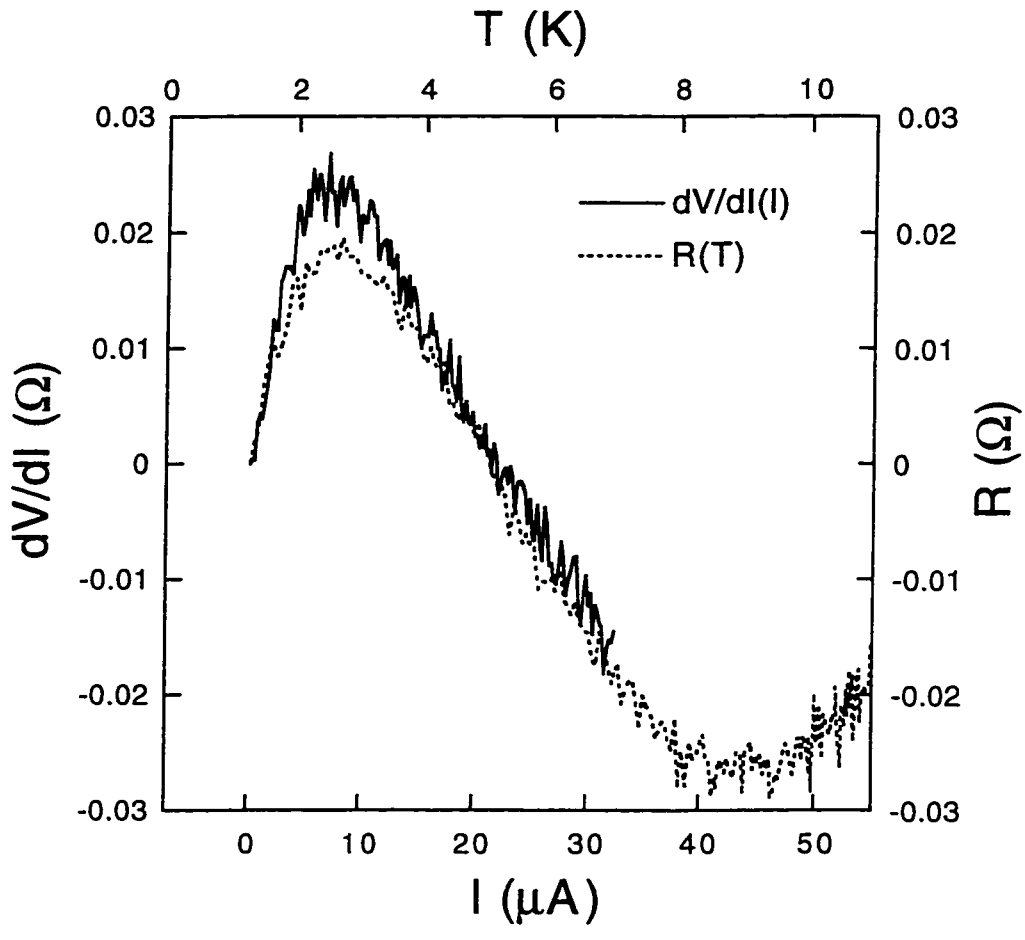

Figure 6.5: $dV/dI(I)$ vs. $R(T)$ of a wide AuFe wire. Solid line: $dV/dI(I)$ of a 0.1 at% AuFe wire with $W = 250$ nm, $L = 10.59$ μm, and $t = 225$ Å. $T = 1.314$ K, and $dV/dI(0) = 135.1$ Ω. Dotted line: $R(T)$ of the same wire.

in Section 6.4.4.

Although Fig. 6.4 does not show the high current bias regime, $dV/dI(I)$ will eventually increase as I is increased, influenced by the phonon contribution which is also found in $\rho(T)$ at high temperature.

6.2.2 $dV/dI(I)$ of narrow AuFe wires

Electron heating is the dominant contribution to the nonlinear behavior of $dV/dI(I)$ of a wide AuFe wire. However, we found that there is another contribution in narrow AuFe wires. Figure 6.6 shows $dV/dI(I)$ of narrow AuFe wires in two different concentrations, 0.2 and 0.4 at%. Both samples were made by ion implantation. The widths of the wires are 85 and 135 nm, respectively. The resistance at 4.2 K of the 0.2 at% sample is 17.7 Ω, the 0.4 at% sample 57.5 Ω. The measurement environment was identical to that for the wide AuFe wires, and the temperature T was fixed below T_m. As is clear in Fig. 6.6(a) *$dV/dI(I)$'s of narrow AuFe wires is asymmetric in I.* The asymmetry is more evident when the antisymmetric part of the differential resistance $dV/dI_A(I)$ is examined. $dV/dI_A(I)$ is obtained numerically from $dV/dI(I)$ and is drawn in Fig. 6.6(b). $dV/dI_A(I)$ shows a clear step-like anomaly near zero dc bias current.

This anomaly is a rather surprising result since $dV/dI_A(I)$ of the narrow Au wire in Fig. 6.1 does not contain any antisymmetric part. The asymmetry must be associated with the presence of magnetic impurities in the sample. To clarify

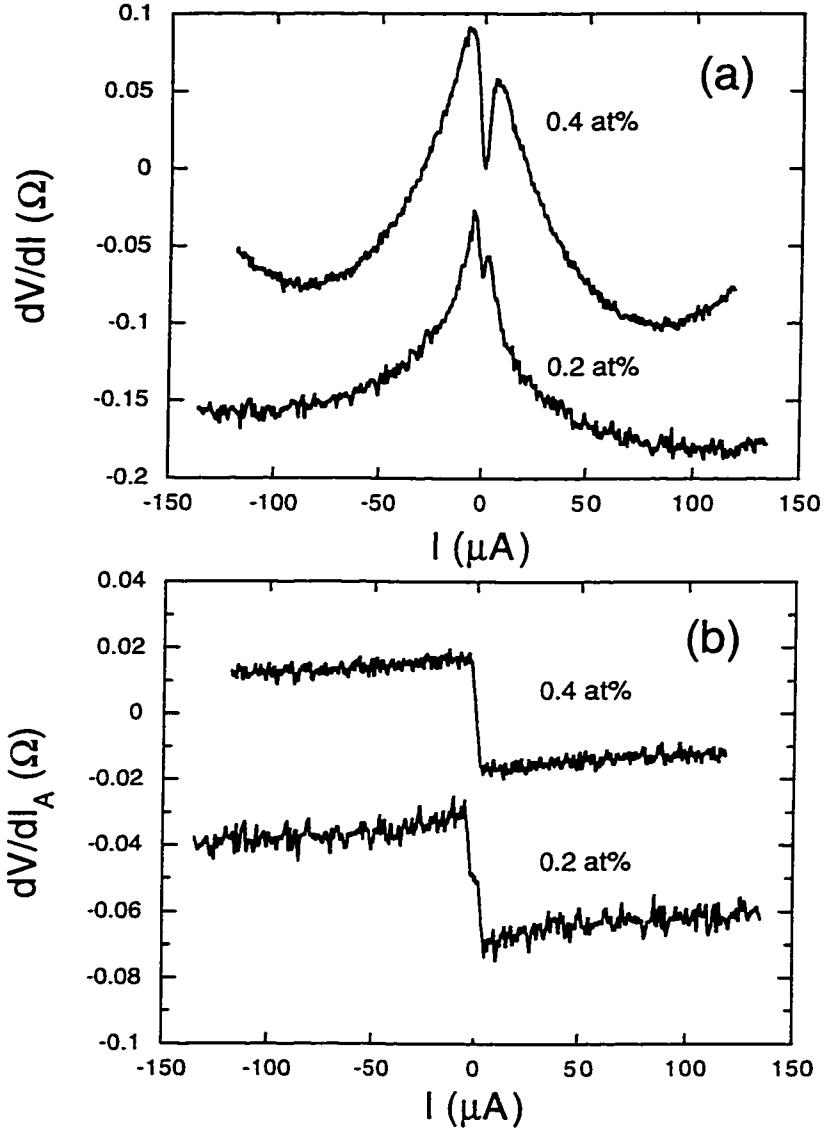

Figure 6.6: $dV/dI(I)$ of narrow AuFe wires. (a) $dV/dI(I)$ of a 0.4 at% AuFe wire with $W = 85$ nm, $L = 3.5$ μm, and $t = 330$ Å. The measurement was performed at $T = 1.705$ K (b) $dV/dI(I)$ of a 0.2 at% AuFe wire with $W = 135$ nm, $L = 1.8$ μm, and $t = 330$ Å. The measurement was performed at $T = 0.051$ K. The plots are shifted for clarity.

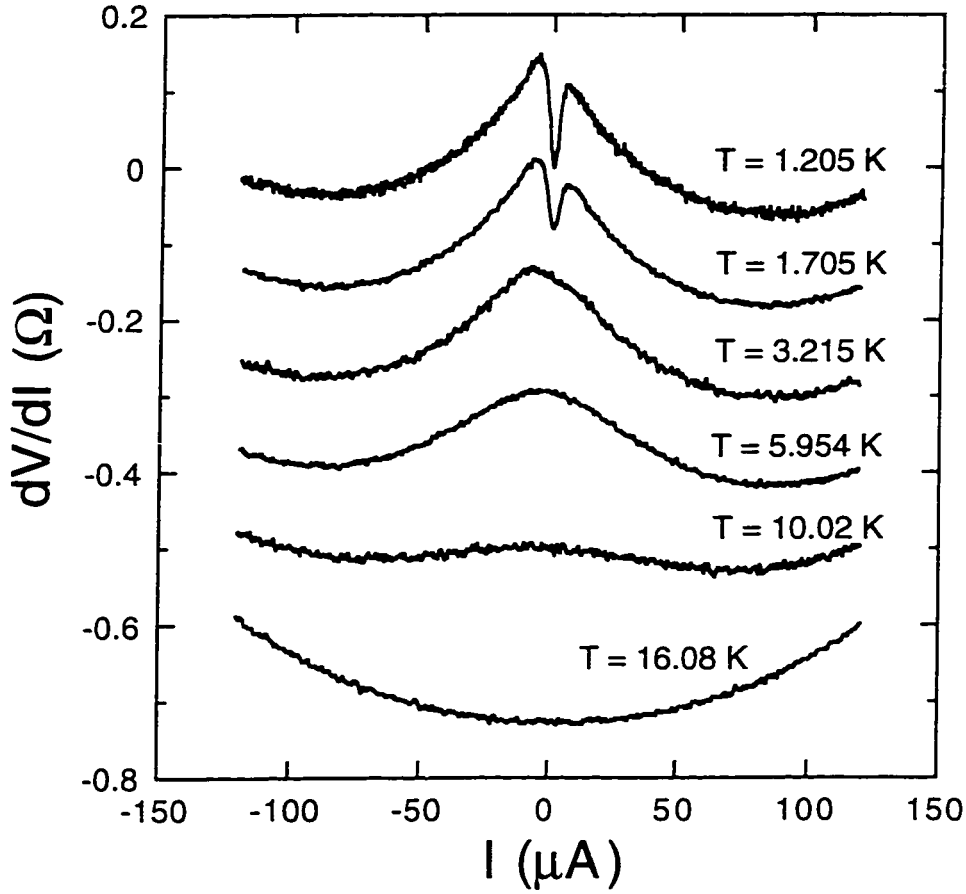

Figure 6.7: $dV/dI(I)$ of a narrow 0.4 at% AuFe wire at various temperatures. The dimension of the wire is $W = 85$ nm, $L = 3.5$ μm, and $t = 330$ Å. Asymmetric $dV/dI(I)$ at low temperature gradually becomes symmetric at higher temperature, and is completely symmetric at $T = 16.08$ K.

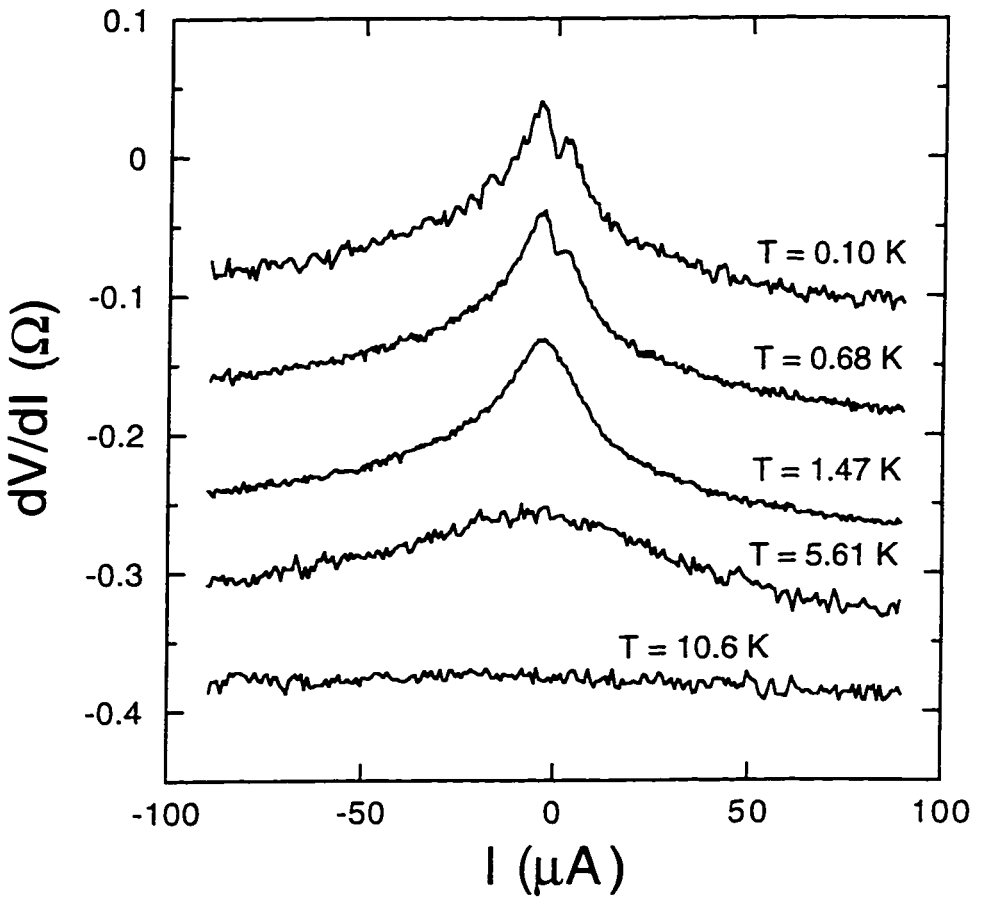

Figure 6.8: $dV/dI(I)$ of a narrow 0.2 at% AuFe wire at various temperatures. The dimension of the wire is $W = 135$ nm, $L = 1.8$ μm, and $t = 330$ Å. The temperature dependence shows behavior similar to a narrow 0.4 at% AuFe wire. The asymmetry in $dV/dI(I)$ at low temperature gradually decreases at higi temperature.

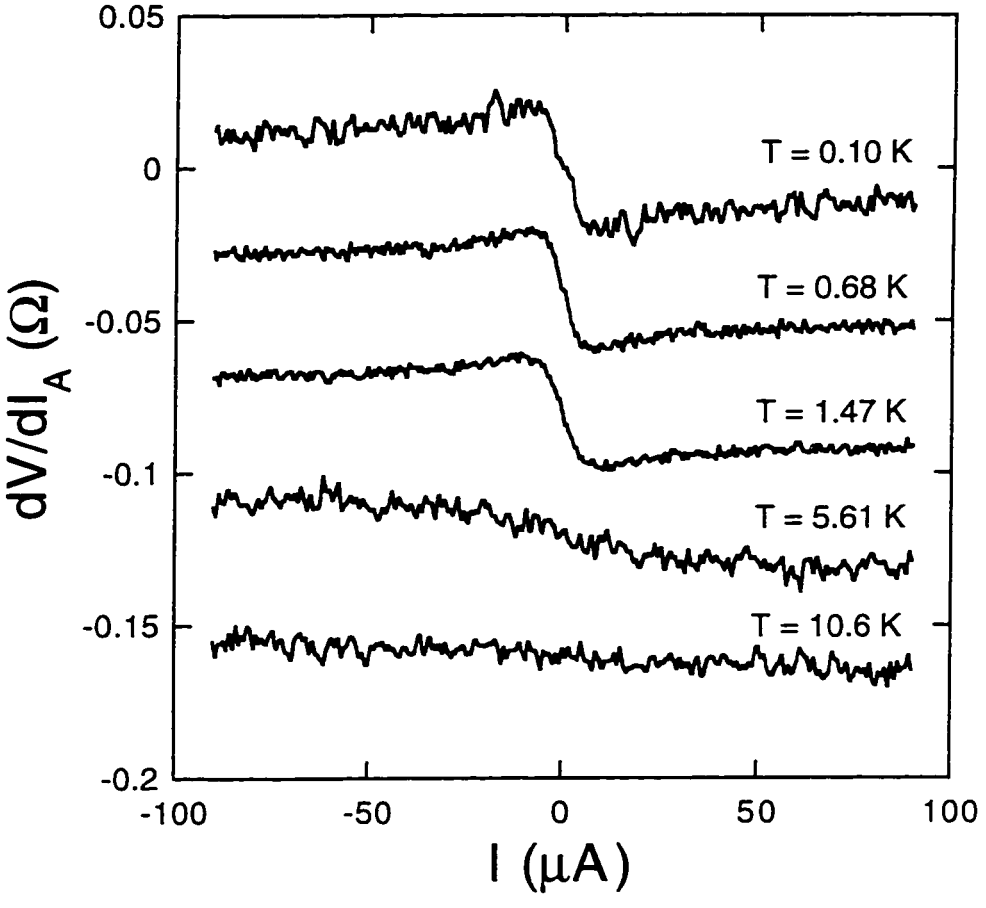

Figure 6.9: $dV/dI_A(I)$ of a narrow 0.2 at% AuFe wire at various temperatures. dV/dI_A is numerically extracted from $dV/dI(I)$ in Fig. 6.8.

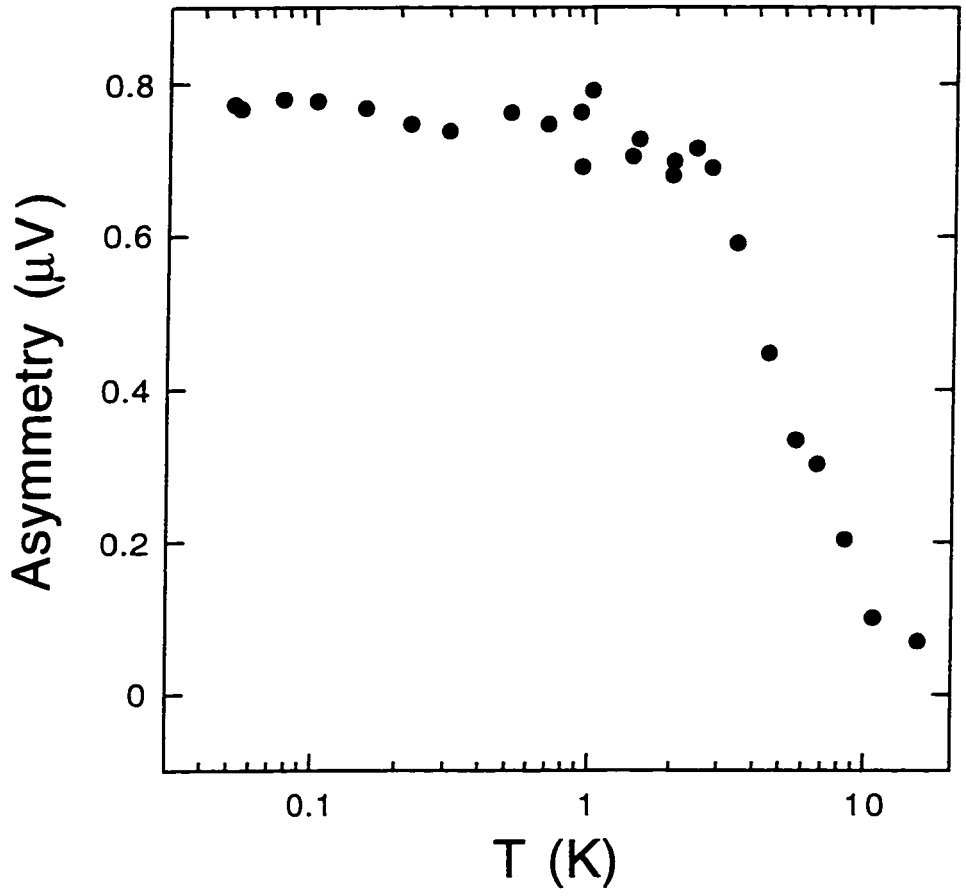

Figure 6.10: Asymmetry of a narrow 0.2 at% AuFe wire as a function of temperature. Asymmetry is defined by the integration of $dV/dI_A(I)$ from $I = 0$ to 30 μA. $dV/dI_A(I)$ is from Fig. 6.9.

the relationship with the magnetic impurities present in the samples, we measured $dV/dI(I)$ of the narrow AuFe wire at various temperatures. Fig. 6.7 shows $dV/dI(I)$ of a narrow 0.4 at% AuFe wire at six different temperatures T. As T is increased above T_m, the maximum in $dV/dI(I)$ disappears, and the asymmetry of $dV/dI(I)$ also disappears gradually, vanishing completely at $T = 16.08$ K.

Similarly, $dV/dI(I)$ of a 0.2 at% AuFe wire with $W = 135$ nm was measured at various fixed temperatures. The temperature dependence of the asymmetric $dV/dI(I)$ resembles that of the narrow 0.4 at% wire. As T is increased, the asymmetry in $dV/dI(I)$ gradually disappears. The asymmetry as a function of bath temperature T can be seen more clearly if the antisymmetric part of $dV/dI(I)$ is examined. The resulting $dV/dI_A(I)$'s at various T's are shown in Fig. 6.9. The step-like $dV/dI_A(I)$ at low temperatures gradually disappears at high temperatures. To obtain quantitative estimates of the asymmetry, we integrate the antisymmetric part from 0 to 30 μA. This quantitative result of the integration is named as *asymmetry*. The resulting asymmetry is shown in Fig. 6.10. The asymmetry grows by more than an order of magnitude as T is decreased from 10 K down to 2.5 K, and saturates below $T_{sat} \approx 2.5$ K. The saturation temperature, T_{sat}, is comparable to T_m of this sample (see Fig. 5.1). However, the saturation temperature, T_{sat}, obtained by this analysis is dependent on the range of integration, presumably due to electron heating at high current bias. Reducing the integration range lowers the saturation temperature by about 10 - 20 %, but the increased scatter in the

data also increases the uncertainty in determining the saturation temperature by approximately the same amount. Consequently, we have chosen the integration range small enough to minimize the effect of heating, but large enough to reduce the scatter in the data to an acceptable level.

6.2.3 Effect of magnetic field on the asymmetry in $dV/dI(I)$

Spin glass freezing is sensitive to magnetic field. From the theoretical point of view, a magnetic field destroys the spin glass phase transition [82], which is consistent with the experimental observation that a sharp cusp-like ac susceptibility at T_c becomes flattened out in a finite field [81]. We have already examined the field dependence of $\rho(T)$ in Section 5.2. The resistivity maximum moves up to higher temperatures and the amplitude of the maximum decreases as the magnetic field H is increased.

A magnetic field affects $dV/dI(I)$ of spin glass wires as well. The maximum in $dV/dI(I)$ shifts towards higher bias currents as H is increased (see Fig. 6.11). At the highest applied magnetic field of 5.92 Tesla, the maximum is buried completely under the differential resistance of the high bias current regime. If one looks only at Fig. 6.11, the asymmetry in $dV/dI(I)$ appears to be reduced with H, vanishing at $H = 5.92$ Tesla. However, it turns out that this is just an illusion. $dV/dI_A(I)$ still shows a clear zero bias anomaly at high fields, as is shown in Fig. 6.12. Actually, the magnitude of the peak in $dV/dI_A(I)$ increases as H is increased.

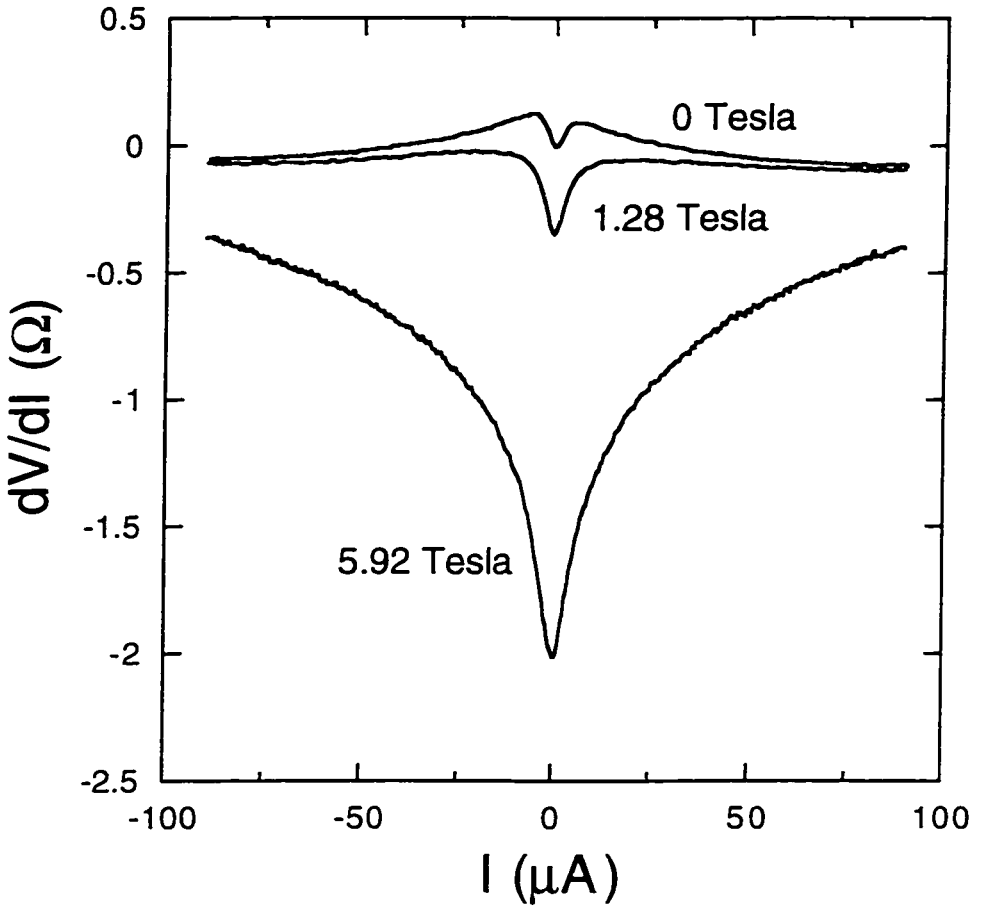

Figure 6.11: $dV/dI(I)$ of a narrow 0.4 at% AuFe AuFe wire at various magnetic fields. The dimension of the sample is $W = 85$ nm, $L = 3.5$ μm, and $t = 330$ Å. The bath temperature is fixed at $T = 1.28$ K for all three fields. The maximum moves to higher bias currents as the magnetic field is increased.

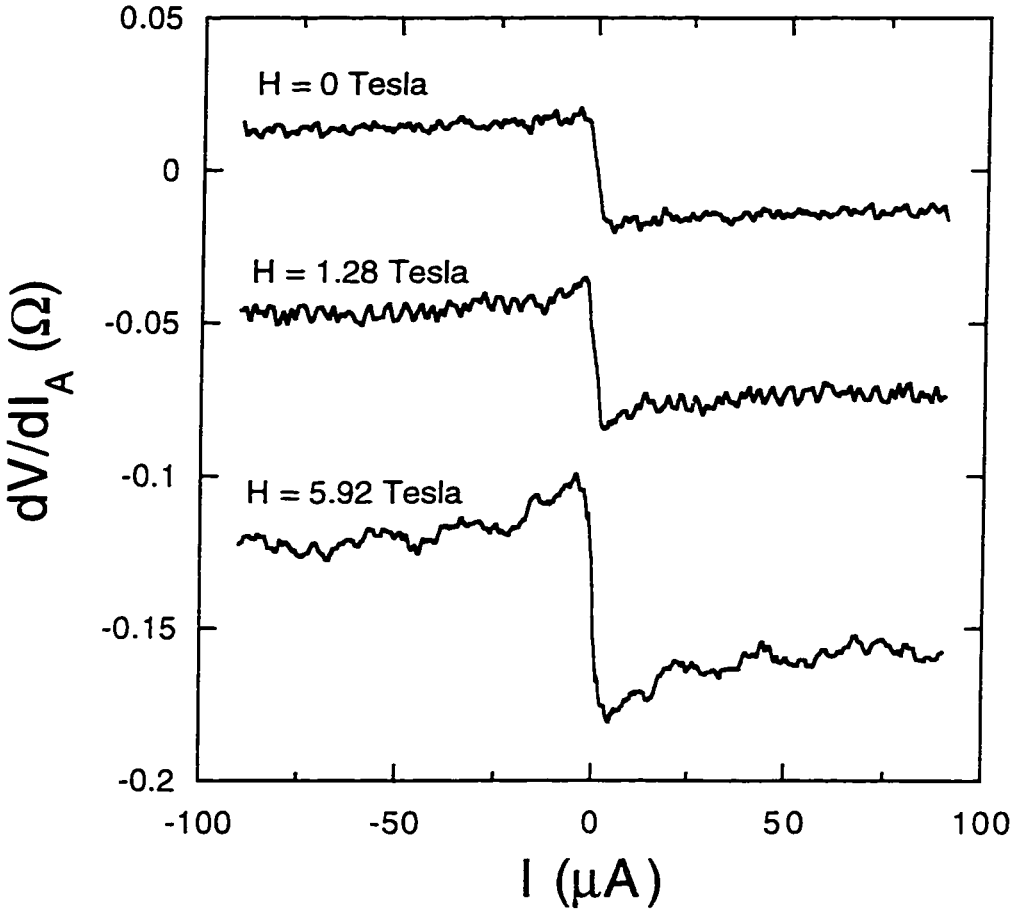

Figure 6.12: $dV/dI_A(I)$ of a narrow 0.4 at% AuFe wire at various magnetic fields. $dV/dI_A(I)$ was extracted from $dV/dI(I)$ in Fig. 6.11.

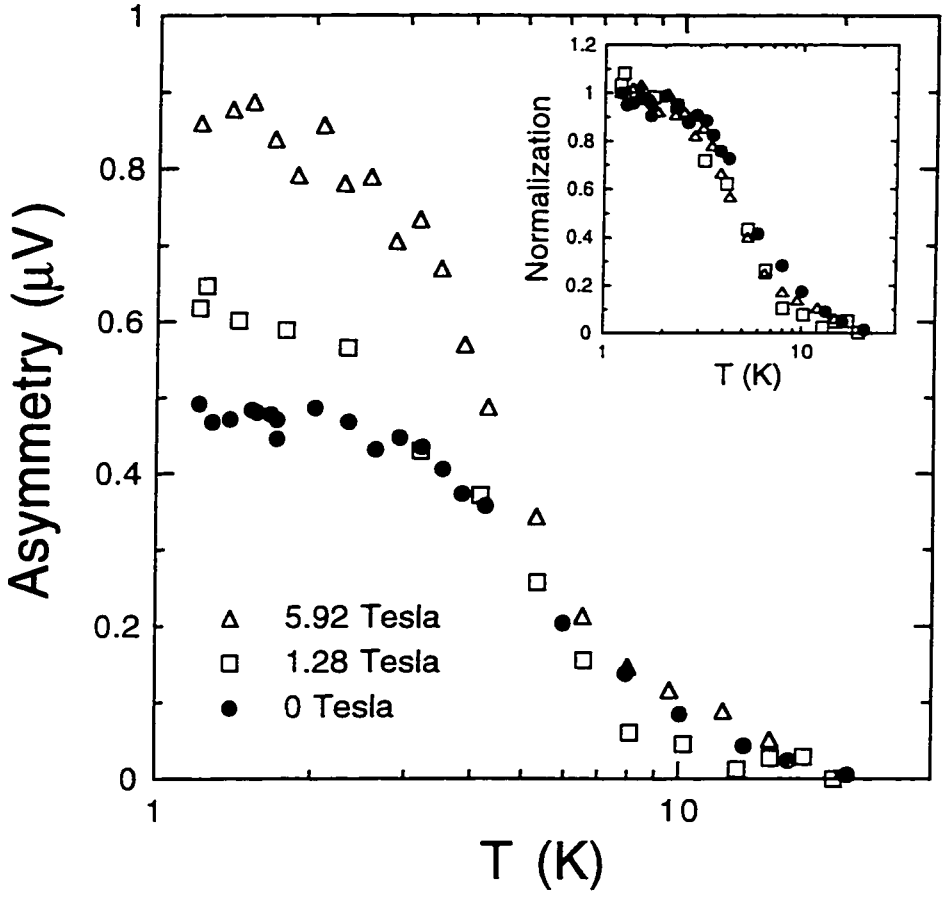

Figure 6.13: Asymmetry as a function of T at various magnetic fields. The narrow 0.4 at% AuFe wire has $W = 85$ nm, $L = 3.5$ μm, and $t = 330$ Å. Inset: Normalized asymmetry as a function of T. All three curves go into a single functional form.

We already know that as T is lowered the asymmetry of a narrow 0.2 at% AuFe wire gradually grows and saturates at a temperature which is comparable to the resistivity maximum temperature (see Fig. 6.10). The measurement in Fig. 6.10 was done in zero magnetic field. One might want to know about the effect of magnetic field on the asymmetry.

To answer this issue, we performed $dV/dI(I)$ measurements as a function of temperature at three different magnetic fields $H = 0$, 1.28, and 5.92 Tesla. For each field $dV/dI(I)$ at a variety of different bath temperatures have been measured, and finally the asymmetry was estimated as a function of T. The resulting asymmetry has been shown in Fig. 6.13. The asymmetry increases as H is increased up to $\sim$ 6 Tesla (We will discuss the results for higher field in Section 6.2.4), while the saturation temperature of the asymmetry does not move with H. This fact can be seen more clearly if the normalized asymmetry is drawn as a function of T. The Inset of Fig. 6.13 shows the normalized asymmetry as a function of T. All three curves at different magnetic fields collapse onto a single functional curve, clearly indicating that the saturation temperature is independent of H.

6.2.4 Sensitivity of $dV/dI(I)$ sensitive to the four-terminal measurement configuration

As many measurements have indicated, a sensitivity to the four-terminal measurement configuration is a hallmark of mesoscopic systems [15, 36]. The condition to

observe such an effect is that the size of a sample should be less than the phase coherence length. Benoit *et al.* [15] noted that the four terminal magnetic field dependent conductance $G(H)$ of small metallic wires and loops was asymmetric in H and sensitive to the configuration of current and voltage contacts, even though classically the same sample was being measured. Buttiker [31] explained this as a consequence of the mixing of diagonal and off-diagonal components of the conductance in a four terminal phase coherent sample.

To test the possibility that such quantum interference effects may still survive in our samples, we performed $dV/dI(I)$ measurements as we changed the four-terminal measurement configuration.

Fig. 6.14 shows the resulting $dV/dI(I)$ of a narrow 0.4 at% AuFe wire for four different measurement configurations. For all four configurations the samples are identical from the classical point of view, and the direction of dc bias current I is also identical. Hence, one expects the same $dV/dI(I)$ for each configuration. However, we found *the resulting dV/dI(I) is sensitive to the four-terminal measurement configuration.* None of the curves show the same asymmetry. However, the symmetric parts of these four curves are found to be the same.

A similar sensitivity of the asymmetry to the four-terminal measurement configurations has been found in many other AuFe spin glass wires with narrow widths. However, the polarity of the asymmetry as well as the magnitude are different from sample to sample even if the four-terminal measurement configuration is the same.

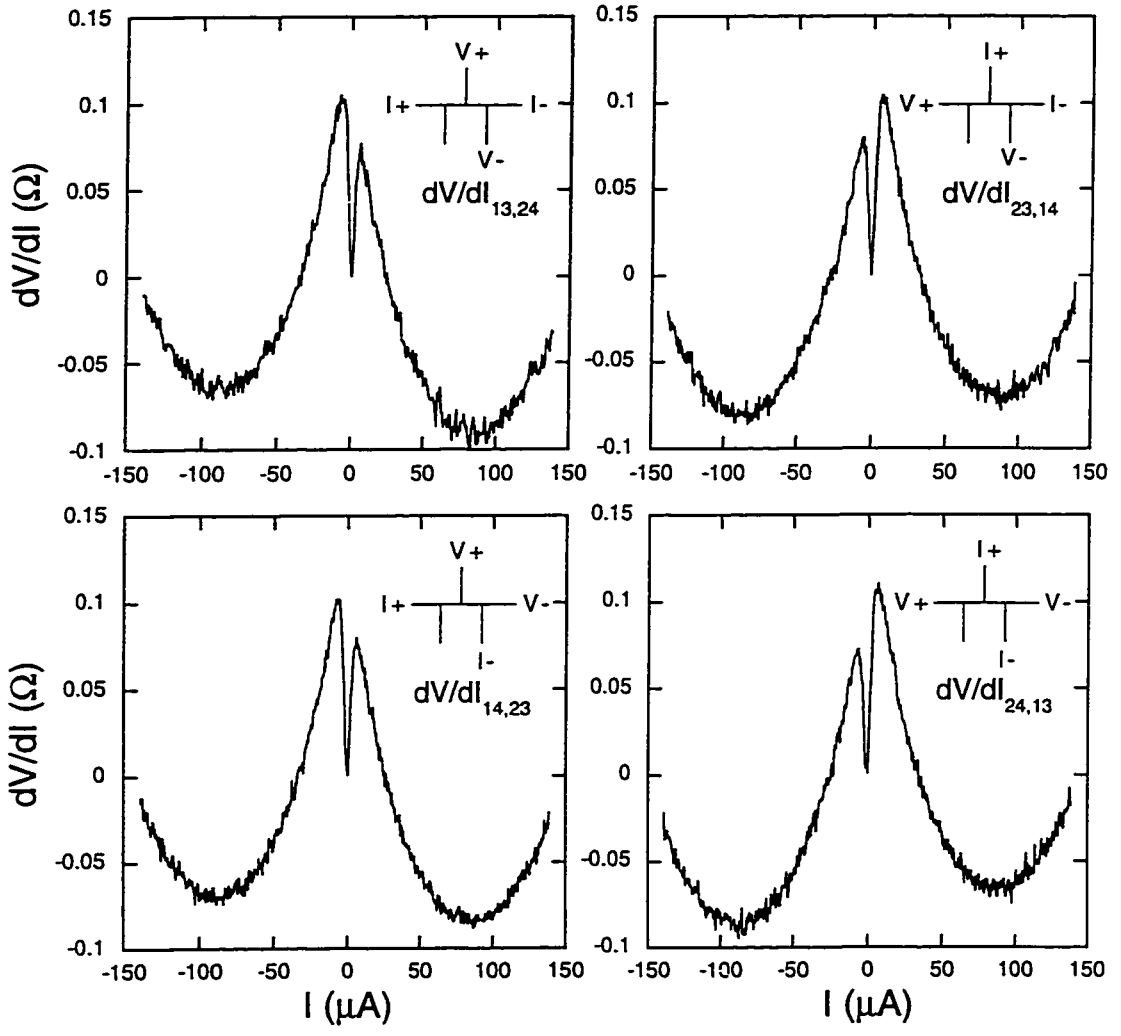

Figure 6.14: $dV/dI(I)$ for four different measurement configurations at $T = 1.56$ K. The narrow 0.4 at% AuFe wire has $W = 85$ nm, $L = 3.5$ μm, and $t = 330$ Å.

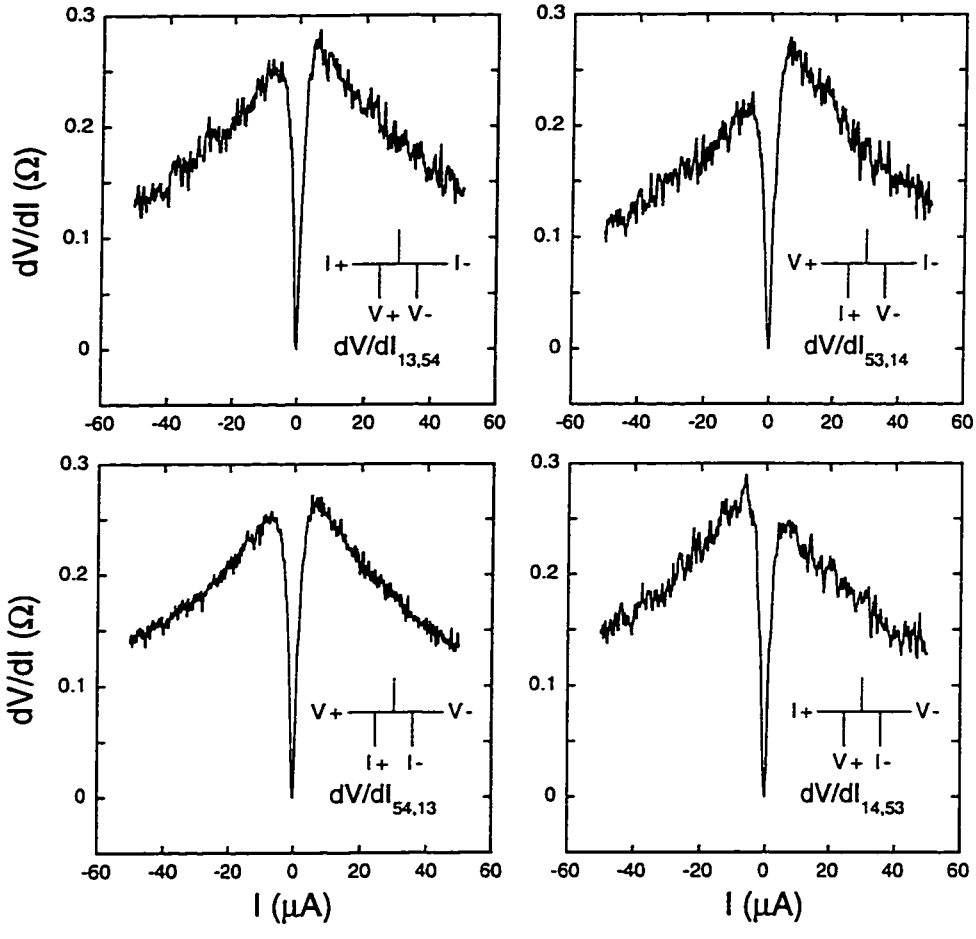

Figure 6.15: $dV/dI(I)$ for four different measurement configurations at zero magnetic field. The narrow 0.4 at% AuFe wire has $W = 80$ nm, $L = 3.7$ μm, and $t =$ 330 Å. $T = 106$ mK.

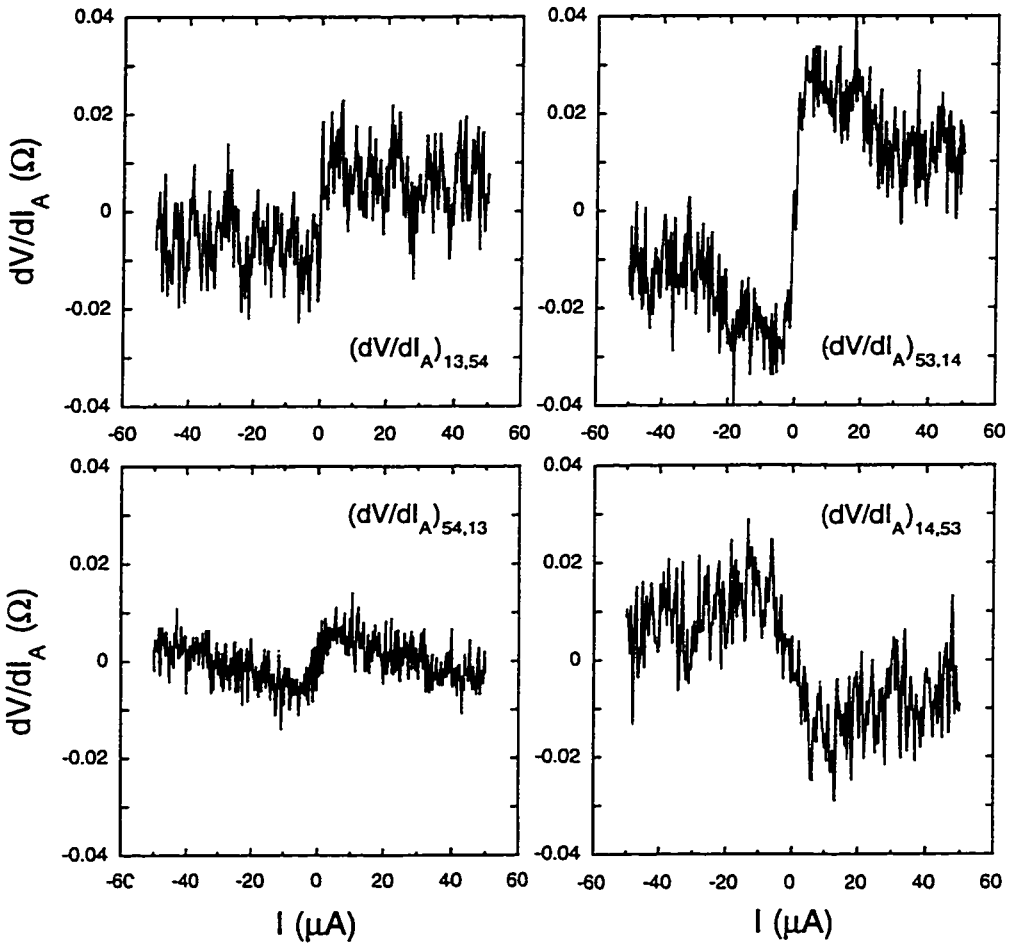

Figure 6.16: $dV/dI_A(I)$ for four different measurement configurations at zero magnetic field. $dV/dI_A(I)$ is numerically obtained from $dV/dI(I)$ in Fig. 6.15.

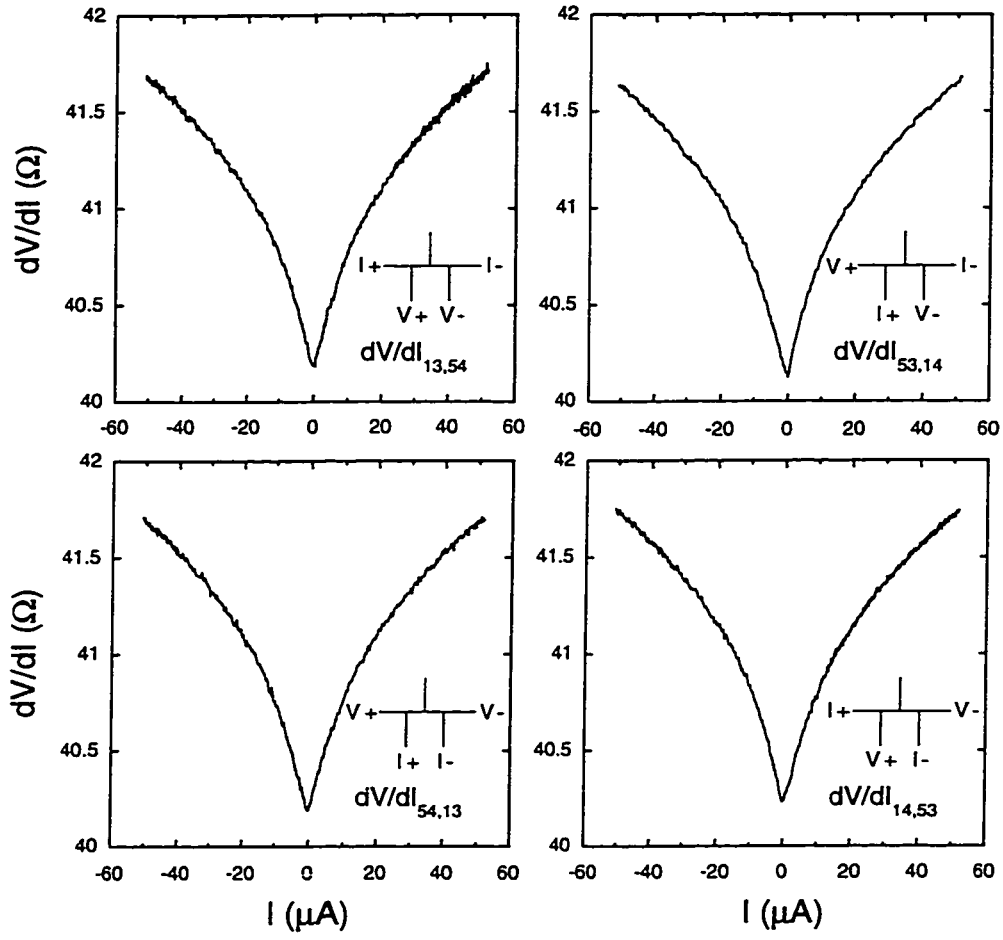

Figure 6.17: $dV/dI(I)$ for four different measurement configurations at $H = 11.9$ Tesla. The narrow 0.4 at% AuFe wire has $W = 80$ nm, $L = 3.7$ μm, and $t = 330$ Å. $T = 106$ mK.

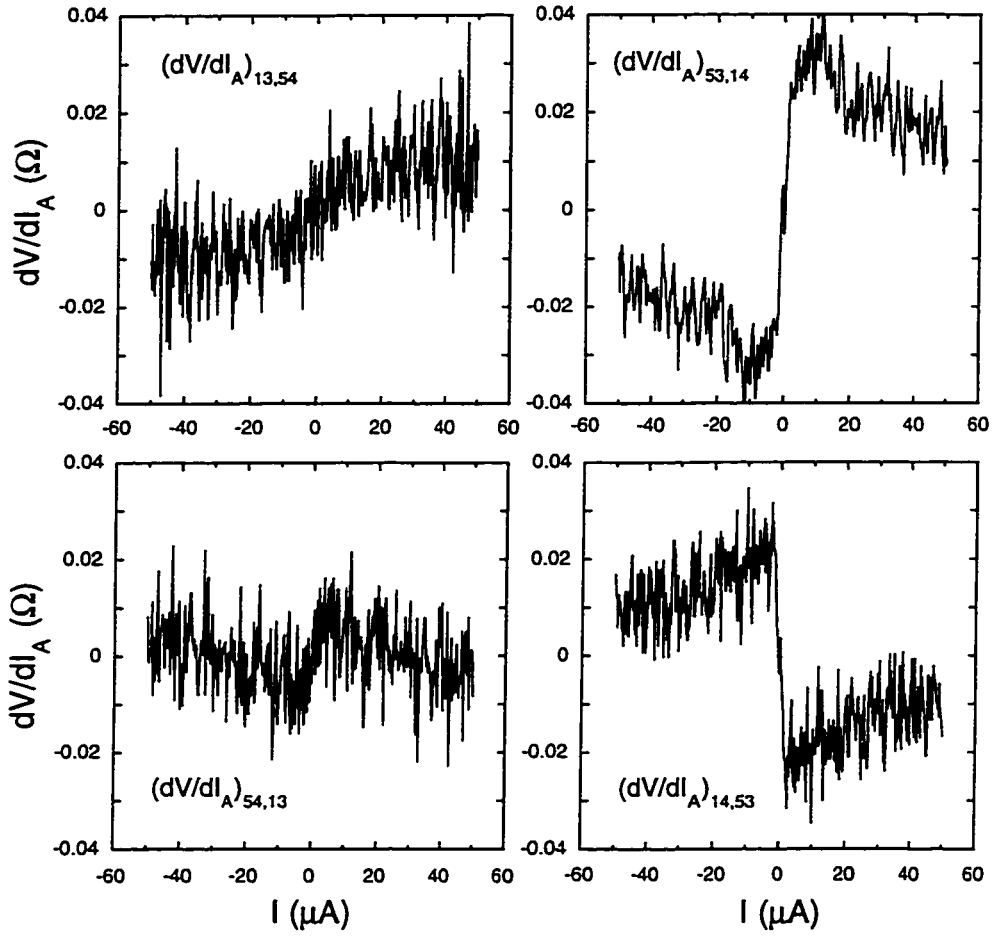

Figure 6.18: $dV/dI_A(I)$ for four different measurement configurations at $H = 11.9$ Tesla. $dV/dI_A(I)$ is numerically obtained from $dV/dI(I)$ in Fig. 6.17.

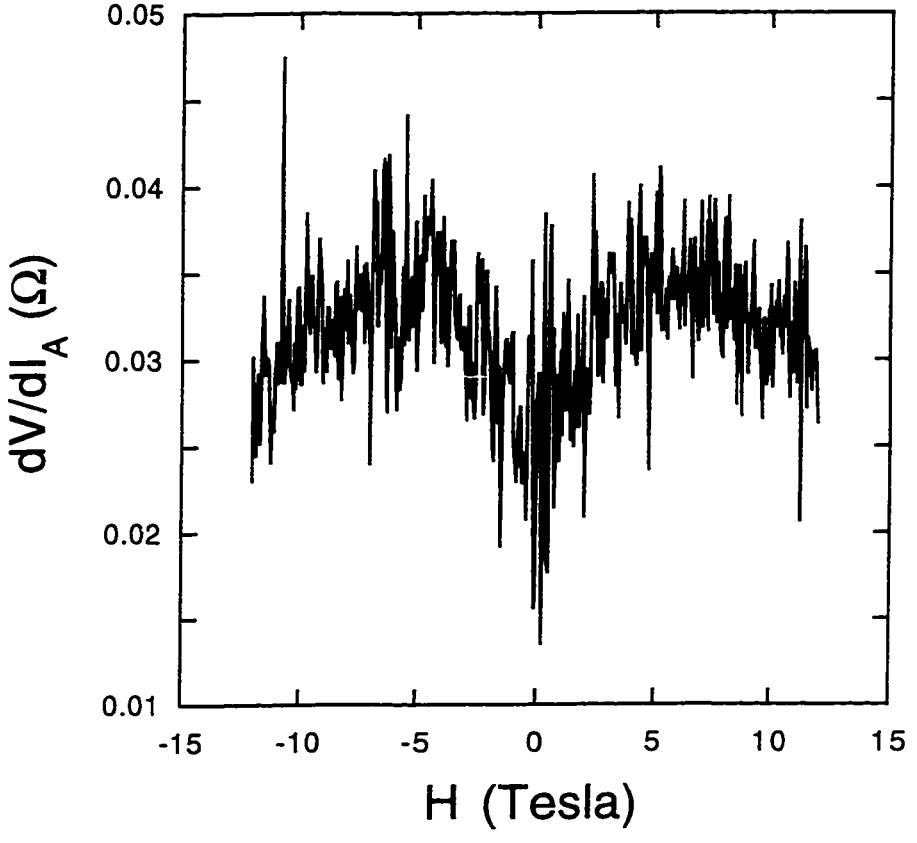

Figure 6.19: $dV/dI_A(H)$ for the measurement configuration $dV/dI_{53,14}$. The narrow 0.4 at% AuFe wire has $W = 80$ nm, $L = 3.7$ μm, and $t = 330$ Å. $T = 106$ mK

Since spin glasses are easily affected by magnetic field, one may expect that the magnetic field affects the sensitivity of $dV/dI(I)$ to measurement configuration. We want to know whether $dV/dI_A(I)$ for each configuration is sensitive to magnetic field.

To answer this question we first measured $dV/dI(I)$ of a narrow 0.4 at% AuFe wire at zero magnetic field (See Fig. 6.15). The corresponding antisymmetric part, dV/dI_A is plotted in Fig. 6.16. As expected, each configuration gives a different asymmetry. After this measurement we applied a magnetic field (11.9 Tesla) perpendicular to the sample and $dV/dI(I)$ for each configuration was measured. The resulting $dV/dI(I)$'s are shown in Fig 6.17 and the corresponding antisymmetric parts are shown in Fig. 6.18. To our surprise the polarity of asymmetry is rather robust even in such a high magnetic field and is the same for all four different configurations. The magnitude of the asymmetry is also more or less the same as before applying the magnetic field.

To see in more detail the dependence of the asymmetry on the magnetic field, we took two traces of dV/dI at $I = +5$ and -5 μA as a function of H and extracted the antisymmetric part of $dV/dI_{5\mu A}(H)$ numerically. Specifically,

$$\left(\frac{dV}{dI}\right)_A(H) = \frac{1}{2}\left[\left.\frac{dV}{dI}\right|_{I=5\mu A}(H) - \left.\frac{dV}{dI}\right|_{I=-5\mu A}(H)\right] \tag{6.2}$$

The resulting $dV/dI_A(H)$ is been shown in Fig. 6.19. The field dependence of $dV/dI_A(H)$ is not monotonic. The asymmetry increases with H in the field regime below 6 Tesla, while the asymmetry decreases with H in the field regime above 6

Tesla. This result provides evidence for the fact that the origin of the antisymmetric part of $dV/dI(I)$ is different from the origin of the resistivity of the sample. Remember that the resistivity maximum temperature just shows monotonic behavior in its magnetic field dependence, as shown in Fig. 5.2. The origin of the antisymmetric part of $dV/dI(I)$ will be discussed in a later section.

6.2.5 Is the asymmetry in $dV/dI(I)$ a quantum interference effect?

The origin of quantum interference effects in condensed matter lies in the phases of electrons (or holes). In mesoscopic samples where the electron phase coherently contributes to the transport properties, quantum interference effects reveal themselves in the magnetoresistance, or conductance as a function of gate potential, etc. The important properties of these interference effects include the facts that (1) they are sample specific and sensitive to the detailed impurity configuration, and (2) they are non-additive in a classical way, *i.e.*, the phase plays an important role.

$dV/dI(I)$ of narrow AuFe wires looks like a quantum interference effect in the sense that the asymmetries in $dV/dI(I)$ are sample specific and sensitive to probe configurations. However, we still need to check the second property listed above before we conclude that $dV/dI(I)$ of AuFe spin glass wires is a quantum interference effect. Usually quantum interference effects are defined by certain fundamental length scales. L_φ and L_T are good examples of such fundamental length scales. Due to these properties, most quantum interference effects are not

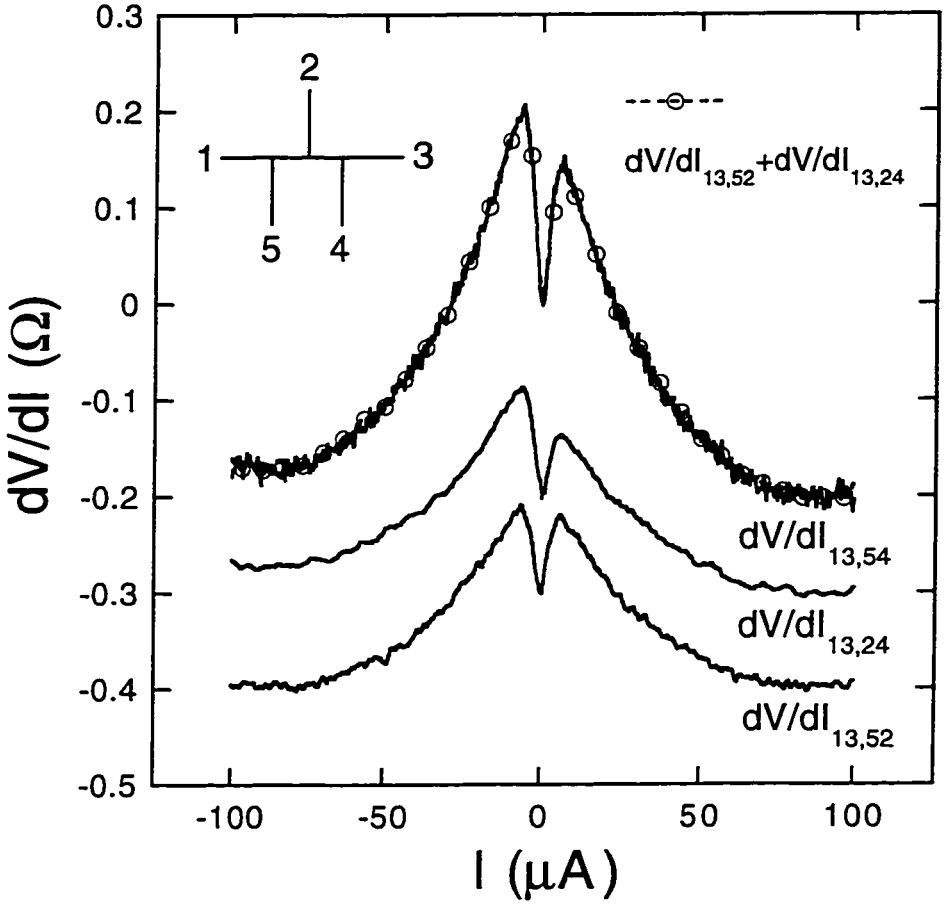

Figure 6.20: $dV/dI(I)$'s of consecutive sections. The narrow AuFe 0.4 at% wire has $W = 85$ nm, $L = 7.0$ μm between contacts 4 and 5, and $t = 330$ Å. Data are taken at $T = 1.557$ K

additive in a classical way. It is worthwhile to check whether these aspects of quantum interference phenomena are observable in the $dV/dI(I)$ of narrow AuFe wires.

Fig. 6.20 answers the above issue. In a five-probe AuFe wire we measured $dV/dI(I)$'s of consecutive sections and checked whether $dV/dI(I)$ is additive. It turns out that $dV/dI(I)$'s of two consecutive sections are exactly additive. The numerical sum of the differential resistances of two consecutive sections ($dV/dI_{13,52}$+ $dV/dI_{13,24}$) is identical to the differential resistance of the entire section ($dV/dI_{13,54}$). *The $dV/dI(I)$'s are additive in a classical way.*

Further evidence against the possibility of quantum interference effects in $dV/dI(I)$ is found in the fact that the asymmetry is rather insensitive to the detailed microscopic spin configuration. The spins in a magnetic alloy freeze at the spin glass transition, but the microscopic configuration of the frozen spins changes at each cooling. This fact has been demonstrated [44] by the phenomena of the *magnetofingerprint.* The detailed pattern of the magnetoresistance as a function of field changes at each different cool-down. However, $dV/dI(I)$ of a narrow AuFe wire does not change even after several thermal cyclings from room temperature to liquid helium temperature. *Consequently we believe the asymmetry in $dV/dI(I)$ is not a quantum interference effect.*

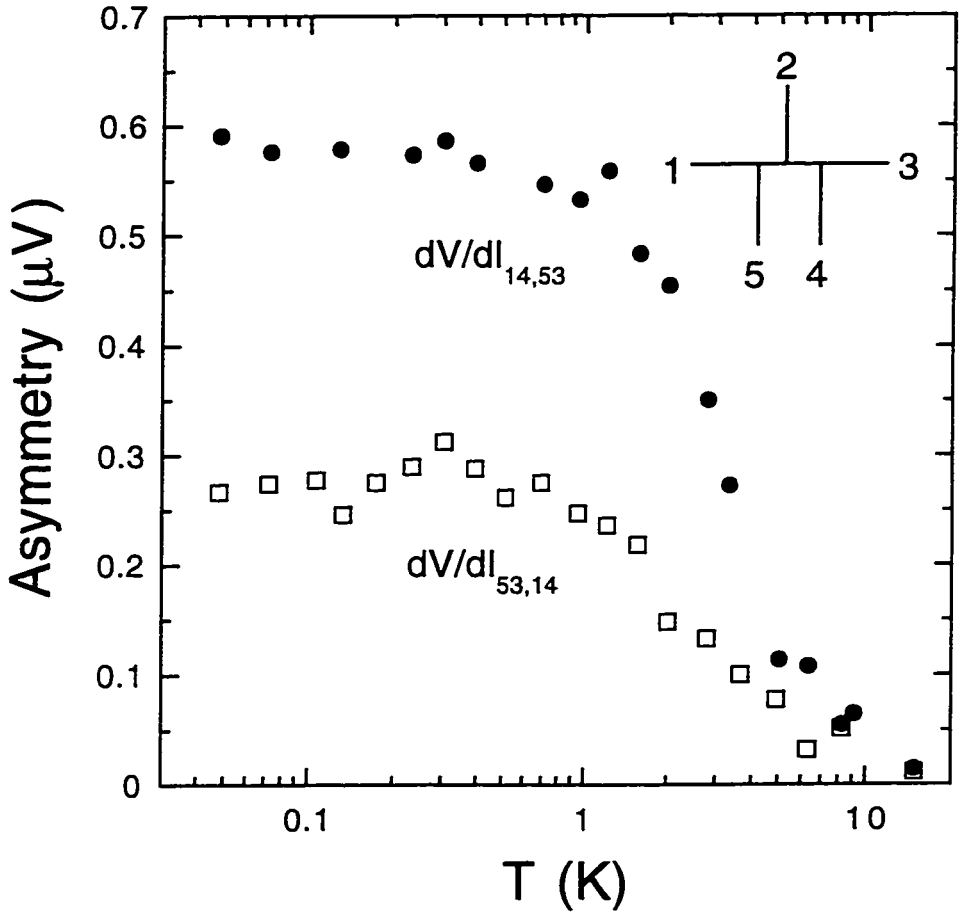

Figure 6.21: Asymmetry as a function of T for two different configurations. The narrow 0.4 at% AuFe wire has $W = 80$ nm, $L = 3.7$ μm between contacts 4 and 5, and $t = 330$ Å.

6.2.6 *Asymmetry saturation temperature for different configurations*

In this short section we are going to show the temperature dependence of the asymmetry for different measurement configurations. Fig. 6.21 shows the asymmetry as a function of temperature for two different configurations $dV/dI_{14,53}$ and $dV/dI_{53,14}$. The sample is the same as the one in Fig. 6.15. The measured section is classically the same, but $dV/dI(I)$ shows a different asymmetry as shown in Fig. 6.16. The asymmetry in $dV/dI_{14,53}$ is larger than that in $dV/dI_{53,14}$. However, we found rather interesting property for the temperature where the asymmetry saturates. The saturation of the asymmetry occurs almost at the same temperature $\sim$ 2 K for both configurations.

6.2.7 *Searching for the origin of the asymmetry*

What is the origin of the asymmetry in $dV/dI(I)$? We have shown it is clearly associated with the presence of magnetic impurities in samples. One possibility is that this phenomenon may be related to the enhanced thermopower in magnetic alloys [97]. In what follows, we justify that the thermopower of AuFe alloys is the origin of the asymmetry in $dV/dI(I)$.

The voltage $V(I)$ across a sample can be expanded in a Taylor series with terms symmetric in I and terms antisymmetric in I:

$$V(I) = RI + R_2I^2 + R_3I^3 + R_4I^4 + ... \tag{6.3}$$

The symmetric terms in $V(I)$ actually give rise to the antisymmetric terms in

$dV/dI(I)$.

Now let us think about the origin of the even order terms in Eq. 6.3 in view of thermoelectric effects. When a temperature difference $\Delta T = T_1 - T_2$ exists along a sample, the thermoelectric voltage developed between points 1 and 2 is given by

$$V_{th} = \int_{T_1}^{T_2} S dT \tag{6.4}$$

where S represents *thermopower* of the sample. As we stated in Section 3.5.3, V_{th} contributes to the antisymmetric part of $dV/dI(I)$. To check this idea experimentally we measured $dV/dI(I)$ of a heterogeneous sample, which has a large thermopower difference between two voltage terminals. The heterogeneous sample consists of a five probe AuFe 0.4 at% wire and a 1 μm width Ge/Au wire, which is made of 50 Å thick Ge layer and 250 Å thick Au layer. Ge/Au is metallic with this thickness ratio, and is expected to have a small thermopower compared to AuFe alloys [41]. Fig 6.22(a) shows the structure of the heterogeneous sample. The terminal 3 is a line made of Ge/Au, and the other terminals are 0.4 at% AuFe wire with $\sim$ 1 μm width. Fig 6.22(b) shows the differential resistance as a function of I for the configuration $dV/dI_{21,34}$. One of the two voltage terminals is made of AuFe alloy and the other Ge/Au. dV/dI is clearly asymmetric in I, which is due to the fact that the thermopower of AuFe is large [97] while that of Ge/Au is small [41].

Now we exchange the $I+$ and $V+$ terminals in the configuration $dV/dI_{21,34}$. Classically this terminal exchange is not expected to cause any difference since the measured section is still the same as before. However, $dV/dI_{31,24}$ have no asym-

metry (Fig 6.22(c)). This is consistent with the fact that thermoelectric voltage is zero when two voltage terminals have the same thermopower regardless of the magnitude of the absolute thermopower. We finally conclude that *the difference of the thermopower of two voltage terminals gives rise to the asymmetry in* $dV/dI(I)$.

In addition we demonstrate that the symmetric part of $dV/dI(I)$ does not depend on a four-terminal measurement configuration (see Fig. 6.22(c)). The symmetric part of $dV/dI_{21,34}$, which is numerically extracted from $dV/dI_{21,34}(I)$ in Fig. 6.22(b), is identical to $dV/dI_{31,24}(I)$. This confirms that only the antisymmetric part of the differential resistance is sensitive to the four-terminal measurement configuration.

6.3 $dV/dI(I)$ of multi-probe 0.3 at% AuFe wires

In the previous section, we reached the conclusion that the observed asymmetry in $dV/dI(I)$ is closely related to a thermoelectric voltage, which originates from the thermopower difference between two voltage terminals. However, this conclusion puzzles us because a narrow AuFe wire, the terminals of which are essentially made of identical material (AuFe), should not give rise to thermoelectric voltage. There must be something more in narrow AuFe wires to explain the observed asymmetry. First of all, we have to answer the question why the asymmetry in $dV/dI(I)$ is found only in narrow samples. The second question regards the sample length. So far narrow samples normally have short length less than ~ 5 μm. Is sample length

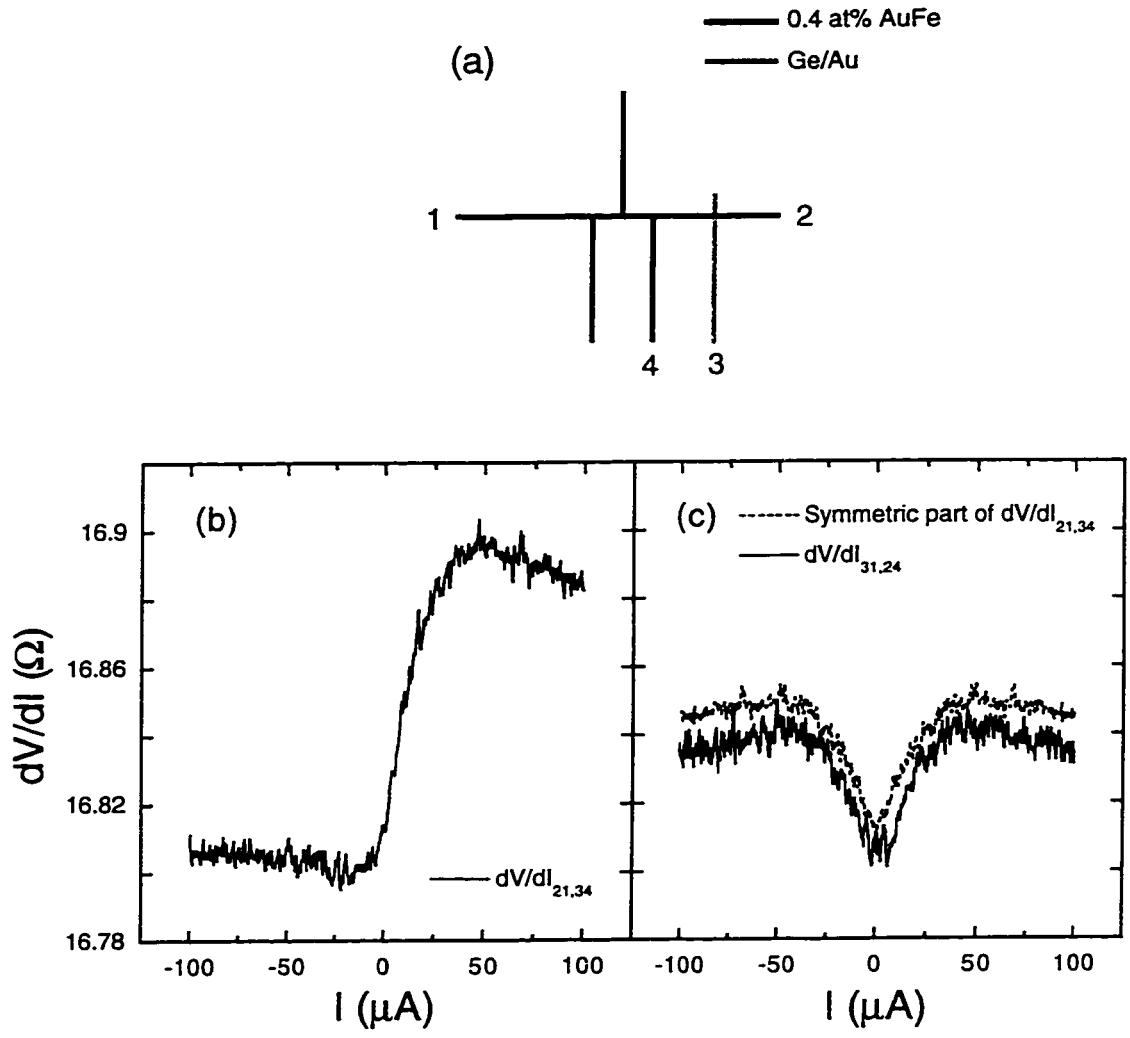

Figure 6.22: Asymmetric $dV/dI(I)$ of a heterogeneous wire. (a) On top of a 5 probe 0.4 at% AuFe wire ($W = 1$ μm, $t = 330$ Å), an Ge/Au line was made by SEM lithography and thermal evaporation. Width of the line is ~ 1 μm, and the thickness of the line 300 Å (Ge = 50 Å and Au = 250 Å). The distance between contacts 3 and 4 is $\sim 15.7\mu$m. (b) $dV/dI_{21,34}(I)$ at $T = 1.36$ K. (c) Comparison between $dV/dI_{31,24}(I)$ at $T = 1.36$ K and the symmetric part of $dV/dI_{21,34}(I)$.

also important?

To address this question, we made multi probe samples which can be studied for various measurement configurations as well as various sample lengths. The SEM micrograph of one of typical samples is shown in Fig 6.23. The horizontal line ($W \approx 60$ nm) is usually narrower than the vertical lines ($W \approx 110$ nm).

6.3.1 $dV/dI_A(I)$ sensitive to the width difference of two voltage probes

The first task we want to figure out was the question regarding the length dependence of the asymmetry in the $dV/dI(I)$ of narrow AuFe wires. We measured sample sections with various lengths from 1.5 to 28 μm. Fig. 6.24(a) shows the measurement configurations, by which $dV/dI(I)$'s for the different lengths were measured. To change the sample length from 1.5 to 8.5 μm, we move only $I-$, keeping the other terminals the same. Only for the 28 μm length we moved the $V+$ terminal to the far end. The reason why we are so careful about choosing terminals is that the asymmetry depends on the specific measurement configuration. One should try to keep the configuration the same as much as possible in four-terminal measurement configurations. The resulting $dV/dI_A(I)$ is shown in Fig. 6.24(b), which clearly demonstrates that $dV/dI_A(I)$ *is independent of sample length.* This result confirms that the width of the wires plays the most important role in $dV/dI_A(I)$.

The second task was to figure out the importance of the four-terminal mea-

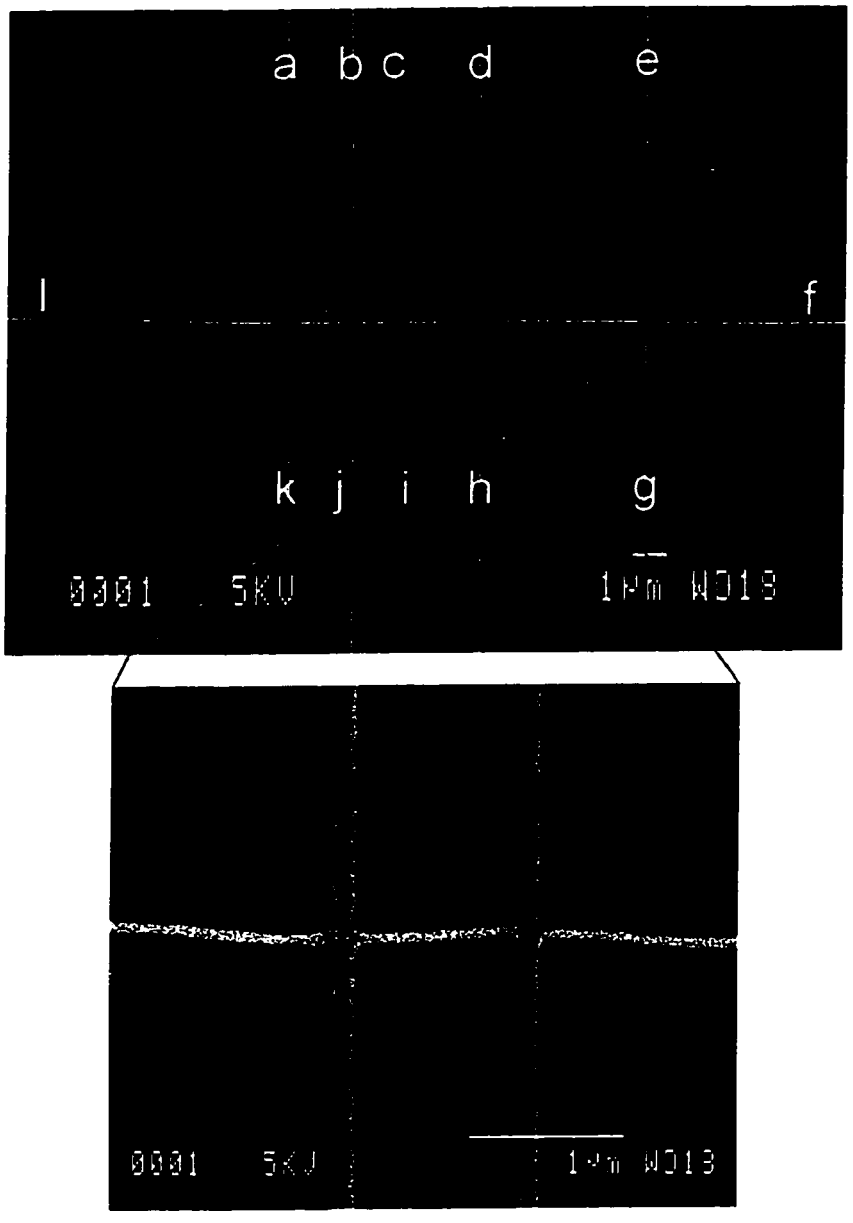

Figure 6.23: SEM micrograph of a typical 0.3 at% AuFe sample. The horizontal line ($W \approx 60$ nm) is usually narrower than the vertical lines ($W \approx 110$ nm). The film thickness is 303 Å.

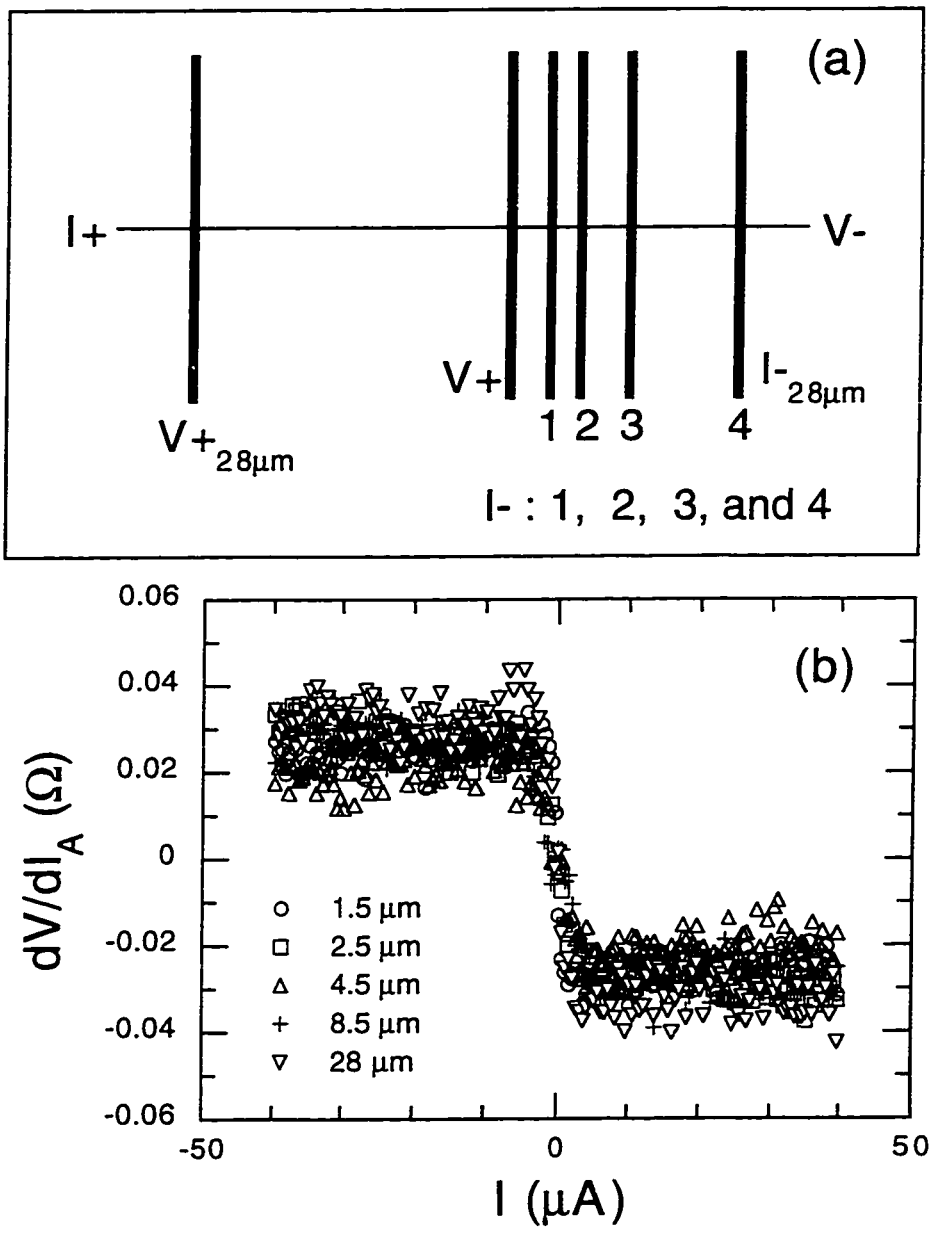

Figure 6.24: $dV/dI_A(I)$ for various sample lengths. (a) Measurement configurations for each different length. (b) $dV/dI_A(I)$ for various lengths.

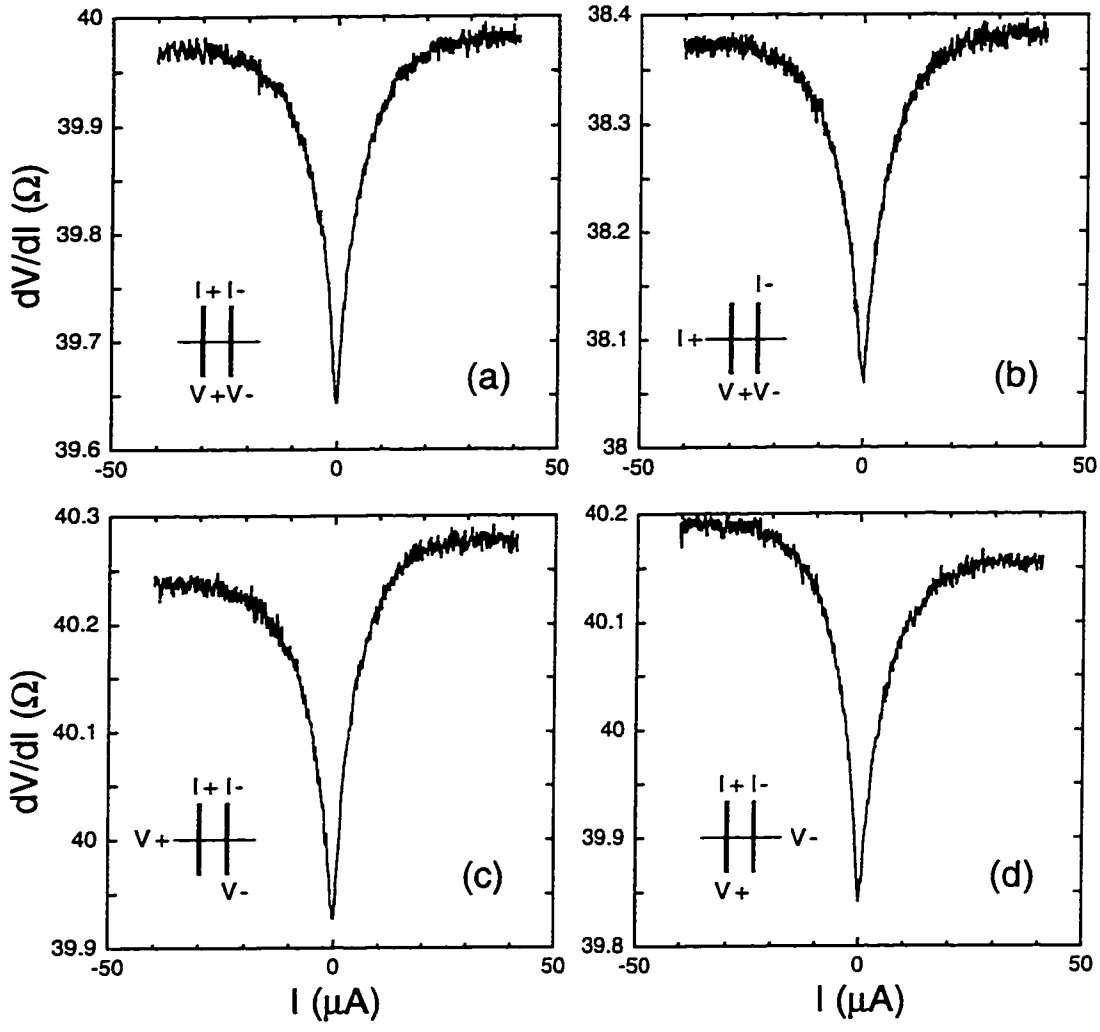

Figure 6.25: $dV/dI(I)$ of a 0.3 at% AuFe wire for various measurement configurations. Inset to each panel illustrates the specific terminal configuration. The width of vertical wires is 110 nm, the width of the horizontal wire 60 nm. $L = 2\mu$m, $t =$ 303 Å. $T = 0.45$ K.

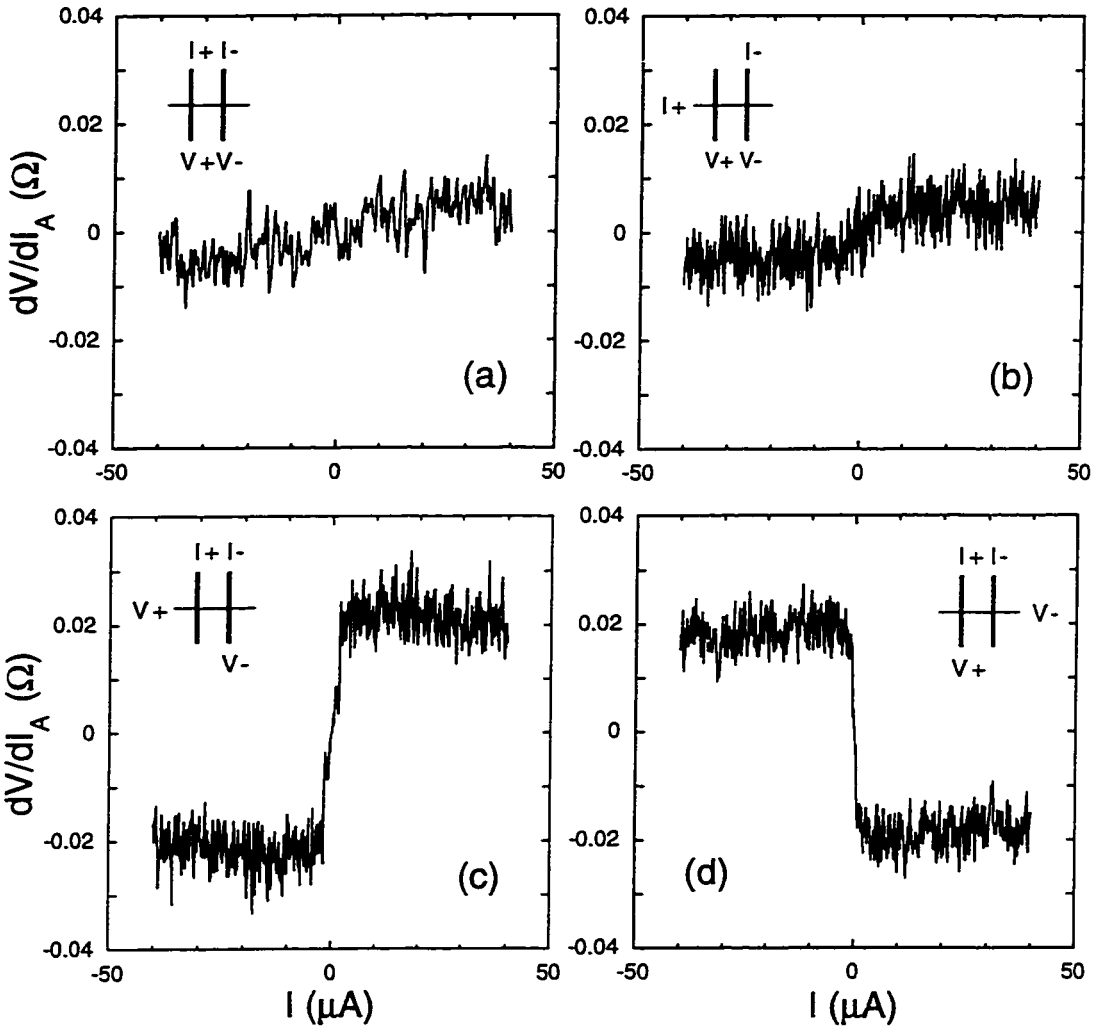

Figure 6.26: $dV/dI_A(I)$ of a 0.3 at% AuFe wire for various measurement configurations. Inset to each panel illustrates the specific terminal configuration. $dV/dI_A(I)$ is numerically obtained from $dV/dI(I)$ in Fig. 6.25.

surement configuration. Fig. 6.25 shows $dV/dI(I)$ of a 0.3 at% AuFe wire for four different measurement configurations. The corresponding dV/dI_A are shown in Fig. 6.26. The polarity and magnitude of the asymmetry depend on the measurement configuration. Each configuration measures the same section of the sample, and dc bias current flows in the same direction in each configuration.

Now let us discuss the detailed features of $dV/dI_A(I)$ in Fig. 6.26. The inset to each figure illustrates the measurement configuration. In Fig. 6.26(a) current flows from one of the vertical lines to the other vertical line, and the two voltage probes are vertical lines. In this configuration $dV/dI(I)$ is symmetric in I. In Fig. 6.26(b) we moved one of the current probes (I+) to the horizontal line, keeping other three probes the same as in Fig. 6.26(a). The resulting $dV/dI_A(I)$ does not show any major difference from that of Fig. 6.26(a), indicating that the current probe does not influence the asymmetry in $dV/dI(I)$.

In Fig. 6.26(c) we moved one of voltage probes (V+) to the narrow horizontal line, keeping other three probes the same as in Fig. 6.26(a). Then a large asymmetry develops as shown in Fig. 6.26(c). When the $V-$ probe instead of the V+ probe was moved to the narrow horizontal line (see Fig. 6.25(d)), a large asymmetry develops but had the opposite polarity compared to $dV/dI_A(I)$ in Fig. 6.26(c). Noting the results in Fig. 6.26 and the fact that the vertical lines are wider than the horizontal line, we make a few statements with regard to $dV/dI_A(I)$.

- Non-zero $dV/dI_A(I)$ of a AuFe spin glass wire is observed only when two

voltage probes have different widths from each other. However, the critical width to see a non-zero $dV/dI_A(I)$ is $\sim$ 150 nm. When the width of both voltage terminals is larger than this, no appreciable asymmetry is observed. Therefore one of voltage terminals should have a width less than 150 nm to have a non-zero $dV/dI_A(I)$.

- The polarity of $dV/dI_A(I)$ is governed by the relation between the widths of two voltage probes. When the width of the $V+$ probe is narrower (wider) than that of the $V-$ probe, $dV/dI_A(I)$ has a positive (negative) polarity.

- It turns out that the asymmetry in $dV/dI(I)$ of narrow 0.2 at% AuFe wires is also explained by the above statements. The normal SEM lithographical technique can frequently give rise to the variation in the linewidth of order $\sim$ 10 nm. This lithographical variation is the main reason for the previously observed asymmetry in $dV/dI(I)$ of very narrow wires.

These statements are very general and have been found valid in any arbitrary combination of measurement probes as well as in other multi probe samples.

6.3.2 Asymmetry as a function of temperature

Previously $dV/dI_A(I)$ of narrow AuFe 0.2 and 0.4 at% wires were found to be dependent on the temperature T. The amplitude of $dV/dI_A(I)$ increases as T is lowered, saturating below $1-2$ K. We found a very similar behavior in $dV/dI_A(I)$

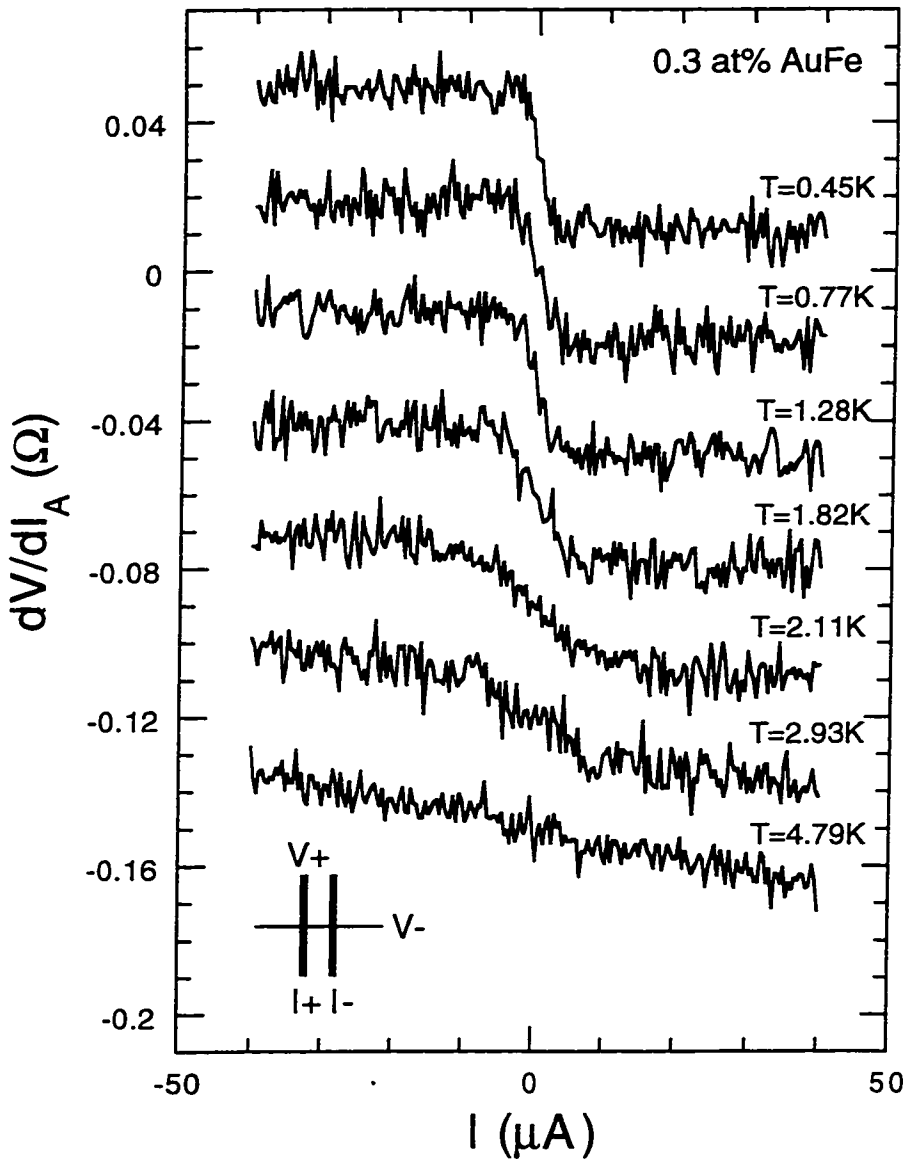

Figure 6.27: $dV/dI_A(I)$ of a 0.3 at% AuFe wire for various temperatures. The width of vertical wires is 110 nm, the width of horizontal wire 60 nm. $L = 2\mu$m, t = 303 Å. Inset: the 4-terminal measurement configuration used here.

of a 0.3 at% AuFe wire. The step-like zero bias anomaly in $dV/dI_A(I)$ at $T = 0.45$ K diminishes as T is increased, finally becoming flat above $T \approx 4$ K (see Fig. 6.27).

6.4 Thermopower of AuFe mesoscopic spin glass wires

As discussed in Section 3.5, the nontrivial $dV/dI_A(I)$ is attributed to a thermoelectric voltage, which originates from two voltage wires with different thermopower. In the case of AuFe wires, how can two voltage wires have different thermopowers? Thermopower for a normal metal is given by Eq. 3.3, and is very sensitive to $\partial\rho/\partial\varepsilon$ at the Fermi level. It is generally true that $\rho(\varepsilon)$ of bulk does not depend on the size of a sample. However, $\rho(\varepsilon)$ can be sensitive when the sample size becomes comparable to same fundamental microscopic length scale, for example, L_T, or L_φ [5]. By the same token one might expect a size dependence of $\partial\rho/\partial\varepsilon$ at the Fermi level. Consequently it is reasonable to consider a size effect of thermopower in mesoscopic metal wires. From the statements which have been drawn in Section 6.3.1, we can make following statements:

- The thermopower of a AuFe spin glass wire depends on the width of the wire if it is lower than $W = 150$ nm.

- The magnitude of the thermopower of a AuFe spin glass wire decreases as the width of the wire is reduced.

Now, we are going to estimate the thermopower difference (ΔS) between two voltage probes, one of which has W = 110 nm, and the other W = 60 nm. The estimation of thermopower requires a calculation of the electron temperature profile in a sample wire. In the following section we calculate the electron temperature profile in a sample with a dc bias current flow and then discuss the thermopower of mesoscopic AuFe spin glasses.

6.4.1 Electron temperature of a sample wire

First of all we simplified the sample structure shown in Fig. 6.23 to simplify the calculation. The simplified structure has 6 probes around a short sample section, which has been already fully studied in Section 3.5.2. The simplified structure is exactly same as in Fig. 3.8. Dc current flows between two vertical lines, and the 4-terminal measurement configuration is shown in the inset to Fig. 6.27. The scheme to calculate the electron temperature T_e has been discussed in Section 3.5.

The sample section is 2 μm long, and the other parameters used for the coefficients in Nagaev's equation are D = 105 cm^2/sec, W_c = 110 nm, L_c = 15.5 μm, W_{v1} = 110 nm, L_{v1} = 24.5 μm, W_{v3} = 60 nm, L_{v2} = 24.5 μm,$R_\square$ =!1.22 Ω, Θ_D = 170 K, and α_{ph} = 0.415. Fig. 6.28 shows T_e of the short sample section as a function of I at various bath temperatures. Here we assumed that the T_e profile is constant within the short sample section. The estimated T_e indicates that the efficiency of electron heating by I increases as the bath temperature T is lowered.

This is simply because the electron-phonon scattering rate ($\propto T^3$) decreases as T is lowered.

6.4.2 Thermopower of mesoscopic AuFe spin glasses

The thermopower difference (ΔS) of two AuFe wires with different widths is obtained from Eq. 3.52, which can be rewritten in the form of

$$S_{v+} - S_{v-} = \left(\frac{dT_e}{dI}\right) \Big/ \left(\frac{dV}{dI}\right)_A \tag{6.5}$$

$dV/dI_A(I)$ is obtained from a measurement at $T = 0.45$ K, which is shown in Fig. 6.27, and $T_e(I)$ which was calculated in the previous subsection. Therefore ΔS ($= S_{w=110nm} - S_{w=60nm}$) can be obtained as a function of T_e, and the result is plotted in Fig. 6.29. The magnitude of ΔS increases as T_e is increased up to $T_e \approx 5.5$ K.

Fig. 6.29 is very useful when we reconstruct $dV/dI_A(I)$ for bath temperatures from 0.45 to 5.5 K. The scheme to reconstruct $dV/dI_A(I)$ is as follows.

1. We calculate $T_e(I)$ at a certain T by Nagaev's equation.

2. Plugging $T_e(I)$ into $\Delta S(T_e)$, we get a functional form for $\Delta S(I)$.

3. Finally $dV/dI_A(I)$ is calculated by Eq. 3.52.

Eventually $dV/dI_A(I)$ for various temperatures from 0.45 to 5.5 K can be calculated and compared to measurements. The resulting calculated $dV/dI_A(I)$s are shown as

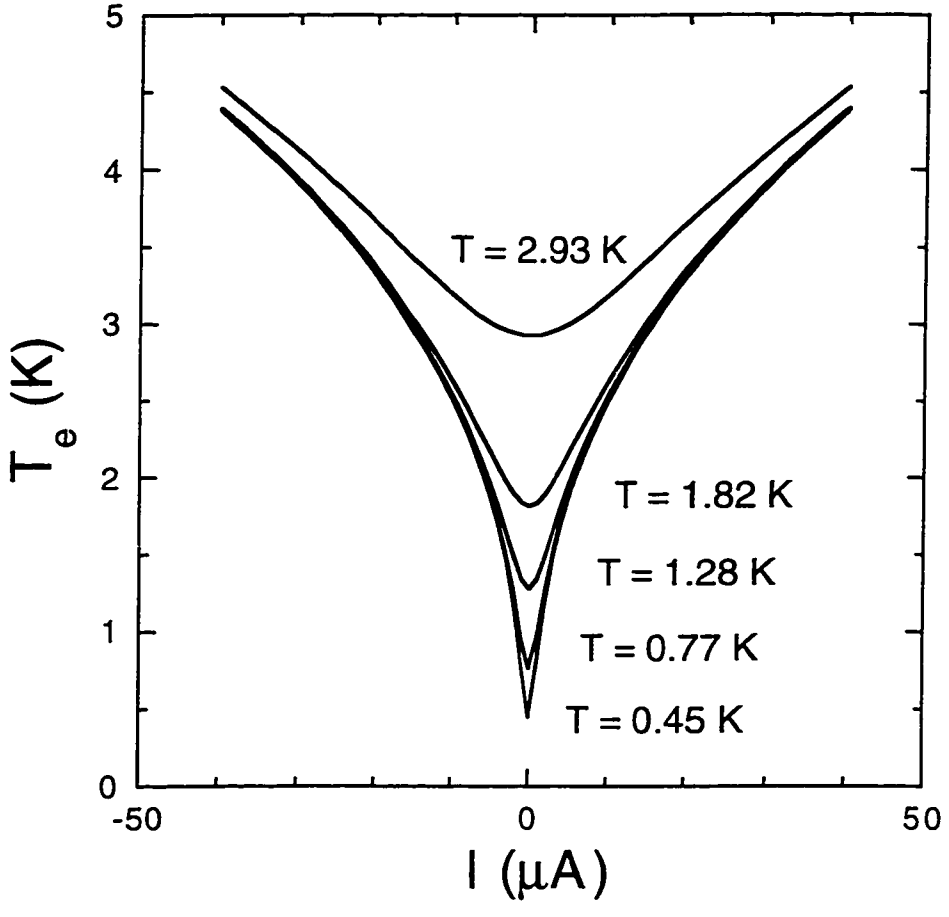

Figure 6.28: $T_e(I)$ of a 0.3 at% AuFe wire at various bath temperatures. I flows as shown in inset to Fig. 6.27.

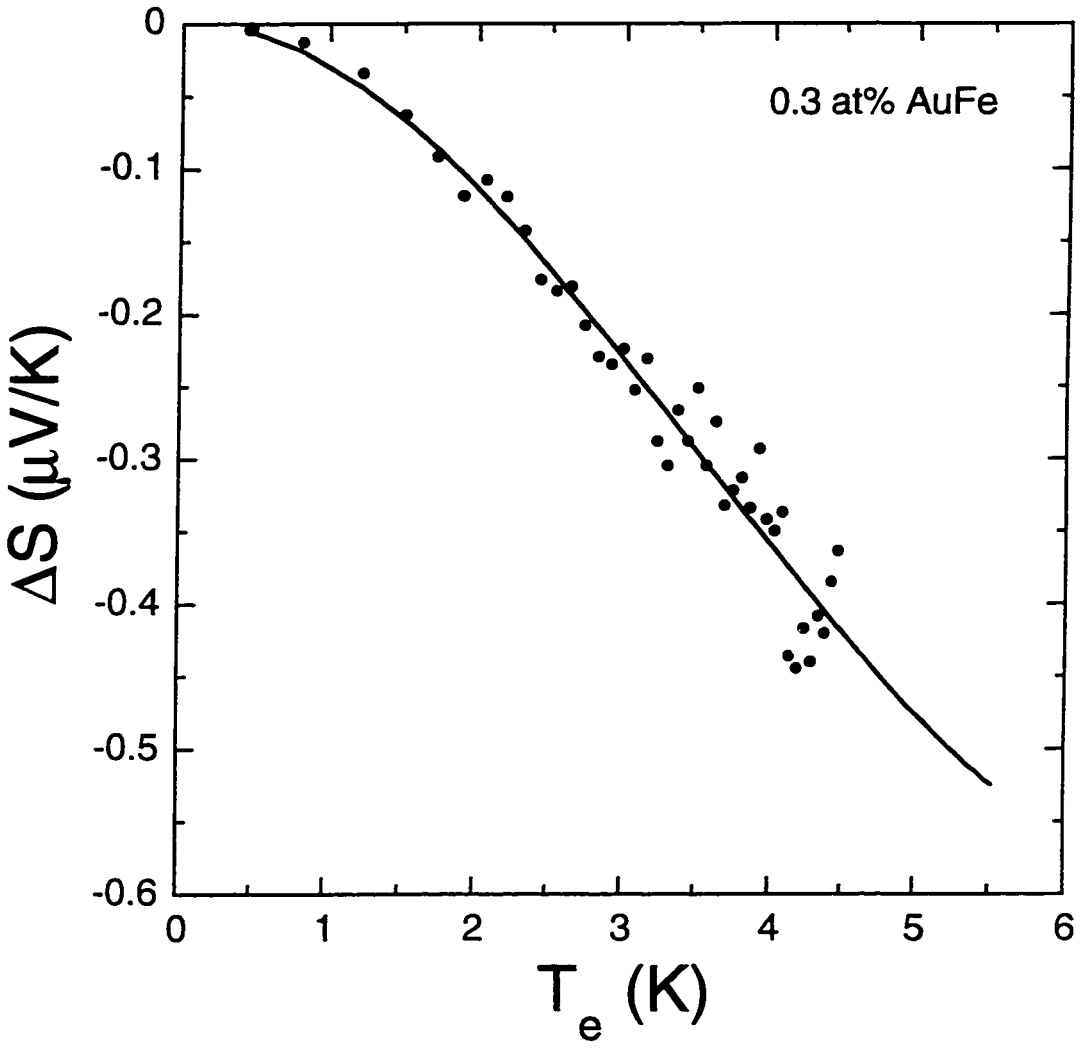

Figure 6.29: ΔS as a function of T_e. The solid line is a fit by $\Delta S = AT_e + BT_e^2 + CT_e^3$.

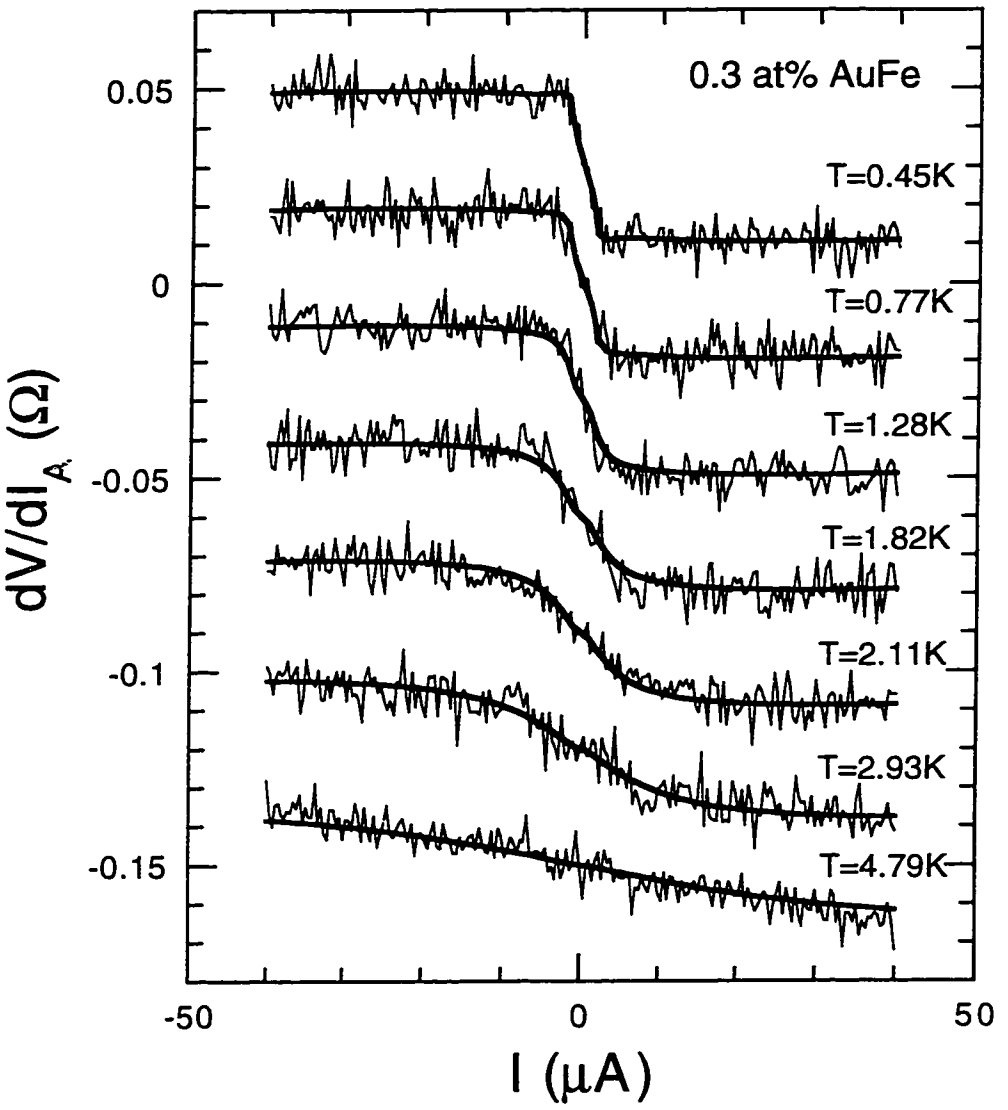

Figure 6.30: Calculated $dV/dI_A(I)$ of the 0.3 at% AuFe wire for various temperatures. Thin line: the experimental data in Fig. 6.27. Thick line: the calculated $dV/dI_A(I)$.

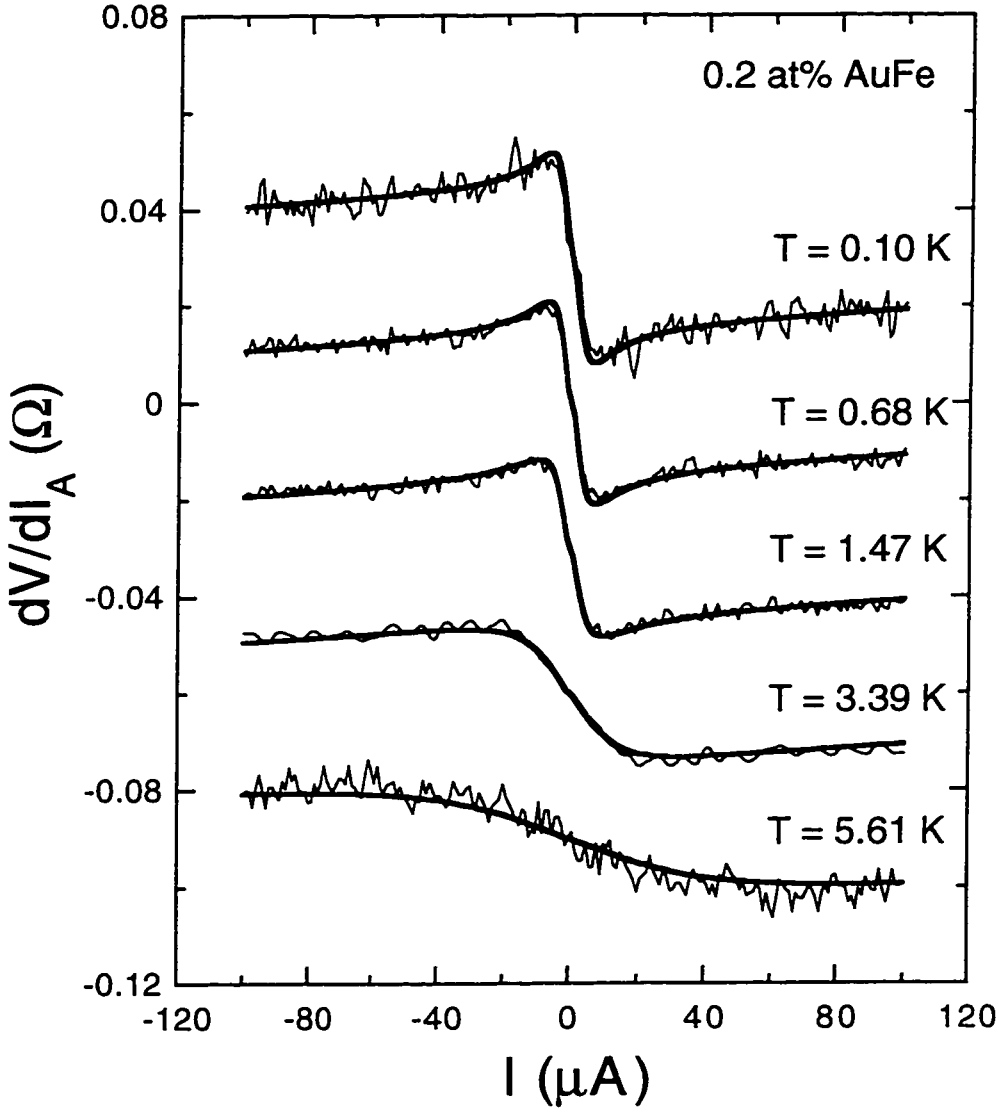

Figure 6.31: Calculated $dV/dI_A(I)$ for the 0.2 at% AuFe wire at various temperatures. Thin line: the experimental data in Fig. 6.9. Thick line: the calculated $dV/dI_A(I)$.

thick solid lines in Fig. 6.30. The calculated $dV/dI_A(I)$s are exactly superposed on top of the experimental data for all temperatures ranging from 0.45 to 4.79 K.

A similar calculation for $dV/dI_A(I)$ of the narrow 0.2 at% AuFe wire in Fig. 6.9 has been done and compared with experimental data. The calculated $dV/dI_A(I)$ is plotted in Fig. 6.31 along with the experimental data. Again, the calculated $dV/dI_A(I)$ are exactly superposed on top of measurements in a wide range of temperature.

6.4.3 More evidence for the size dependent thermopower

We have learned now that the nontrivial $dV/dI_A(I)$ originates from the thermopower difference between two voltage terminals. To account for the reason why two voltage terminals have different thermopower in AuFe samples, we assumed a size dependence of the mesoscopic thermopower of AuFe wires. However, one may point out that the thermopower variation can be caused by spatial variations of the magnetic impurity concentration in a sample. Concentration variations by their very nature are random in space, and hence cannot explain the consistent change of the asymmetry polarity in a variety of measurement configurations as shown in Figs. 6.25 and 6.26.

Nevertheless one may still insist that voltage wires may have systematic concentration variations for some reason. To clearing this issue, let us calculate the expected $dV/dI_A(I)$ due to concentration variations and compare it with observed

data.

The thermopower in a normal metal is given by [140]

$$S = \frac{\pi^2}{3}\frac{k_B}{e}k_B T \left[\frac{\partial \ln \sigma(\varepsilon)}{\partial \varepsilon}\right]_{\varepsilon=\varepsilon_F} \tag{6.6}$$

When the conductivity σ is sensitive to the energy ε of conduction electrons at the Fermi level, the thermopower S can be large. For this reason a dilute magnetic alloy in which spin flip scattering gives rise to a conductivity anomaly at the Fermi level, has a giant thermopower around the Kondo temperature. Fig. 6.32 shows $S(T)$ of AuFe alloys with various concentrations. The dashed lines are phenomenological fits to the data obtained from Ref. [97]. We used a fit equation of the form

$$S_c = \alpha\left(\frac{1}{(T+\beta)^2} - \frac{1}{\beta^2}\right) \tag{6.7}$$

where the fitting parameters α and β are given as a function of impurity concentration c in units of at%,

$$\begin{aligned} \alpha &= 12029\ c^{1.6507} \\ \beta &= 34.747\ c + 0.85225 \end{aligned} \tag{6.8}$$

As shown in Fig. 6.32 this phenomenological equation fits the data reasonably well. Using Eq. 6.7 we can estimate a thermopower variation ΔS_c caused by concentration variation $\delta c \sim 0.01$ at% at $c = 0.3$ at%. Once ΔS_c is estimated, the rest of the calculation is straightforward. Using exactly the same scheme discussed in Section 6.4.2, $dV/dI_A(I)$ at T = 0.45 K caused by the concentration variation has

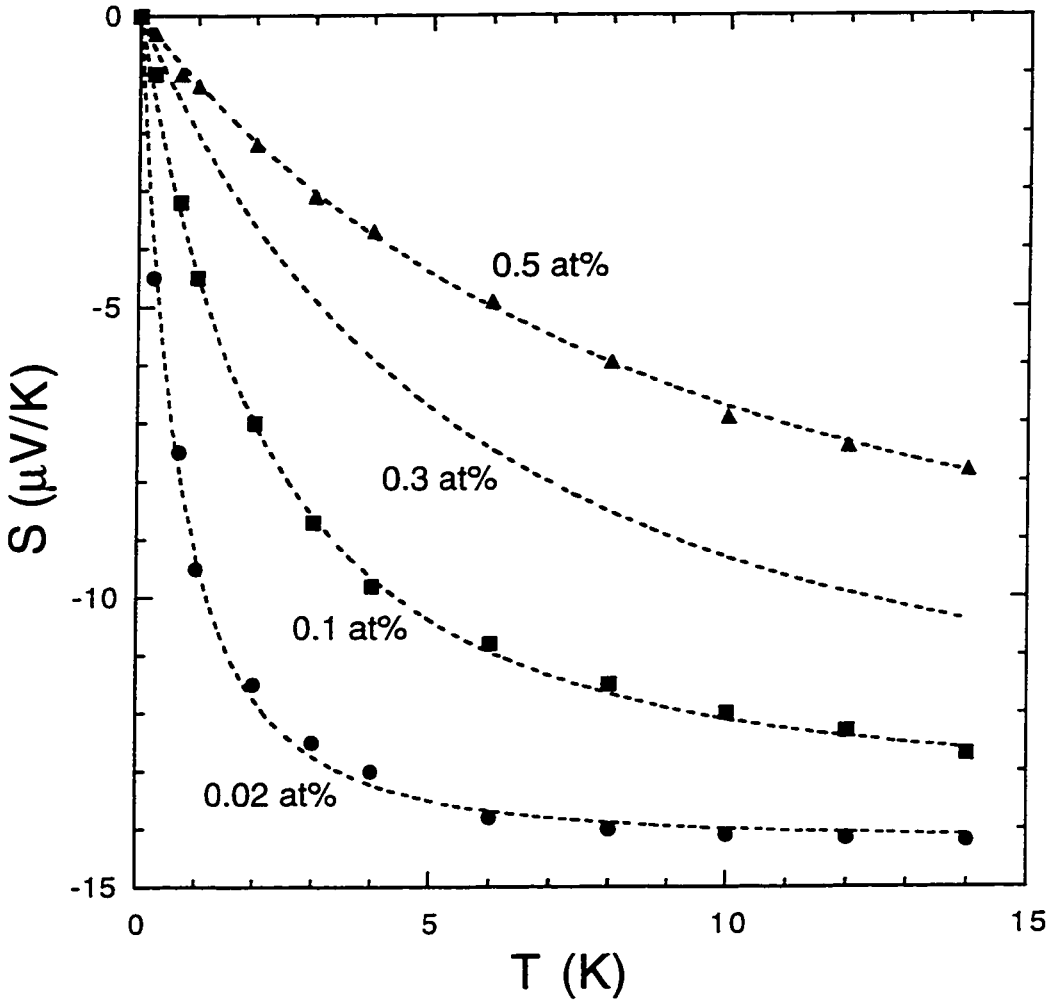

Figure 6.32: Absolute thermopower of AuFe alloys. Dotted line: phenomenological fits by Eq. 6.7. Solid circle: thermopower of AuFe alloys from Ref. [97].

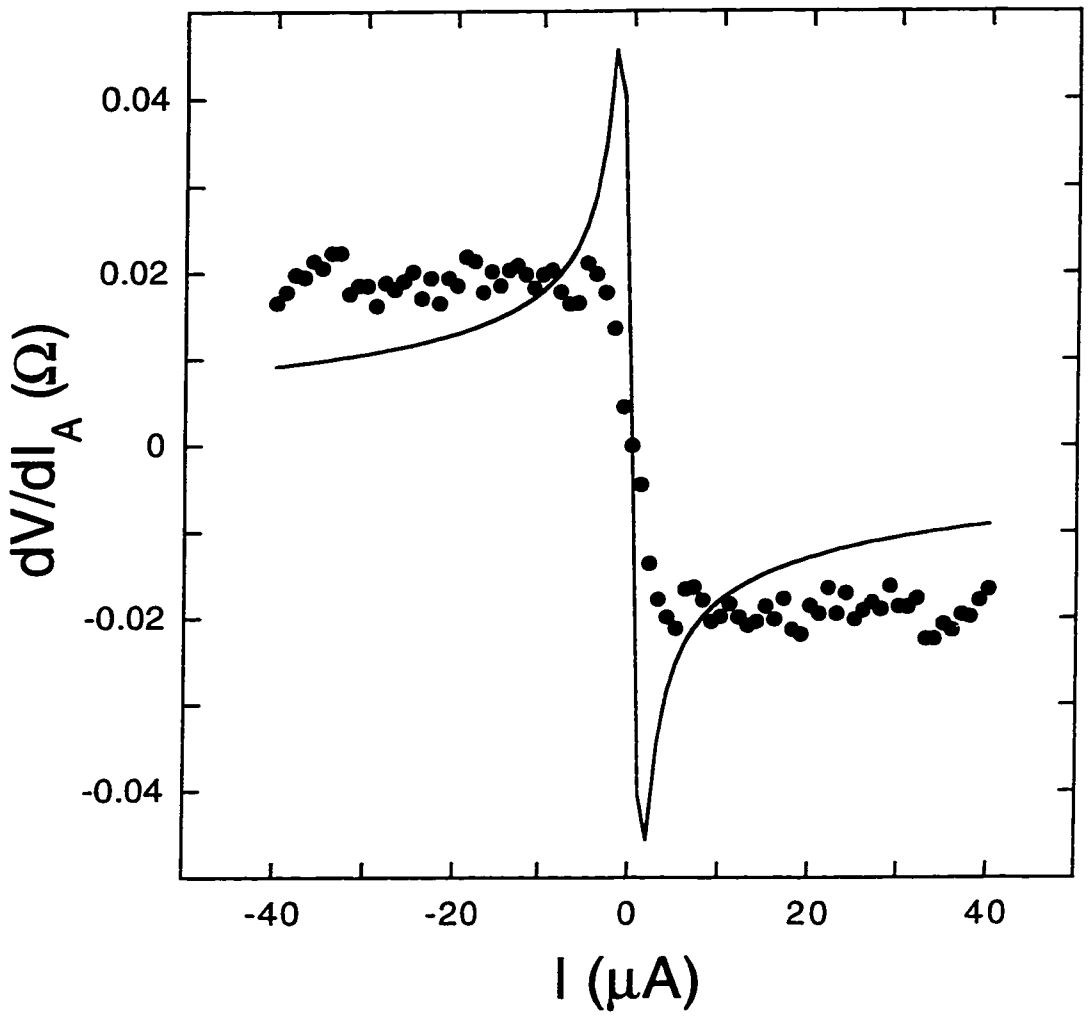

Figure 6.33: Calculated $dV/dI_A(I)$ caused by concentration variation between two voltage terminals. Solid circle: measured $dV/dI_A(I)$ of a AuFe 0.3 at% wire at T = 0.45 K (from Fig. 6.27). Solid line: calculated $dV/dI_A(I)$ associated with ΔS caused by the concentration variation $\delta c = 0.01$ at%. ΔS $(= S_{c=0.31at\%} - S_{c=0.3at\%})$ is obtained from Eq. 6.7.

been calculated. ΔS $(= S_{c=0.31at\%} - S_{c=0.3at\%})$ is obtained from Eq. 6.7. The calculated $dV/dI_A(I)$ are plotted in Fig. 6.33 along with the measured $dV/dI_A(I)$. The calculated $dV/dI_A(I)$ is different from the measurement $dV/dI_A(I)$. A sharp zero bias anomaly in the calculated $dV/dI_A(I)$ is not found in the measurement $dV/dI_A(I)$. In conclusion, we believe that concentration variations cannot explain the observed asymmetry in $dV/dI(I)$.

Although the following experiment does not necessarily support the idea of a mesoscopic thermopower, it provides direct evidence for the fact that $dV/dI_A(I)$ results from a thermal effect. Fig. 6.34 shows $dV/dI(I)$ as a function of the distance between a sample and a heater. The path of bias current is kept the same for all $dV/dI(I)$ measurements. The only moving part is the $V+$ terminal, so that the distance from the heater is increased. Since no current is passing through the sample (nonlocal measurement), the observed effect is expected to be solely related to a heating effect.

The resulting $dV/dI(I)$'s are entirely antisymmetric, having no contribution from a symmetric part. The amplitude of $dV/dI(I)$ decreases as the distance is increased, vanishing at a distance of ~ 6 μm. This is because the heating effect decays as the distance is increased, providing clear evidence for the fact that the asymmetry we observe is directly related to a thermal effect.

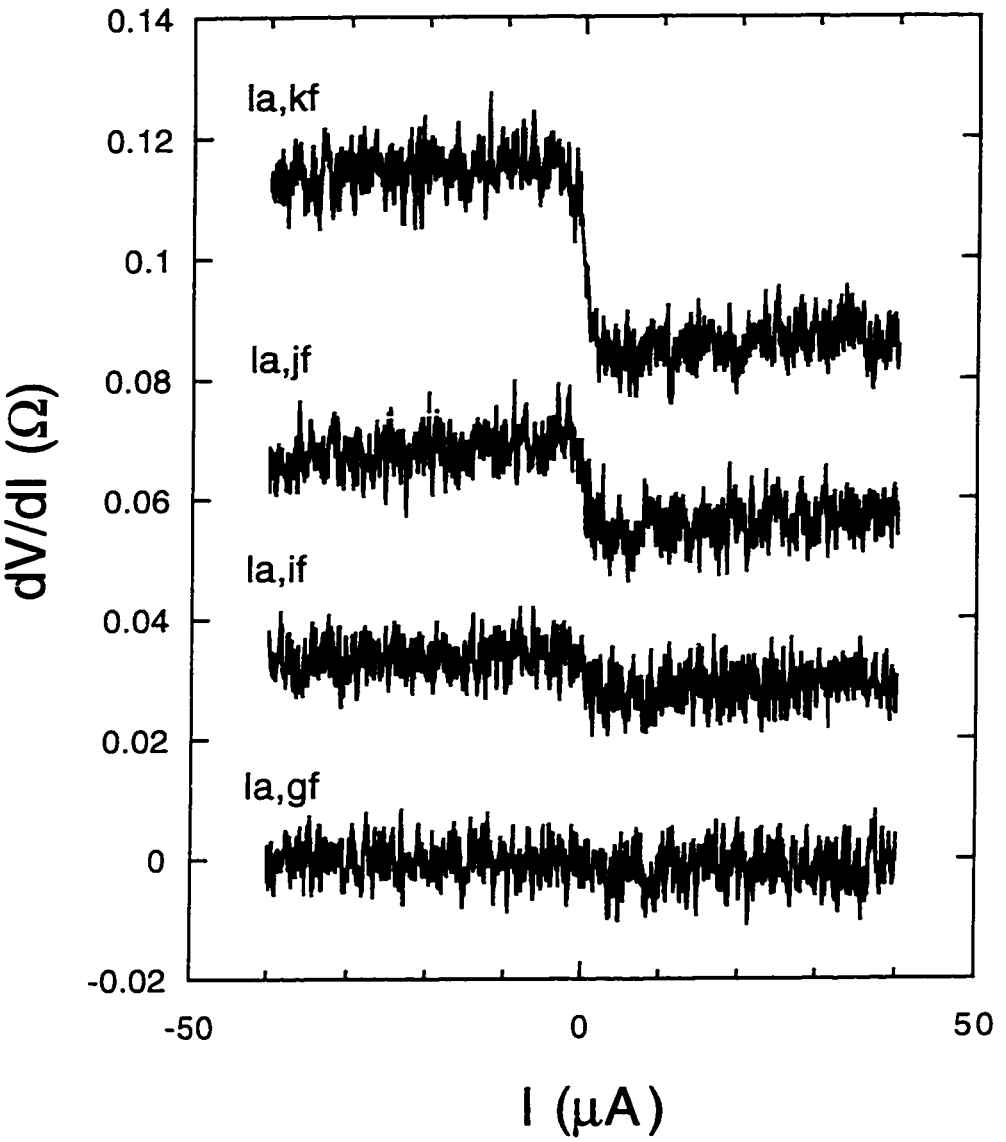

Figure 6.34: Nonlocal $dV/dI(I)$ of a 0.3 at% AuFe wire. Measurement configuration is denoted by $I+I-, V+V-$. The sample terminals are labeled as in Fig. 6.23.

6.4.4 Observed but yet to be explained

So far we have just concentrated on the antisymmetric part of $dV/dI(I)$, which is attributed to thermoelectric effects associated with the width difference of two voltage terminals. Now let us think about the symmetric part of $dV/dI(I)$.

The symmetric part of differential resistance, $dV/dI_{sym}(I)$ in the diffusive limit is believed to be nothing but $R(T)$ if I is properly converted into T. However, Fig. 6.35 shows a clear discrepancy between $dV/dI_{sym}(I)$ and $R(T)$ in their amplitude. It has been found that the difference in the amplitudes is more evident when the width of a AuFe wire becomes narrower. This discrepancy cannot be properly explained whichever way I is converted to T, because the discrepancy exists on the y-axis. A suggestion to explain this discrepancy has been made by K. Lane *et al.* [88]. In their point of view, $dV/dI(I)$ does not directly transform to $R(T)$ just by converting I into T because $R(T)$ is an averaged resistance rather than a differential resistance. If we write their recipe as a formula, it is expressed by

$$\begin{aligned} R(T) - R(T_b) &= \frac{1}{I}\int_0^I \frac{dV}{dI}(I)dI \\ &\neq \frac{dV}{dI}(I) - \frac{dV}{dI}(0) \end{aligned} \tag{6.9}$$

where T_b is the bath temperature, and T is temperature which is raised by I above T_b.

However, the scheme is not backed by appropriate physical explanations, and furthermore the conversion by the scheme does not work properly in narrow spin

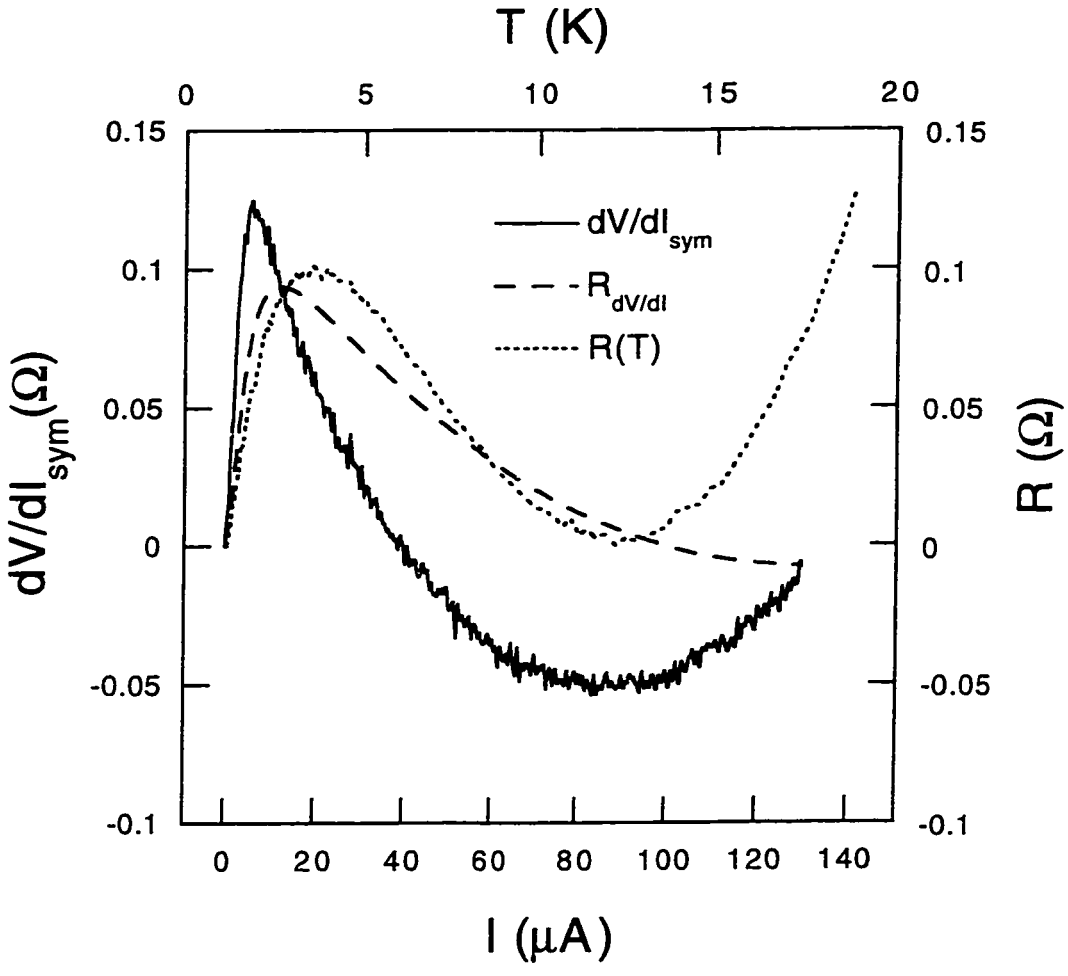

Figure 6.35: Enhanced amplitude of a spin glass maximum in $dV/dI(I)$. Solid line: $dV/dI_{sym}(I)$ at $T = 1.205$ K. Dashed line: $R_{dV/dI}$, the resistance converted from $dV/dI_{sym}(I)$. Dotted line: $R(T)$. R(T=1.205K) = 57.16 Ω. The sample is a AuFe 0.4 at% wire with $W = 85$ nm, $L = 3.5$ μm, and $t = 330$ Å.

glass wires as shown in Fig. 6.35. After converting $dV/dI(I)$ (solid line) into $R_{dV/dI}$ (dashed line) by their scheme, the minimum of $dV/dI(I)$ with high current regime disappears. This should not happen if the conversion is an appropriate one.

The discrepancy between the amplitudes of dV/dI_{sym} and R may be due to the difference of the phonon contribution for each case. Since the dc bias current effectively heats up the electron system only, the phonon contribution to the differential resistance ($dV/dI_{sym}(I)$) should be much smaller than normal resistance ($R(T)$). This fact explains the observation that the minimum of dV/dI_{sym} at $I \approx 90$ μA is much smaller than that of $R(T)$ at $T \approx 12$ K (see Fig. 6.35).

Further thorough study is demanded with regard to the discrepancy between the amplitudes of $dV/dI_{sym}(I)$ and $R(T)$, before we address the detailed mechanism involved in this problem.

Chapter 7

SUMMARY AND CONCLUSIONS

7.1 Size effect in the spin glass resistivity

The size dependence of electron-spin scattering in magnetic alloys has been continuously a hot issue in the mesoscopic physics community for the last seven or eight years. We have investigated the issue by resistivity measurements of AuFe spin glass wires. We have measured low temperature resistivity $\rho(T)$ on AuFe spin glass wires. The wires have a thickness $\sim$ 200 Å and linewidths ranging from 150 nm to 300 μm. A broad resistivity maximum was observed as T was lowered, reflecting the existence of spin freezing at low temperature. The observed resistivity maximum temperature T_m was indeed size dependent, decreasing as the linewidth was reduced. However, this T_m shift was found to be due to the electron-electron interaction contribution to $\rho(T)$, while the spin glass contribution was independent of linewidth. This result is in contrast the previously observed size effect of the spin glass resistivity for CuCr films [87], and leaves the open question of the characteristic length scale in spin glasses.

In a recent paper [123], Ujsaghy *et al.* proposed anisotropic spin-orbit scatter-

ing as the origin of the size effect of the resistivity in dilute magnetic alloys. The anisotropy is higher at the surface and hence the surface-to-volume ratio plays an important role in the size effect. The surface-to-volume ratio is not changed much by varying linewidth of wires, but the surface-to-volume ratio is changed considerably when the thickness of films is varied. Therefore one expects to see a cross-over of the size effect when the linewidth becomes smaller than the film thickness. To check this idea, one needs to measure the resistivity of very narrow wires of which the linewidth is comparable to the film thickness. We leave this thing as a future project.

7.2 Thermopower of mesoscopic spin glass wires

We have measured the differential resistance dV/dI of mesoscopic AuFe spin glass wires as a function of dc bias current I at low temperatures. The major role of dc bias current is heating of the conduction electron system above the lattice temperature. Therefore, $dV/dI(I)$ at low temperature resembles resistance as a function of T. When I is reduced from high currents, $dV/dI(I)$ decreases. When I is reduced further, $dV/dI(I)$ initially increases due to the Kondo effect, and finally decreases again due to spin glass freezing. Since electron heating is basically independent of the direction of I, the resulting $dV/dI(I)$ is expected to be symmetric in I. However, when the width of one voltage probe is less than $\sim$ 150 nm and different from the width of the other probe, $dV/dI(I)$ becomes asymmetric in I. By assuming the

existence of a size dependent thermopower in mesoscopic spin glasses, the observed asymmetry in $dV/dI(I)$ at various temperatures can be explained consistently. In conclusion, we find that *the thermopower of AuFe spin glass wires becomes size dependent as the width is reduced below* $\sim$ *150 nm.*

What is the reason we see a size dependence in the thermopower, but we see no size dependence in the resistivity? There could be a couple of answers to this question. First, the width of the wires in the resistivity study ranged only down to 150 nm. Therefore it is still consistent with the fact that the size dependence in the thermopower is revealed only below $\sim$ 150 nm. Second, it has been once pointed out that no size effects should be observed until the electronic density of states is modified [34]. The thermopower may be a more sensitive tool to detect a size effect which originates from the modification of the electronic density of states [140].

There is another issue which still needs to be resolved: the critical length scale for spin glasses or the Kondo effect. The Kondo length, $\xi_K = \hbar v_F/k_B T$, can be as large as 10 μm for AuFe alloys, and hence one should see a size effect in transport properties at much larger scales than was observed for the thermopower in this study. There might be a possibility that the Kondo length is not properly scaled. Actually, the critical length scale ($\sim$ 150 nm) which we found in thermopower turns out to be more or less consistent with Bergmann's argument [17]. He argued that the number of electrons which one needs to make the Kondo bound state is $\approx 10\varepsilon_F/k_B T_K$. Using the number density of conduction electrons for Au, one

gets a length scale of the Kondo bound state $\approx$ 20 nm. Then, one expects a size dependence on a much smaller size scale than ξ_K, as was observed in our experiments.

We are in the process of developing a local electron thermometer by using the temperature dependence of resistance of a normal metal wire in a proximity region around a normal/superconductor interface [37]. With this thermometry technique we expect a direct measurement of the thermopower of mesoscopic AuFe spin glass wires for various widths.

While developing an interpretation of the asymmetry in $dV/dI(I)$ of mesoscopic AuFe spin glass wires, we noticed that the measurement of $dV/dI(I)$ can be a very sensitive tool to detect thermopower of very small devices at very low temperatures. We have applied this method to measure the thermopower of Andreev interferometers, and demonstrated the first observation of quantum interference effects in the thermopower [51].

BIBLIOGRAPHY

[1] Abrahams, E., P. W. Anderson, P. A. Lee, and T. V. Ramakrishinan, Phys. Rev. B **24**, 6783 (1981).

[2] Adler, J. G., and J. E. Jackson, Rev. Sci. Instrum. **37**, 1049 (1966).

[3] Altshuler, B. L., preprint (con-matt/9803125).

[4] Altshuler, B. L., A. G. Aronov, and D. E. Khmelnitskii, Pisma Zh. Eksp. Teor. Fiz. **41**, 530 [JETP Lett. **41**, 648 (1985)].

[5] Altshuler, B. L., and A. G. Aronov, in *Electron-Electron Interactions in Disordered Systems*, edited by A. L. Efros and M. Pollak, (Elsevier Science Publishers B. V., 1985).

[6] Altshuler, B. L., A. G. Aronov, and D. E. Khmelnitskii, J. Phys. C **5**, 7367 (1982).

[7] Altshuler, B. L., and A. G. Aronov, Pisma Zh. Eksp. Teor. Fiz. **33**, 515 (1981) [JETP Lett. **33**, 499 (1981)].

[8] Altshuler, B. L., A. G. Aronov, and B. Z. Spivak, Pisma Zh. Eksp. Teor. Fiz. **33**, 101 (1981) [JETP Lett. **33**, 94 (1981)].

[9] Altshuler, B. L., and A. G. Aronov, Pisma Zh. Eksp. Teor. Fiz. **30**, 514 (1979) [JETP Lett. **30**, 482 (1979)].

[10] Altshuler, B. L., and A. G. Aronov, Zh. Eksp. Teor. Fiz. **75**, 1610 (1978) [JETP **48**, 812 (1978)].

[11] Altshuler, B. L., and D. E. Khmelnitskii, Pisma Zh. Eksp. Teor. Fiz. **42**, 291 [JETP Lett. **42**, 359 (1985)].

[12] Anderson, P. W., E. Abrahams, and T. V. Ramakrishnan, Phys. Rev. Lett. **43**, 718 (1979).

[13] Ashcroft, N. W., and N. D. Mermin, *Solid State Physics*, (Sauders College Publshing, New York, 1976).

[14] Belitz, D., and S. Das Sarma, Phys. Rev. B **36**, 7701 (1987).

[15] Benoit, A. D., Phys. Rev. Lett. **57**, 1765 (1986).

[16] Bergmann, G., W. Wei, and Y. Zou, Phys. Rev. B **41**, 7386 (1990).

[17] Bergmann, G., Phys. Rev. Lett. **67**, 2545 (1991).

[18] Bergmann, G., Phys. Rev. B **36**, 2469 (1987).

[19] Bergmann, G., Phys. Rev. Lett. **57**, 1460 (1986).

[20] Bergmann, G., Phys. Rep. **107**, 1 (1984).

[21] Bergmann, G., Phys. Rev. B **3**, 3797 (1971).

[22] Binder, K., and A. P. Young, Rev. Mod. Phys. **4**, 801 (1986).

[23] Blachly, M. A., and N. Giordano, Phys. Rev. B **51**, 12537 (1995).

[24] Blachly, M. A., and N. Giordano, Phys. Rev. B **49**, 6788 (1994).

[25] Blachly, M. A., and N. Giordano, Europhys. Lett. **27**, 687 (1994).

[26] Blachly, M. A., and N. Giordano, Physica(Amsterdam) **194B - 194B**, 983 (1994).

[27] Blachly, M. A., and N. Giordano, Phys. Rev. B **46**, 2951 (1992).

[28] Boyce, J. B., and C. P. Slichter, Phys. Rev. Lett. **32**, 61 (1974).

[29] Bray, A. J., and M. A. Moore, Phys. Rev. Lett. **58**, 57 (1987).

[30] Bray, A. J., and M. A. Moore, J. Phys. C **17**, L463 (1984).

[31] Buttiker, M., Phys. Rev. Lett. **57**, 1761 (1986).

[32] Cable, J. W., S. A. Werner, G. P. Felcher, and N. Wakabayashi, Phys. Rev. B **29**, 1268 (1984).

[33] Cannella, V., and J. A. Mydosh, Phys. Rev. B **6**, 4220 (1972).

[34] Chandrasekhar, V., P. Santhanam, N. A. Penebre, R. A. Webb, H. Vloeberghs, C. Van Haesendonck, and Y. Bruynseraede, Phys. Rev. Lett. **72**, 2053 (1994).

[35] Chandrasekhar, V., *Ph. D. Thesis*, (Yale University, 1989).

[36] Chandrasekhar, V., and M. J. Rooks, S. Wind, and D. E. Prober, Phys. Rev. Lett. **61**, 2253 (1988).

[37] Charlat, P., H. Courtois, Ph. Gandit, D. Mailly, A. F. Volkov, and B. Pannetier, Phys. Rev. Lett. **77**, 4950 (1996).

[38] Chen, G., and N. Giordano, Phys. Rev. Lett. **66**, 209 (1991).

[39] Coles, B. R., B. V. B. Sarkissian, and R. H. Taylor, Phil. Mag. **37**, 489 (1978).

[40] Cowen, J. A., J. Bass, and G. G. Kenning, J. Appl. Phys. **64**, 5781 (1988).

[41] Crisp, R. S., W. G. Henry, and P. A. Schroeder, Phil. Mag. **10**, 553 (1964), This report is actually for CuGe, but we expect a similar thermopower for AuGe.

[42] Datta, S., M. R. Melloch, S. Bandyopadyay, R. Noren, M. Varizi, M. Miller, and R. Reifenberger, Phys. Rev. Lett. **55**, 2344 (1985).

[43] de Almeida, J. R. L., and D. J. Thouless. Phys. Rev. A **11**, 983 (1978).

[44] de Vegvar, P. G. N., J. M. Slaughter, and J. A. Cowen, Phys. Rev. Lett. **66**, 2380 (1991).

[45] Daybell, M., in *Magnetism*, edited by G. T Rado and H Suhl (Academic, New York, 1973), Vol. 5.

[46] DiTusa, J. F., K. Lin, M. Park, S. Isaacson, and J. M. Parpia, Phys. Rev. Lett. **68**, 678 (1992).

[47] Dobisz, E. A., C. R. K. Marrian, and R. J. Colton, Appl. Phys. Lett. **70**, 1973 (1991).

[48] Edwards, S. F., and P. W. Anderson, J . Phys. F: Metal Phys. **5**, 89 (1975).

[49] Eom, J., J.-G. Yoon, S.-I. Kwun, Phys. Rev. B **44**, 2826 (1992).

[50] Eom, J., G. Neuttiens, C. Strunk, C. Van Haesendonck, Y. Bruynseraede, and V. Chandrasekhar, Phys. Rev. Lett. **77**, 2276 (1996).

[51] Eom, J., C.-J. Chien, and V. Chandrasekhar, preprint (cond-mat/9803371).

[52] Feng, S., A. J. Bray, P. A. Lee, and M. A. Moore, Phys. Rev. B **36**, 5624 (1987).

[53] Fischer, K. H., *Spin Glasses*, (Cambridge University Press, New York, 1991).

[54] Fischer, K. H., Phys. Rev. Lett. **34**, 1438 (1975).

[55] Fisher, D. S., and D. A. Huse, Phys. Rev. B **38**, 386 (1988).

[56] Fisher, D. S., and D. A. Huse, Phys. Rev. Lett. **56**, 1601 (1986).

[57] Ford, D. J., and J. A. Mydosh, Phys. Rev. B **14**, 2057 (1976).

[58] Garcia, R. G., Appl. Phys. Lett. **60**, 1960 (1992).

[59] Gorkov, L. P., A. I. Larkin, and D. E. Khmelnitskii, Pisma Zh. Eksp. Teor. Fiz. **30**, 248 [JETP Lett. **30**, 228 (1979)].

[60] Gotaas, J. A., J. J. Rhyne, and S. A. Werner, J. Appl. Phys. **57**, 3404 (1985).

[61] Gruener, G., and A. Zawadowski, Prog. Low Temp. Phys. **7B**, 591 (1978).

[62] Gubernatis, J. E., J. E. Hirsch, and D. J. Scalapino, Phys. Rev. B **35**, 8478 (1987).

[63] Heeger, A. J., in *Magnetism*, edited by G. Rado and H. Suhl, (Academic Press, New York, 1973).

[64] Heeger, A. J., in *Solid State Physics*, edited by H. Ehrenreich, F. Seitz, and D. Turnbull, (Academic Press, New York,1969).

[65] Heeger, A. J., A. P. Klein, and P. Tu, Phys. Rev. Lett. **17**, 803 (1966).

[66] Henny, M., H. Birk, R. Huber, C. Strunk, A. Bachtold, M. Kruger, and C. Schönenberger, Appl. Phys. Lett. **71**, 773 (1997).

[67] Hoines, L., R. Stubi, R. Loloee, J. A. Cowen, and J. Bass, Phys. Rev. Lett. **66**, 1224 (1990).

[68] Horowitz, P., and W. Hill, *The Art of Electronics*, (Cambridge University Press, New York 1982).

[69] Huntley, D. J., and C. W. E. Walker, Can. J. Phys. **47**, 805 (1969).

[70] Huse, D. A., and I. Morgenstern, Phys. Rev. B **38**, 373 (1988).

[71] Imry, Y., Europhys. Lett. **1**, 249 (1986).

[72] Ishii, H., J. Low. Temp. Phys. **32**, 457 (1978).

[73] Israeloff, N. E., M. B. Weismann, G. J. Nieuwenhuys, and J. Kosiorowska, Phys. Rev. Lett. **63**, 794 (1989).

[74] Jagannathan, A., E. Abrahams, and M, Stephen, Phys. Rev. B **37**, 436 (1988).

[75] Kaplan, S. B., A. Harstein, Phys. Rev. Lett. **56**, 2403 (1986).

[76] Kastner, M. A., R. F. Kwasnik, J. C. Licini, and D. J. Bishop, Phys. Rev. B **36**, 8015 (1987).

[77] Kasuya, T., Prog. Theor. Phys. **16**, 45 (1956).

[78] Keck, B., and A. Schmid, J. Low Temp. Phys. **24**, 611 (1976).

[79] Kenning, G. G., J. Bass, W. P. Pratt Jr., D. Leslie-Pelecky, L. Hoines, W. Leach, M. L. Wilson, R. Stubi, and J. A. Cowen, Phys. Rev. B **42**, 2393 (1990).

[80] Kenning, G. G., J. Bass, W. P. Pratt Jr., D. Leslie-Pelecky, L. Hoines, W. Leach, R. Stubi, and J. A. Cowen, Phys. Rev. Lett. **59**, 2596 (1987).

[81] Ketelsen, L. J. P., and M. B. Salamon, Phys. Rev. B **33**, 3610 (1986).

[82] Kirkpatrick, S., and D. Sherrington, Phys. Rev. B **17**, 4384 (1978).

[83] Kondo, J., in *Magnetism*, edited by G. Rado and H. Suhl, (Academic press, New York, 1973).

[84] Kondo, J., Prog. Theor. Phys. **34**, 372 (1965).

[85] Kondo, J., Prog. Theor. Phys. **32**, 37 (1964).

[86] Korn, D., Z. Phys. **238**, 275 (1970).

[87] Lane, K. R., M. Park, M. S. Isaacson, and J. M. Parpia, Phys. Rev. B **51**, 945 (1995).

[88] Lane, K. R., M. Park, M. S. Isaacson, and J. M. Parpia, J. Low Temp. Phys. **93**, 7 (1993).

[89] Larsen, U., J. Appl. Phys. **49**, 1610 (1978).

[90] Larsen, U., Phys. Rev. B **14**, 4356 (1976).

[91] Lee, P. A., Physica A **140**, 169 (1986).

[92] Lee, P. A., and A. D. Stone, Phys. Rev. Lett. **55**, 1622 (1985).

[93] Li, G., M. Chen, G. Liu, M. Wang, S. Wang, and S. Yan, Phys. Rev. B **57**, 2683 (1998).

[94] Licini, J. C., D. J. Bishop, M. A. Kastner, and J. Melngailis, Phys. Rev. Lett. **55**, 2987 (1985).

[95] Maletta, Phys. Rev. Lett. **42**, 108 (1979).

[96] Martin, I., Y. Wan, P. Phillips, Phys. Rev. Lett. **78**, 114 (1997).

[97] McDonald, D. K. C., Proc. Roy. Soc. **A266**, 166 (1962).

[98] McMillan, W. L., J. Phys. C **17**, 3179 (1984).

[99] Mohanty, P., E. M. Q. Jariwala, and R. A. Webb, Phys. Rev. Lett. **78**, 3366 (1997).

[100] Mydosh, J. A., *Spin Glasses: an Experimental Introduction*, (Taylor & Francis Inc., PA, 1993).

[101] Nagaev, K. E., Phys. Rev. B **52**, 4740 (1995).

[102] Nagata, S., P. H. Keesom, and H. R. Harrison, Phys. Rev. B **19**, 1633 (1979).

[103] Neuttiens, G., J. Eom, C. Strunk, H. Pattyn, C. Van Haesendonck, Y. Bruynseraede, and V. Chandrasekhar, to appear in Europhys. Lett.

[104] Neuttiens, G., J. Eom, C. Strunk, V. Chandrasekhar, C. Van Haesendonck, and Y. Bruynseraede, Europhys. Lett. **34** 617 (1996).

[105] Omelyanchuk, A. N., and I. G. Tuluzov, Sov. J. Low Temp. **11**, 211 (1985).

[106] Parisi, G., J. Phys. A: Math. Gen. **13**, 1887 (1980).

[107] Parisi, G., J. Phys. A: Math. Gen. **13**, 1101 (1980).

[108] Parisi, G., Phys. Rev. Lett. **43**, 1754 (1979).

[109] Pobell, F., *Matter and Methods at Low Temperatures.* (Springer-Verlag, Berlin, 1996).

[110] Ruderman, M. A., and C. Kittel, Phys. Rev. **96**, 99 (1954).

[111] Schmid, A., Z. Phys. F **271**, 251 (1974).

[112] Sherrington, D., and S. Kirkpatrick, Phys. Rev. Lett. **35**, 1792 (1975).

[113] Sherrington, D., and B. W. Southern, J. Phys. F **5**, 49 (1975).

[114] Skocpol, W. J., P. M. Mankiewich, R. E. Howard, L. D. Jackel, D. M. Tennant, and A. D. Stone, Phys. Rev. Lett. **56**, 2865 (1975).

[115] Strunk, C., M. Henny, C. Schönenberger, G. Neuttiens, C. Van Haesendonck, preprint (1998).

[116] Stubi, R., J. A. Cowen, D. Leslie-Pelecky, and J. Bass, Physica (Amsterdam) **165B - 166B**, 2438 (1990).

[117] Takayama, H., Z. Phys. **263**, 329 (1973).

[118] Tholence, J. L., and R. Tournier, J. Phys. **35**, C4-229 (1974).

[119] Thouless, D. J., Phys. Rev. Lett. **39**, 1167 (1977).

[120] Thouless, D. J., P. W. Anderson, and R. G. Palmer, Phil. Mag. **35**, 137 (1977).

[121] Ujsaghy, O., and A. Zawadowski, Phys. Rev. B **57**, 11609 (1998).

[122] Ujsaghy, O., and A. Zawadowski, Phys. Rev. B **57**, 11598 (1998).

[123] Ujsaghy, O., A. Zawadowski, and B. L. Gyorffy, Phys. Rev. Lett. **76**, 2378 (1996).

[124] van der Post, N., F. L. Metters, J. A. Mydosh, J. M. Ruitenbeek, and I. K. Yanson, Phys. Rev. B **53**, R476 (1996).

[125] van der Post, N., J. A. Mydosh, J. M. Ruitenbeek, and I. K. Yanson, Phys. Rev. B **53**, 15106 (1996).

[126] Van Haesendonck, C., J. Vranken, Y. Bruynseraede, Phys. Rev. Lett. **58**, 1968 (1987).

[127] Vier, D. C., and S. Schultz, Phys. Rev. Lett. **54**, 150 (1985).

[128] Vloeberghs, H., J. Vranken, C. Van Haesendonck, and Y. Bruynseraede, Europhys. Lett. **12**, 557 (1990).

[129] Vranken, J., C. Van Haesendonck, H. Vloeberghs, and Y. Bruynseraede, Physc. Scr. **T25**, 348 (1989).

[130] Washburn, S., H. Schmid, D. Kern, and R. A. Webb, Phys. Rev. Lett. **59**, 1791 (1987).

[131] Washburn, S., and R. A. Webb, Adv. Phys. **35**, 375 (1986).

[132] Webb, R. A., S. Washburn, and C. P. Umbach, Phys. Rev. B **37**, 8455 (1988).

[133] Wenger, L. E., and P. H. Keesom, Phys. Rev. B **13**, 4053 (1976).

[134] Werner, S. A., and J. W. Cable, J. Appl. Phys. **52**, 1757 (1981).

[135] Wilson, K., Rev. Mod. Physc. **47**, 773 (1975).

[136] Yanson, I. K., V. V. Fisun, A. V. Khotkevich, R. Hesper, J. M. Krans, J. A. Mydosh, and J. M. van Ruitenbeek, Low Temp. Phys. **20**, 836 (1994).

[137] Yanson, I. K., V. V. Fisun, R. Hesper, A. V. Khotkevich, J. M. Krans, J. A. Mydosh, and J. M. van Ruitenbeek, Phys. Rev. Lett. **74**, 302 (1995).

[138] Yacoby, A., M. Heiblum, D. Mahalu, H. Shtrikman, Phys. Rev. Lett. **74**, 893 (1995).

[139] Yosida, K., Phys. Rev. **106**, 893 (1957).

[140] Ziman, J. M., *Principles of the Theory of Solids.* (Cambridge University Press, New York, 1972).

Appendix A

LIST OF CHEMICALS, ELECTRONIC COMPONENTS, AND MEASUREMENT APPARATUS USED IN THIS STUDY

AD524, AD624, AD630, AD632 Analog Devices, Norwood, MA.

Dow Corning 340 Dow Corning Corp., Midland, Mich.

DS345 Stanford Research Systems, Sunnyvale, CA.

Edwards 306 Edwards High Vacuum, West Sussex, England.

GenRad 1432-W Decade Resistor General Radio Co., Concord, MA.

HP3325A, HP6260B Hewlett Packard, Cupertino, CA.

JXA-840 Scanning electron microscope, JEOL.

Keithley 230 Keithley Instruments, Inc., Cleveland, OH.

Kepco BOP 20-20M, Kepco BOP 100-1M Kepco, Inc., Flushing, NY.

Kulicke and Soffa Model 4123 Kulick and Soffa Industries, Inc., Willow Grove, PA.

LakeShore Model 622 Lake Shore Cryotronics, Inc., Westerville, OH.

Leybold XTM/2 Deposition Monitor Leybold Inficon Inc., East Syracuse, New York.

Microposit MF-319 Developer Shipley, Marlborough, MA.

Microposit S1813 Photo Resist Shipley, Marlborough, MA.

NANO^{TM} 100PMMA A4 Microlithography Chemical Corp., Newton, MA.

NANO^{TM} 495PMMA A4 Microlithography Chemical Corp., Newton, MA.

Oxford 300 Kelvinovax Oxford Instruments, Oxon, England.

PAR116, PAR124 Princeton Applied Research, Princeton, NJ.

Pi section filter Murata Electronics North America, Inc., Rockmart, GA. The filters used in this study have a loss $\sim$ 5 dB at 10 MHz and $\sim$ 70 dB at 1 GHz.

Silicon wafers Polishing Corporation of America, Santa Clara, CA.

Superconducting wires We use superconducting wires for data lines. The wires have a CuNi 0.004″ diameter with Formvar insulating skin. Supercon, Inc., Shrewsbury, MA.

Tencor P-10 Tencor Instruments, Mountain View, CA.

Triad G-31 Triad-Utrad Distributor, Huntington, IND.

Quintel Q-2001CT Quintel Corp., San Jose, CA.

1 MΩ Precision Resistor Vishay Resistive Systems Group, Malvern, PA.

12 Tesla Superconducting magnet Oxford Instruments, Oxon, England.

6 Tesla Superconducting Magnet Cryomagnetics, Inc., Oak Ridge, TN.

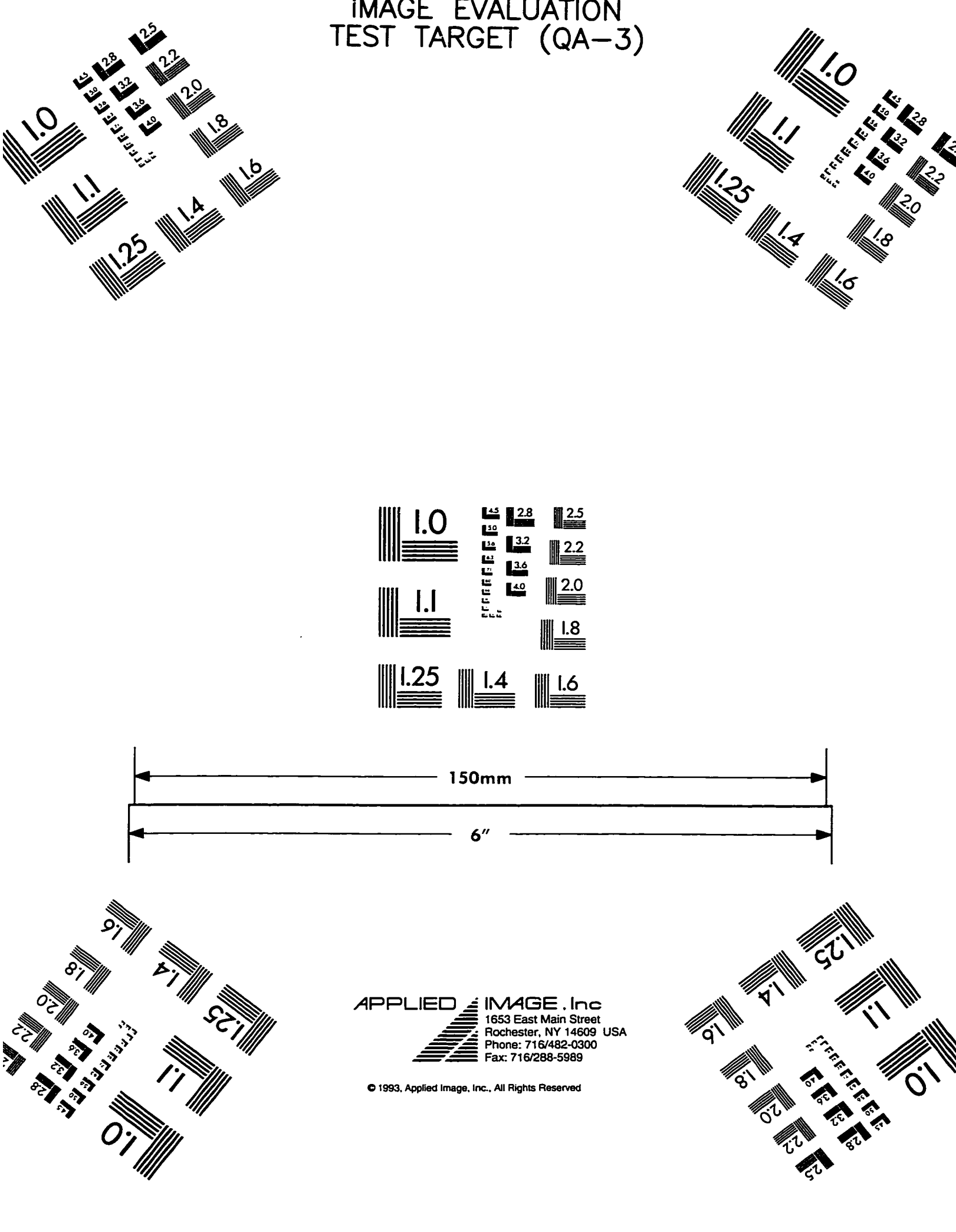
IMAGE EVALUATION
TEST TARGET (QA-3)
1.0
1.1
1.25
1.4
1.6
1.8
2.0
2.2
2.5
2.8
3.2
3.6
4.0
150mm
6"
APPLIED IMAGE, Inc
1653 East Main Street
Rochester, NY 14609 USA
Phone: 716/482-0300
Fax: 716/288-5989
© 1993, Applied Image, Inc., All Rights Reserved